

分类号\_\_\_\_\_

密级\_\_\_\_\_

UDC\_\_\_\_\_

编号\_\_\_\_\_

华中师范大学  
博士学位论文

RHIC 能量扫描中氙核产生以及产额比  
( $N_t \times N_p / N_d^2$ ) 的实验研究

学位申请人姓名:

张定伟

申请学位学生类别:

全日制博士

申请学位学科专业:

粒子物理与原子核物理

指导教师姓名:

罗晓峰 教授

Tetyana Galatyuk 教授



忠诚博雅，朴实刚毅

Dedicated to my family

谨献给我的家人

# 博士学位论文

论文题目：RHIC 能量扫描中氙核产生以及产额比  $(N_t \times N_p / N_d^2)$  的实验研究

论文作者：张定伟  
指导教师：罗晓峰 教授, Tetyana Galatyuk 教授  
学科专业：粒子物理与原子核物理  
研究方向：相对论重离子碰撞物理

华中师范大学物理科学与技术学院

2023 年 5 月

# Dissertation

## Measurement of Triton Production and Yield Ratio $(N_t \times N_p / N_d^2)$ in Au+Au Collisions at RHIC Beam Energy Scan

By

Dingwei Zhang

Supervisor: Prof. Xiaofeng Luo, Prof. Tetyana Galatyuk

Specialty: Particle Physics and Nuclear Physics

Research Area: Physics of Relativistic Heavy Ion  
Collision

College of Physical Science and Technology

Central China Normal University

May, 2023

# 华中师范大学学位论文原创性声明和使用授权说明

## 原创性声明

本人郑重声明：所呈交的学位论文，是本人在导师指导下，独立进行研究工作所取得的研究成果。除文中已经标明引用的内容外，本论文不包含任何其他个人或集体已经发表或撰写过的研究成果。对本文的研究做出贡献的个人和集体，均已在文中以明确方式标明。本声明的法律结果由本人承担。

作者签名：

日期：2023年5月26日

## 学位论文授权使用授权书

学位论文作者完全了解华中师范大学有关保留、使用学位论文的规定，即：研究生在校攻读学位期间论文工作的知识产权单位属华中师范大学。学校有权保留并向国家有关部门或机构送交论文的复印件和电子版，允许学位论文被查阅和借阅；学校可以公布学位论文的全部或部分内容，可以允许采用影印、缩印或其它复制手段保存、汇编学位论文。（保密的学位论文在解密后遵守此规定）  
保密论文注释：本学位论文属于保密，在\_\_\_\_\_年解密后适用本授权书。非保密论文注释：本学位论文不属于保密范围，适用本授权书。

作者签名：

导师签名：

日期：2023年5月26日

日期：2023年5月26日

---

本人已经认真阅读“CALIS 高校学位论文全文数据库发布章程”，同意将本人的学位论文提交“CALIS 高校学位论文全文数据库”中全文发布，并可按“章程”中的规定享受相关权益。同意论文提交后滞后： 半年； 一年； 二年发布。

作者签名：

导师签名：

日期：2023年5月26日

日期：2023年5月26日

# Contents

<b>1</b>	<b>Introduction</b>	<b>1</b>
1.1	Elementary Particle and Standard Model . . . . .	1
1.2	Quantum Chromodynamics(QCD) Phase Diagram and Critical Point . . . . .	7
1.3	Relativistic Heavy Ion Collision (HIC) . . . . .	10
1.4	Light Nuclei Production in HIC . . . . .	11
1.4.1	Importance of Light Nuclei Production . . . . .	11
1.4.2	The Formation Mechanism of Light Nuclei in HIC . . . . .	12
1.4.3	Neutron Density Fluctuation - The Light Nuclei Compound Yield Ratio . . . . .	15
1.5	Thesis Motivation . . . . .	17
<b>2</b>	<b>Experiment Setup</b>	<b>19</b>
2.1	Relativistic Heavy Ion Collider . . . . .	19
2.2	STAR Detector System . . . . .	20
2.2.1	Time Projection Chamber . . . . .	21
2.2.2	Time of Flight . . . . .	25
2.3	Simulation of STAR Experiment . . . . .	27
<b>3</b>	<b>Analysis Details for Triton</b>	<b>29</b>
3.1	Data Set . . . . .	29
3.1.1	Event Selection . . . . .	30
3.1.2	Track Selection . . . . .	33
3.2	Centrality Determination . . . . .	33
3.3	Triton Identification . . . . .	36



---

3.4	Data Correction . . . . .	50
3.4.1	TPC Tracking Efficiency . . . . .	50
3.4.2	TOF Matching Efficiency . . . . .	53
3.4.3	Energy Loss Correction . . . . .	55
3.4.4	Absorption Correction . . . . .	56
3.4.5	Triton Background Estimation . . . . .	56
3.5	Systematic Uncertainty Estimation . . . . .	60
3.5.1	On transverse momentum spectra . . . . .	60
3.5.2	On $dN/dy$ and $\langle p_T \rangle$ . . . . .	62
<b>4</b>	<b>Analysis Details for Proton</b> . . . . .	<b>65</b>
4.1	Data Set . . . . .	65
4.2	Feed-down Correction Procedure . . . . .	67
4.3	Feed-down Correction Results . . . . .	71
4.4	Systematic Uncertainty Estimation . . . . .	73
4.4.1	On Primordial Proton Yields . . . . .	73
4.4.2	On Light Nuclei Yield Ratio ( $N_t \times N_p/N_d^2$ ) . . . . .	74
<b>5</b>	<b>Results and Discussion</b> . . . . .	<b>79</b>
5.1	Transverse Momentum Spectra . . . . .	79
5.2	Coalescence Parameters . . . . .	80
5.3	Particle Integral Yields ( $dN/dy$ ) and Average Transverse Momentum ( $\langle p_T \rangle$ ) . . . . .	82
5.4	Particle Ratios . . . . .	86
<b>6</b>	<b>Summary, Others, and Outlook</b> . . . . .	<b>94</b>
6.1	Summary . . . . .	94
6.2	Di-lepton Production . . . . .	95
6.3	Outlook . . . . .	97
	<b>Bibliography</b> . . . . .	<b>107</b>
	<b>Publications and Presentations</b> . . . . .	<b>118</b>
	<b>Achnowledgments</b> . . . . .	<b>120</b>

# 摘 要

现代物理学从 19 世纪发展至今, 严格而科学的理论告诉我们, 夸克、轻子通过电磁相互作用、弱相互作用、强相互作用和引力相互作用构成了自然界奥妙无穷、千变万化的物理规律。其中强相互作用是四大相互作用中最强的, 是理解微观世界基本组成以及它们之间相互作用运动规律的关键。强相互作用的不断研究与发展最终建立了强相互作用量子场论-量子色动力学 (QCD) 理论。QCD 理论的基本成分是夸克和胶子, 它们被紧紧的束缚在强子的内部, 不能单独的达到自由的状态, 只可能间接的由强子实验来观测它们的存在。相对论重离子碰撞实验作为研究 QCD 相结构的强有力的工具, 为探索核物质性质, 强相互作用以及宇宙演化有着指导性的作用。格点 QCD 理论预言在高温低重子密度区域发生的从夸克胶子禁闭的强子物质相到退禁闭的夸克胶子等离子体 (QGP) 相的转变是平滑过渡, 而在低温高重子密度区域发生的相变是一阶相变, 并且一阶相变边界有个终点, 被称为 QCD 临界点。寻找和确定临界点成为当今高能物理实验和理论研究的热点和前沿课题。近年来有理论提出, 基于核子合并模型的轻核产生与系统演化的局域重子数密度紧密相关, 预示着末态的轻核将会携带核物质相变的信息, 重离子碰撞中的轻核测量也将作为探索 QCD 相结构的有效探针。

轻核是由 2-40 个核子组成的相对稳定的原子核, 也称之为核子团簇, 在中低能核物理和高能物理中都是十分重要的研究对象。经过半个多世纪的研究和发展, 众多理论都在尝试去理解重离子碰撞中轻核的产生, 其中较为成功的有核子合并模型和热力学统计模型等, 但目前该问题仍没有明确的答案。近年来有理论提出, 基于核子合并机制的轻核复合产额比 ( $N_t \times N_p / N_d^2$ ) 与重离子末态系统中局域中子数密度涨落直接相关, 而该涨落则能作为核物质相变的有效信号。因为当系统发生相变或到达临界点附近, 系统的关联长度发散, 从而引发系统中局域重子数密度的不均匀, 当核子通过合并形成成为轻核时, 重子数密度涨落的相关信息则会直接携带在轻核产额当中。在核子合并模型中, 轻核的产额强烈依赖于系统的体积和动力学冻结温度等, 所以单个轻核的产额是很动态的, 很难作为了解系统动态演化的有效观测量。轻核的复合产额比  $N_t \times N_p / N_d^2$ , 可以将压倒性的密度、体积等效应抵消, 从而使隐藏在轻核产额中可能存在的核子密度涨落浮现出来。



美国布鲁克海文国家实验室的相对论重离子对撞机是目前世界上进行高能重离子碰撞的大型实验装置之一，其中 STAR 实验致力于高温高密条件下夸克胶子等离子体性质以及 QCD 相结构的实验研究。STAR 探测器是由多个不同功能的粒子探测器组成，其核心寻迹部分包含圆柱形的时间投影室 (TPC) 和飞行时间探测器 (TOF)，其具有全方位角及较大中心快度区域覆盖的接受度，并具有优异的粒子鉴别能力。2010 年至今，STAR 能量扫描计划中采集了金核-金核对撞，质心系能量  $\sqrt{s_{NN}} = 3-200$  GeV 的数据，其对应的重子化学势为 750-25 MeV，在 QCD 相图上覆盖了较宽的范围，这为从实验上研究 QCD 相图提供了有效的途径。本文主要介绍 (1) 金核-金核对撞，质心系能量为 7.7, 11.5, 14.5, 19.6, 27, 39, 54.4, 62.4, 和 200 GeV 下氙核的产生。(2) 除 200 GeV 外，其余能量下原初质子横动量谱和积分产额的提取。(3) 7.7-200 GeV 下轻核复合产额比  $N_t \times N_p / N_d^2$  的测量，该比值在 19.6 和 27 GeV 下 0%-10% 对心碰撞中呈现能量依赖的非单调行为，且该比值的合并增强偏离理论基线 4.1 倍的标准差，在边缘碰撞和不含临界点的模型中都是单调变化的行为，理论预言该非单调行为与核物质相变及 QCD 临界点紧密相关，目前仍无明确的答案。本课题系统研究了 STAR 实验第一阶段能量扫描中轻核的产生，较大能量范围内氙核产额、原初质子产额、产额比等相关测量结果的获得，为重离子碰撞中实验测量的信息提供了重要的实验数据。新观测量的提出以及实验测量结果，为人们对重离子碰撞中轻核的产生机制以及 QCD 相图的理解提供了全新的见解。

本文将着重介绍 STAR 第一阶段能量扫描中氙核产生、质子弱衰变修正以及轻核复合产额比值等结果的测量过程。相关分析方法、修正细节、模型比较以及物理意义的讨论都会一一呈现。论文有以下几个章节组成：第 1 章主要为本文绪论部分，简单介绍了现代物理学发展背景和本文的研究动机。第 2 章介绍了 RHIC-STAR 实验装置，以及我们所用到的探测器和探测方法。第 3 章介绍了 STAR 实验第一阶段能量扫描中氙核的测量，详细介绍了数据分析的流程，最终得到了氙核的产额。第 4 章则是对 STAR 已经发表的末态总质子进行了奇异粒子弱衰变的修正，阐述了修正过程，给出了原初质子的产额以及弱衰变质子所占比例。第 5 章给出了我们的测量最终的结果以及相关的物理讨论。第 6 章进行了简单的总结和展望。高能重离子碰撞中轻核的测量研究为探索为 QCD 相图以及重离子碰撞中轻核形成机制的认知有着极其重要的科学意义。

**关键词：**相对论重离子碰撞；量子色动力学；临界点；氙核的产生；原初质子产额，轻核复合产额比值。

# Abstract

Modern physics has been continuously developing since the 19th century, rigorous and scientific theories have taught us that quarks and leptons constitute the mysterious and ever-changing physical laws of nature through electromagnetic interaction, weak interaction, strong interaction, and gravitation interaction. The strong interaction is the strongest of the four interactions and plays an essential role in establishing the basic composition of the micro world and how the laws of interaction and motion work between particles. The study of strong interactions has led to the development of the strong interaction quantum field theory, also known as Quantum Chromodynamics (QCD) theory, which is based on two fundamental components, namely quarks and gluons, that are tightly bound inside hadrons and cannot exist independently. The lattice QCD theory predicts that the transition from the quark-gluon confined hadron matter phase to the deconfined Quark Gluon Plasma (QGP) phase is a smooth transition at high temperature and low baryon density regions. However, the phase transition occurring at low temperature and high baryon density regions is a first-order phase transition with an endpoint at the boundary of the first-order phase transition, called the QCD Critical Point (CP). Currently, detecting and determining critical points is a hot and frontier topic in high energy experimental and theoretical physics. Recent theories suggest that light nuclei production based on the nucleon coalescence model is closely related to the local baryon number density of system evolution, which predicts that light nuclei in the final state will carry information about the phase transition of nuclear matter, and light nuclei measurements in heavy ion collisions will also serve as an effective probe to explore the QCD phase structure.

Light nuclei are relatively stable nuclei consisting of 2-40 nucleons, also known as nucleon clusters. They are important objects of study in both low- and intermediate-energy nuclear physics as well as high energy physics. After more than half a century of research and development,



many theories have been developed to try to understand the production mechanism of light nuclei in heavy-ion collisions. Among them, the nucleon coalescence model and the thermodynamic statistical model have been relatively successful, but there is still no definitive answer to this question. In recent years, a theoretical proposal has been put forward that the nuclear compound yield ratio ( $N_t \times N_p/N_d^2$ ), light nuclei production based on the nucleon coalescence mechanism, is directly connected to the local neutron density fluctuation in the final state system of heavy-ion collisions. This fluctuation can be utilized as an effective signal for the phase transition of nuclear matter. When the system undergoes a phase transition or approaches the critical point, the correlation length of the system diverges, causing inhomogeneity of the local baryon number density in the system. As the nucleon coalesce into light nuclei, the information related to the fluctuation of baryon number density is directly carried in the light nuclei yield. Based on the nucleon coalescence model, the yield of light nuclei strongly depends on the system volume and freeze-out temperature, so the yield of individual light nuclei is very dynamic and is not an effective observable to understand the dynamical evolution of the system. Otherwise, the compound yield ratio  $N_t \times N_p/N_d^2$  of light nuclei can cancel the overwhelming density and volume effects, and the possible nucleon density fluctuation hidden in the light nucleus yield has the chance of coming to the surface.

The Relativistic Heavy Ion Collider (RHIC) at Brookhaven National Laboratory in the United States is one of the large-scale experimental facilities for high-energy heavy-ion collisions in the world. Among them, the STAR experiment is dedicated to the experimental study of quark-gluon plasma properties and QCD phase structure under high temperature and high density conditions. The STAR detector consists of multiple particle detectors with different functions. Its core tracking section includes a cylindrical Time Projection Chamber (TPC) and a Time-of-Flight detector (TOF), which provide full azimuthal coverage and a large central rapidity region, as well as excellent particle identification capability. Since 2010, the STAR Beam Energy Scan (BES) program has collected data from Au+Au collision at center-of-mass energy range from 3 to 200 GeV, corresponding to a baryon chemical potential of 750 to 25 MeV. This energy range covers a wide range on the QCD phase diagram, providing an effective approach to experimentally study the QCD phase diagram. This thesis mainly introduces: (1) the production of triton in Au+Au collisions at  $\sqrt{s_{NN}} = 7.7, 11.5, 14.5, 19.6, 27, 39, 54.4, 62.4,$  and 200 GeV; (2) the extraction of the primordial proton transverse momentum spectra and integrated yields at all energies except 200 GeV; (3) the measurement of the nuclear compound yield ratio  $N_t \times N_p/N_d^2$  from 7.7-200 GeV. Enhancements

in the yield ratios relative to the coalescence baseline are observed in the 0%-10% most central collisions at 19.6 and 27 GeV, with a combined significance of  $4.1\sigma$ . The enhancements are not observed in peripheral collisions or model calculations without critical fluctuation. Theoretical predictions suggest that this non-monotonic behavior is closely related to the phase transition of nuclear matter and the QCD critical point, but there is still no definitive answer. This study systematically investigates the production of light nuclei in the first stage of the STAR BES-I, obtaining important experimental data for the measurement of heavy-ion collisions, including triton yields, primordial proton yields, and yield ratios within a wide energy range. The proposed new observations and experimental measurements provide fresh insights into the mechanisms of light nuclei production in heavy-ion collisions and the understanding of the QCD phase diagram.

The thesis focus on the measurement process of triton production, proton weak decay correction, and the ratio of light nuclei in the STAR BES-I. The relevant analysis methods, correction details, model comparisons, and discussions of physical significance will be presented one by one. The paper consists of the following chapters: Chapter 1 provides an introduction to the background of modern physics and the research motivation of this subject. Chapter 2 introduces the RHIC-STAR experimental setup, as well as the detectors and detection methods used in our study. Chapter 3 describes the measurement of triton in the STAR BES-I, providing a detailed explanation of the data analysis process and the final triton yield obtained. Chapter 4 addresses the weak decay of strange particles on the published proton yield of STAR, outlining the correction process, and providing the yield of primordial protons and the fraction of proton feed-down. Chapter 5 presents the final results of our measurements and relevant discussions. Finally, Chapter 6 provides a brief summary and outlook. Researching the production of light nuclei in heavy-ion collisions is of significant scientific importance as it helps to understand the mechanisms behind their formation and explore the QCD phase diagram.

**Keywords:** Relativistic heavy ion collision; QCD critical point; triton production; primordial proton yields; light nuclei compound yield ratio.

# List of Figures

1.1.1 History of the discovery of elementary particle. . . . .	3
1.1.2 Octets of baryons and (pseudo-scalar) mesons. Figure taken from [1]. . . . .	5
1.1.3 The standard model of elementary particles. The figure is from Ref. [2]. . . . .	6
1.2.1 Summary of measurements of strong coupling constant as a function of the energy scale $Q$ . The figure is from Ref.[3], P155. . . . .	8
1.2.2 The QCD phase diagram in terms of temperature and baryon chemical potential. The red line indicates a freeze-out line while the black line indicates the QCD phase transition boundary. The black open square is the conjectured QCD critical point. The figure is from Ref.[4]. . . . .	9
1.3.1 Simplified picture of a central collision of two high energy nuclei in the centre-of-mass frame. Colliding nuclei appear as thin discs due to Lorentz contraction. The figure is from Ref. [5]. . . . .	10
1.4.1 Binding energy per nucleon for a selection of nucleus <sup>1</sup> . . . . .	12
1.4.2 The cartoon shows the coalescence of nucleons. $p_0$ is the effective interaction radius. . . . .	13
1.4.3 In the vicinity of the critical point or the first order phase transition, density fluctuations become larger [6, 7]. . . . .	16
2.1.1 The Relativistic Heavy Ion Collider located in Brookhaven National Laboratory, USA. Accelerated heavy ions can collide at six intersection points on the RHIC ring. . . . .	19
2.2.1 Left: Perspective view of the STAR detector, with a cutaway for viewing inner detector systems. Right: Beam's eye view of a STAR detector. The event on the right side was drawn by the STAR level-3 online display <sup>2</sup> . . . . .	21



2.2.2 The time projection chamber of the STAR detector system. The collisions take place near the center of the TPC in collision model. . . . .	22
2.2.3 Pad plane layout for one super-sector. . . . .	23
2.2.4 Mass stopping power ( $-dE/dx$ ) for positive muons in copper as a function of $\beta\gamma$ over nine orders of magnitude in momentum. Vertical bands indicate boundaries between different approximations region. . . . .	24
2.2.5 The Time of Flight detectors are pink cylinders with patches covering the external cylindrical field cage of the TPC. <sup>3</sup> . . . . .	25
2.2.6 The time projection chamber of the STAR detector system. The collisions take place near the center of the TPC in collision model. . . . .	26
2.3.1 Left: In STAR simulation, the class <b>StMiniMcEvent</b> mainly stores the types of tracks, and different types of tracks are used for different physical analyses. Right: The tracks are stored in the form of a tree for the example of the decay of strange particle into proton in the STAR simulation. . . . .	28
3.1.1 The variation of $z$ position of event vertex in Au+Au collisions at $\sqrt{s_{NN}} = 7.7\sim 200$ GeV. . . . .	31
3.1.2 The variation of $x$ and $y$ position of event vertex in Au+Au collisions at $\sqrt{s_{NN}} = 7.7\sim 200$ GeV. . . . .	32
3.1.3 The example of tracks selection criteria for $\sqrt{s_{NN}} = 39$ GeV Au+Au collisions. . . . .	33
3.2.1 The cartoon example of the correlation of the final state observable $N_{ch}$ with Glauber calculated quantities ( $b, N_{part}$ ). Figure from [8]. . . . .	34
3.2.2 The distribution of TPC RefMult. . . . .	35
3.3.1 Energy loss $dE/dx$ as a function of rigidity for Au+Au collisions at $\sqrt{s_{NN}} = 7.7\sim 200$ GeV. Dashed lines correspond to the theoretical predicted values for different nuclei. The black line represent electron, from low to up is $\pi, k, \text{proton, deuteron, triton, and } ^3\text{He}$ respectively. . . . .	37
3.3.2 $m^2$ as a function of rigidity for Au+Au collisions at $\sqrt{s_{NN}} = 7.7\sim 200$ GeV. Dashed lines correspond to $m^2$ for different nuclei. . . . .	38
3.3.3 Triton phase space for Au+Au collisions at $\sqrt{s_{NN}} = 7.7\sim 200$ GeV. For example, triton at 19.6 GeV is selected by a cutoff criterion of $ z_t  < 0.2$ and $6.9 \leq m^2 \leq 8.9$ ( $\text{GeV}^2/c^4$ ). . . . .	40



3.3.4 The $z(t)$ distributions for triton from the TPC detector for different $p_T$ bins and 0-10% centrality in Au+Au collisions at $\sqrt{s_{NN}} = 39$ GeV. The curves are Gaussian fits. Errors are statistical only. . . . .	41
3.3.5 The $m^2$ distributions for triton in the TOF in Au+Au collisions at $\sqrt{s_{NN}} = 7.7$ GeV, 0-10%. The curves are Gaussian and exponential function fits. Errors are statistical only. . . . .	42
3.3.6 The $m^2$ distributions for triton in the TOF in Au+Au collisions at $\sqrt{s_{NN}} = 7.7$ GeV, 10-20%. The curves are Gaussian and exponential function fits. Errors are statistical only. . . . .	43
3.3.7 The $m^2$ distributions for triton in the TOF in Au+Au collisions at $\sqrt{s_{NN}} = 7.7$ GeV, 20-40%. The curves are Gaussian and exponential function fits. Errors are statistical only. . . . .	44
3.3.8 The $m^2$ distributions for triton in the TOF in Au+Au collisions at $\sqrt{s_{NN}} = 7.7$ GeV, 40-80%. The curves are Gaussian and exponential function fits. Errors are statistical only. . . . .	45
3.3.9 The $m^2$ distributions for triton in the TOF for different $p_T$ bins in Au+Au collisions at $\sqrt{s_{NN}} = 39$ GeV, 0-10%. The curves are Gaussian and exponential function fits. Statistical error only. . . . .	46
3.3.10 The $m^2$ distributions for triton in the TOF for different $p_T$ bins in Au+Au collisions at $\sqrt{s_{NN}} = 39$ GeV, 10-20%. The curves are Gaussian and exponential function fits. Statistical error only. . . . .	47
3.3.11 The $m^2$ distributions for triton in the TOF for different $p_T$ bins in Au+Au collisions at $\sqrt{s_{NN}} = 39$ GeV, 20-40%. The curves are Gaussian and exponential function fits. Statistical error only. . . . .	48
3.3.12 The $m^2$ distributions for triton in the TOF for different $p_T$ bins in Au+Au collisions at $\sqrt{s_{NN}} = 39$ GeV, 40-80%. The curves are Gaussian and exponential function fits. Statistical error only. . . . .	49
3.4.1 Efficiency $\times$ acceptance for reconstructed triton at $\sqrt{s_{NN}} = 39$ GeV in the TPC as a function of $p_T$ at mid-rapidity ( $ y  < 0.5$ ) in Au+Au collisions. The lines are fitting by the function shown in the text. . . . .	51



3.4.2	First row: Triton signal extraction from 200 GeV, the region of side-band is $m^2 \in [6.3, 7.1] \text{ \& } [8.7, 9.5] \text{ GeV}^2/c^4$ , the signal region is $7.1 < m^2 < 8.7 \text{ GeV}^2/c^4$ . Second row: normalized side-band $\times$ background counts. . . . .	52
3.4.3	TOF matching efficiency for triton as a function of $p_T$ at mid-rapidity ( $ y  < 0.5$ ) in Au+Au collisions at 39 GeV. The lines are fitting by the function shown in Eq. 3.4.3.	54
3.4.4	Left: The $p_T$ difference of reconstructed and embedded triton as a function of $p_T^{\text{rec}}$ in Au+Au collision at 39 GeV, 0-10% centrality. Middle: The energy loss of the triton as a function of collision centrality. Right: The energy loss of the triton as a function of collision energy. . . . .	55
3.4.5	DCA distributions of triton for $0.60 < p_T < 0.9 \text{ GeV}/c$ , $0.9 < p_T < 1.2 \text{ GeV}/c$ and $1.2 < p_T < 1.5 \text{ GeV}/c$ up to 3.9 GeV/c in 39 GeV Au+Au collisions. Errors shown are statistical only. The dashed curve is the fit triton background. The red circles are the scaled $\bar{t}$ distribution. . . . .	57
3.4.6	The DCA distribution of the triton in experimental measurements compared with that in embedding data at $\sqrt{s_{\text{NN}}} = 200 \text{ GeV}$ in Au+Au collision, 0-10% centrality. .	59
3.5.1	The relative systematic errors from different source for triton $p_T$ spectra in Au+Au collisions at $\sqrt{s_{\text{NN}}} = 39 \text{ GeV}$ . . . . .	61
3.5.2	The $p_T$ spectra was fitted using the method of parametric scan, left: contours returned by the parametric fit; right: distribution of the scanned parametric range function in green band. . . . .	63
3.5.3	Variation of the parameters and integral yields within the parameters one sigma error range. . . . .	63
4.2.1	Input Monte Carlo parent or parentparent particles spectra from Au+Au collision 0-10% centrality at 39 GeV. . . . .	68
4.2.2	Decayed proton from the embedding sample from Au+Au collision 0-10% at 39 GeV.	69
4.2.3	The primordial proton from total feed-down correction from Au+Au collision 0-10% at 39 GeV. . . . .	70
4.3.1	Mid-rapidity transverse momentum spectra for primordial protons. . . . .	71



4.3.2 The energy dependence of the weak decay feed-down fraction of proton yields at mid-rapidity estimated from the data-driven method. The black-filled circles and the black-open circles are the results of protons and (anti)protons, respectively. The black-shaded bands are the corresponding calculation from the MUSIC+UrQMD hybrid model [9]. Figure made by Dr. Nu Xu. . . . .	72
4.3.3 The energy dependence of the primordial proton yields at mid-rapidity estimated from the data-driven method (red filled squares) and UrQMD+GEANT (open squares). The black filled circles are inclusive protons. The ratio of the data-drive method to UrQMD+GEANT method is shown in the inner panel. . . . .	73
4.4.1 The decayed proton spectra fitted by different function. . . . .	75
4.4.2 Applying the same fit function to each individual particle spectra. . . . .	76
4.4.3 Upper: The $N_t \times N_p/N_d^2$ from the different fit function. Lower: The arithmetic mean and variance of the deviations. . . . .	77
5.1.1 Transverse momentum ( $p_T$ ) spectra for mid-rapidity ( $ y  < 0.5$ ) tritons from 0%-10%, 10%-20%, 20%-40%, and 40%-80% centralities in Au + Au collisions at $\sqrt{s_{NN}} = 7.7, 11.5, 14.5, 19.6, 27, 39, 54.4, 62.4,$ and 200 GeV. Dashed-lines are the corresponding Blast-Wave fits with the profile parameter $n = 1$ . The statistical and systematic uncertainties are shown as vertical lines and boxes, respectively. . . . .	79
5.2.1 Coalescence parameter $B_3$ as a function of transverse momentum scaled with the mass number ( $p_T/A$ ) for triton from 7.7 GeV (left panel) and 200 GeV (right panel) 0-10%, 10-20%, 20-40%, and 40-80% Au+Au collisions. The square brackets show systematic error and vertical lines show the statistical error separately. . . . .	80
5.2.2 Coalescence parameter $B_3$ as a function of collision energy at $p_T/A = 0.65$ GeV/c. . . . .	81
5.3.1 Blast-Wave function fit for triton spectra. Centrality dependence of 0-10% (left panel) and 10-20% (right panel) in Au+Au collisions at $\sqrt{s_{NN}} = 39$ GeV. . . . .	82
5.3.2 Centrality dependence of $dN/dy$ (upper panel) and $\langle p_T \rangle$ (lower panel) of triton in Au+Au collisions at $\sqrt{s_{NN}} = 7.7 \sim 200$ GeV. Errors shown are the statistical and systematic uncertainties separately. . . . .	83



5.3.3 Mass dependence of light nuclei yields (divided by the spin degeneracy factor) $dN/dy$ (upper panel) in Au+Au collisions at $\sqrt{s_{NN}} = 7.7 \sim 200$ GeV. Mass dependence of average transverse momentum $\langle p_T \rangle$ for the particles in Au+Au collisions at $\sqrt{s_{NN}} = 7.7 \sim 200$ GeV. . . . .	84
5.4.1 Collision energy dependence of the mid-rapidity ratios $N_d/N_p$ (blue solid square) and $N_t/N_p$ (red solid circles) from the top 0-10% central Au+Au collisions. Statistical and systematic uncertainties are shown as vertical lines and brackets, respectively. For comparison, results from FOPI [10], E864 [11], PHENIX [12, 13], and ALICE [14] are also shown. The solid and dashed lines are results from thermal model [15, 16] and MUSIC+COAL. model [9] calculations, respectively. . . . .	85
5.4.2 The yield ratio $N_t \times N_p/N_d^2$ as a function of charged-particle multiplicity $dN_{ch}/d\eta$ ( $ \eta  < 0.5$ ) in Au+Au collisions at $\sqrt{s_{NN}} = 7.7 - 200$ GeV for 0-10%, 10-20%, 20-40%, and 40-80% centralities. Statistical and systematic uncertainties are shown as vertical lines and brackets, respectively. . . . .	88
5.4.3 Collision energy, centrality, and $p_T$ dependence of the yield ratio $N_t \times N_p/N_d^2$ in Au+Au collisions at RHIC. . . . .	90
5.4.4 The yield ratio ( $N_t \times N_p/N_d^2$ ) as a function of charge particle multiplicity $dN_{ch}/d\eta$ in Au + Au collisions at $\sqrt{s_{NN}} = 7.7 - 200$ GeV from STAR and p+p 7 TeV, p+Pb 5.02 TeV, Pb+Pb 2.76 TeV from ALICE experiments. . . . .	92
6.2.1 Expected source for di-lepton productions as a function of invariant mass in ultra-relativistic heavy-ion collisions. . . . .	96
6.3.1 A view of the STAR detector with the BES-II upgrades highlighted. The EPD and iTPC are symmetric in STAR. The eTOF is only on the east side. . . . .	97
6.3.2 A summary of the good events acquired for the various collision energies (translated to $\mu_B$ ). The BES-II collider data sets are shown in red bars. The FXT data sets are shown in hashed blue bars. For comparison the BES-I data sets are shown in grey bars. . . . .	98

# List of Tables

3.1	Event cuts and total numbers of minimum bias events . . . . .	30
3.2	Tracks quality cuts applied to all energies . . . . .	33
3.3	Parameters for absorption correction . . . . .	56
3.4	Tracks cuts for systematic error. . . . .	60
3.5	Sources of percentage systematic uncertainties for triton spectra at 39 GeV, 0-10%. . . . .	62
4.1	Spectra data reference . . . . .	66

# Chapter 1

## Introduction

### 1.1 Elementary Particle and Standard Model

The exploration of the laws governing the microstructure of matter has been a fundamental question in the process of human scientific exploration of natural mysteries for centuries. As far back as the 4th century B.C., people have been studying the structure of matter. The ancient Greek pre-Socratic philosopher Democritus proposed the atomism, in which he named the basic elements or particles that make up matter “atom”. However, this was only a hypothesis rooted in a simple understanding of the natural world and lacked a rigorous scientific basis. In the early 19th century, English chemist and physicist John Dalton proposed the atomic theory, which explained many phenomena through the view that matter is made up of atoms. This theory achieved many successes, but Dalton considered atoms as “indivisible masses” of matter. This view was prevalent for a long time and represents a stage in the human understanding of the structure of matter. As scientific understanding deepened, it became clear that the atom was not the “last mass”, but was still separable and had a structure. Major discoveries at the end of the 19th century paved the way for this new understanding of matter. The history of the discovery of the elementary particle shown in Fig. 1.1.1. In 1895, Wilhelm Röntgen discovered X-rays. In 1896, Henri Becquerel accidentally discovered the radioactivity of matter when studying X-rays. In 1897, J.J. Thomson concluded that cathode rays were composed of electrons. These three discoveries ushered in a new era in the study of the structure of matter, leading to a flourishing situation where the study of the microstructure of matter progressed from the atomic lamina to the atomic nucleus level, and



eventually to the elementary particle level.

In 1910, Ernest Rutherford devised the famous  $\alpha$  particle scattering experiment that established the fundamental nuclear model of atomic structure [17]. Four years later in 1914, Niels Bohr proposed a model of the hydrogen atom consisting of an electron orbiting a proton, similar to a planet moving around the sun. Bohr based his model on the opposing charges between the proton and electron which causes them to be mutually attracted to each other, supporting the electron in its orbit. Further utilizing the principles of early quantum mechanics, Bohr was able to calculate the atomic spectrum of hydrogen resulting in data consistent with experimental observations. However, this poses a challenge for atoms like  ${}^4\text{He}$ , which carries only two electrons but has a mass four times greater than that of hydrogen atom. This problem found its resolution with James Chadwick's discovery of the neutron [18], paving the way for the final understanding of classical elementary particle physics, which established that matter is comprised of protons, neutrons, and electrons. However, one difficult question remains unresolved, which is how the nucleons are held together? From this period of classical understanding of elementary particle physics, superlative concepts upholding the gravitas of Hideki Yukawa's Meson, Paul Dirac's Positron, and Wolfgang Pauli's Neutrino emerged.

The positively charged protons experience a strong repulsion from each other due to their electrical charge. Despite this, they remain bound together in the nucleus of an atom, indicating that there is a force stronger than electrical repulsion binding them together. This force is regarded by physicists as one of the fundamental forces of nature, and it is known to be the strongest force. However, due to its short range, it can only act over a distance equivalent to that of a nucleon. The first theory of the strong force was proposed by Yukawa in 1934. He suggested that protons and neutrons are attracted to each other by a field, similar to the way electrons are attracted to atomic nuclei by the electric field. Yukawa went ahead to calculate the quantum nature of this field, and his calculations resulted in the discovery of mesons. Mesons were particles that had a mass approximately equivalent to  $1/6$  of a proton or 300 times that of an electron, and subsequent research found the existence of other similar particles in cosmic rays. This discovery of additional particles between the electron and the proton underscores the complexity and richness of subatomic physics, and ongoing research is shedding more light on the structure of matter at its elementary level.

During the early stages of exploring elementary particles, non-relativistic quantum mechanics was already established, but developing relativistic quantum mechanics based on it was a challenge.

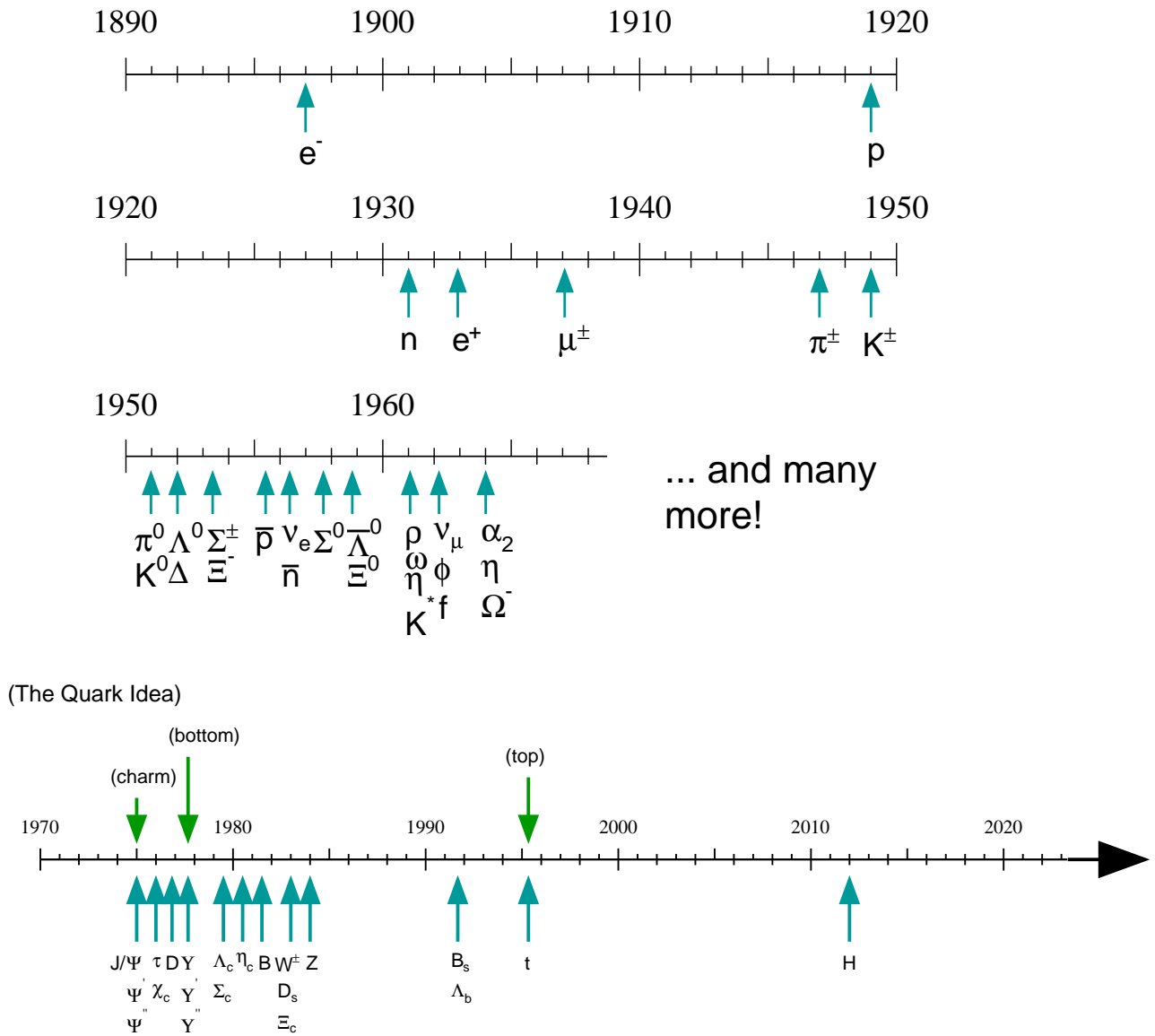


Figure 1.1.1: History of the discovery of elementary particle.



The first outstanding achievement was Dirac's discovery of the equation named after him in 1927, which is used to describe the free electron as given by the relativistic formula. In the initial calculations, the electron energies had a problematic feature: for each positive energy solution, there was a negative energy solution corresponding to it. At the end of 1931, Carl David Anderson discovered positive charges in cosmic rays, which meant that Dirac's theory had won a spectacular victory. Furthermore, in 1930, scientists studying the nuclear  $\beta$  decay discovered that the change from radioactive nuclide A to the slightly lighter nuclide B and the release of an electron was contrary to the law of conservation of energy. In response to this, Pauli proposed that the end state of  $\beta$  decay there is another electrically neutral particle emitted at the same time, which Fermi later called neutrino. In the mid-1950s, experiments on the "inverse"  $\beta$  decay provided conclusive evidence for the existence of neutrinos, and the law of conservation of leptonic number was introduced. During this period, scientists discovered many previously undiscovered particles in cosmic rays, such as  $K^0 \rightarrow \pi^+ + \pi^-$ ,  $K^+ \rightarrow \pi^+ + \pi^+ + \pi^-$ ,  $\eta$ ,  $\phi$ ,  $\omega$ , among others. The discovery of  $\Lambda$ ,  $\Xi$ ,  $\Sigma$  and many other baryons in the 1950s and 1960s, as well as the operation of the first modern accelerator (Brookhaven National Laboratory's synchrotron), led to the conclusion that there is a law of baryon conservation. However, this period also highlighted the dilemma faced by physicists in exploring elementary particles, where the original simple few particles developed into what seemed to be chaotic many particles. To find a way forward, physicists remembered Dmitri Mendeleev's periodic table of elements and set out to discover the "periodic table" of elementary particles.

Murray Gell-Mann, the Mendeleev of elementary particles, is credited with introducing the concept of the octet in 1961. This state involves arranging baryons and mesons into different geometries based on their charges and strange number. Specifically, the eight lightest baryons are arranged in a hexagonal square, with two in the center, in a similar manner, the eight lightest mesons can be arranged to form a hexagonal pattern, known as the (pseudo-scalar) meson octet, as depicted in Fig. 1.1.2. The discovery of the  $\Omega$  particle in 1964 was a significant breakthrough in the understanding of elementary particles, demonstrating the accuracy of the octet state and decuplet state predicted by Gell-Mann. Subsequently, Gell-Mann and George Zweig independently proposed that all hadrons are actually composed of more fundamental components, which Gell-Mann named quarks [19]. Quarks come in three types, forming triangular octet states:  $u$  (for up) carries charge  $2/3$  and has strange number 0;  $d$  (for down) carries charge  $-1/3$  and has strange number 0; and  $s$  (for strange) carries charge  $-1/3$  and has strange number  $-1$ . Each quark has

an antiquark counterpart, carrying the opposite charge and strange number. Combinations of these quarks adhere to specific rules: baryons consist of three quarks, while mesons consist of one quark and one antiquark. This model allows scientists to classify existing particles easily, and even predict the existence. The quark model was originally met with skepticism due to its apparent contradiction with the Pauli exclusion principle. This principle states that no two particles with half-integer spin, including quarks, can occupy the same state. This appeared to conflict with the fact that the same quarks compose both the  $\Delta$  and  $\Omega$  particles. However, in 1964, Oscar W. Greenberg introduced the concept of color, which posited that quarks have not only three flavors, but also three colors [20]. It was suggested that all naturally existing particles are colorless, which solved many of the problems previously encountered. For instance, it explained why particles comprising two or four quarks were not possible and why a single quark could not exist in nature.

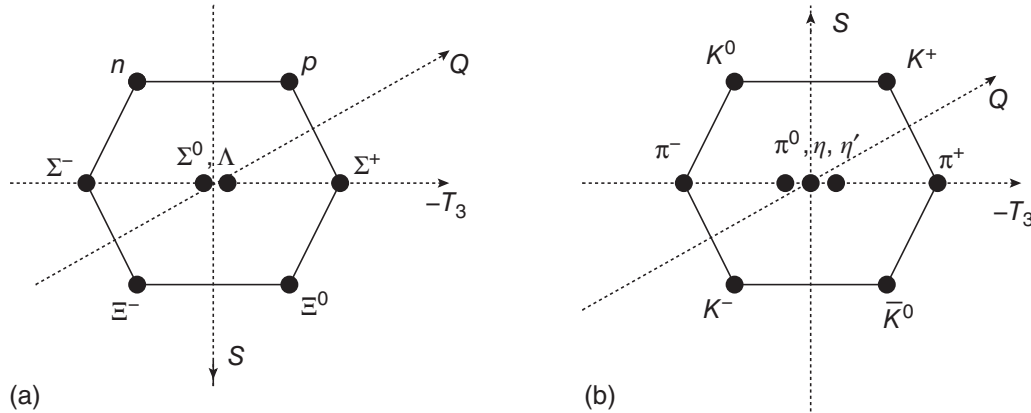


Figure 1.1.2: Octets of baryons and (pseudo-scalar) mesons. Figure taken from [1].

In the summer of 1974, a team led by Samuel C. C. Ting discovered the  $J/\psi$  meson at Brookhaven National Laboratory. The discovery was kept a secret until November of the same year, when the Burton Richter group at the Stanford Linear Accelerator Center (SLAC) independently discovered the new particle. Both teams then published their results at the same time, revealing the discovery of the  $J/\psi$  particle. After its discovery, there was significant discussion and debate around the properties of this particle. Eventually, the explanation that the  $J/\psi$  was composed of a new kind of quark,  $c$  and  $\bar{c}$ , won out. While the fourth flavor quark was predicted by physicists years ago, the discovery of a quark with a single  $c$  confirmed the existence of the fourth generation quark,



leading to a restoration of the quark model to its former status. The discovery of the  $\tau$  leptons in 1975 and the  $\Upsilon$  baryons two years later expanded the number of leptons to six and confirmed the existence of the  $b$  quark. As the collider continued to develop, the  $t$  quarks were also confirmed in the laboratory until 1995. Overall, these discoveries marked significant advancements in the field of particle physics and expanded our understanding of the building blocks of the universe.

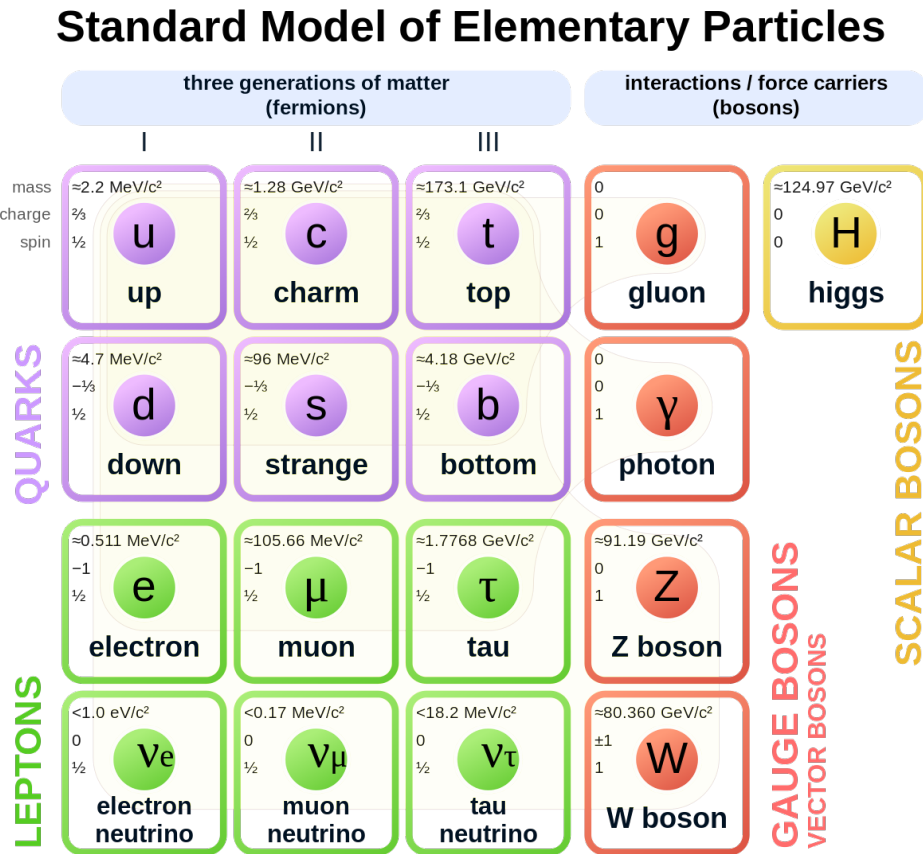


Figure 1.1.3: The standard model of elementary particles. The figure is from Ref. [2].

An interaction accomplished by exchanging certain particles, this posed a new challenge in understanding weak interactions, where both theoretical predictions and experiments were difficult to explore the mediator particles that transmit interactions. Theoretical physicists Tsung-Dao

Lee and Chen-Ning Yang did a literature review on the question of parity conservation in all fundamental interactions. They concluded that in the case of the weak interaction, experimental data neither confirmed nor refuted conservation of parity. The discovery of parity violation in the weak interaction through the Chien-Shiung Wu experiment in 1956 prompted a search for a way to relate the weak and electromagnetic interactions [21]. The electroweak theory of Sheldon Glashow, Steven Weinberg, and Abdus Salam finally solidified the theoretical predictions, and it was not until 1983 that the particles, known as vector intermediate bosons, were confirmed in the laboratory, with a mass almost 100 times that of the proton, reflecting a triumph of human technology. In 2013, CERN made the groundbreaking announcement of the discovery of the Higgs particle, which had been predicted for over half a century, and is considered the last piece of the puzzle of the Standard Model, as shown in Fig. 1.1.3. The establishment of the Standard Model marks a milestone victory, but it raises the question of what the next steps are in the development of particle physics.

## 1.2 Quantum Chromodynamics(QCD) Phase Diagram and Critical Point

In 1935, Yukawa proposed that the strong binding force between protons and neutrons in the nucleus was due to the exchange of an unknown type of meson, a concept later confirmed by the existence of  $\pi$  meson. The strong interaction is similar to the electromagnetic interaction, but with a different mediator. While charge  $e$  marks the strength of electromagnetic interaction,  $g$  marks that of the strong interaction. However, experiments measuring nuclear force have revealed that the effective interaction strength is much larger than 1 with  $\frac{g^2}{4\pi} \approx 14$ , compared to the electromagnetic interaction with  $\frac{e^2}{4\pi} = 1/137$ . Consequently, perturbation theory, which is applicable only when the strength is much less than 1, has been abandoned. S-matrix theory and group theory, which do not depend on perturbation expansions, have emerged as alternatives. In 1967, deep inelastic scattering experiments by SLAC discovered Bjorken scaling, indicating that electrons at large momentum transfer were interacting with many free point particles within protons, which R. Feynman called partons. Further studies showed that partons were valence quarks and sea quarks (quark-antiquark pairs). As momentum transfer increases, the very strong interactions between quarks become weak, displaying an asymptotic free characteristic. Effective coupling constants are defined for strong interactions as follows



$$\alpha_s(Q^2) = \frac{g_s^2}{4\pi} = \frac{4\pi}{\beta_0 \ln \frac{Q^2}{\Lambda^2}} \quad (1.2.1)$$

where  $\beta_0$  is a one-loop  $\beta$  function, encodes the running of a coupling parameter,  $N_f$  is the quark flavor number, and  $\Lambda$  is the QCD scale. It is evident from the above equation that with an increase in energy  $Q^2$ , the strong interaction coupling constant  $\alpha_s$  decrease, which refers to the interaction between quarks tends towards 0. This finding quantitatively depicts the nature of strong interaction. Several years of experimental tests and theoretical advancements have demonstrated the validity of this theory, as illustrated in Fig. 1.2.1. This suggests that the QCD theory has entered the phase of precise verification and development.

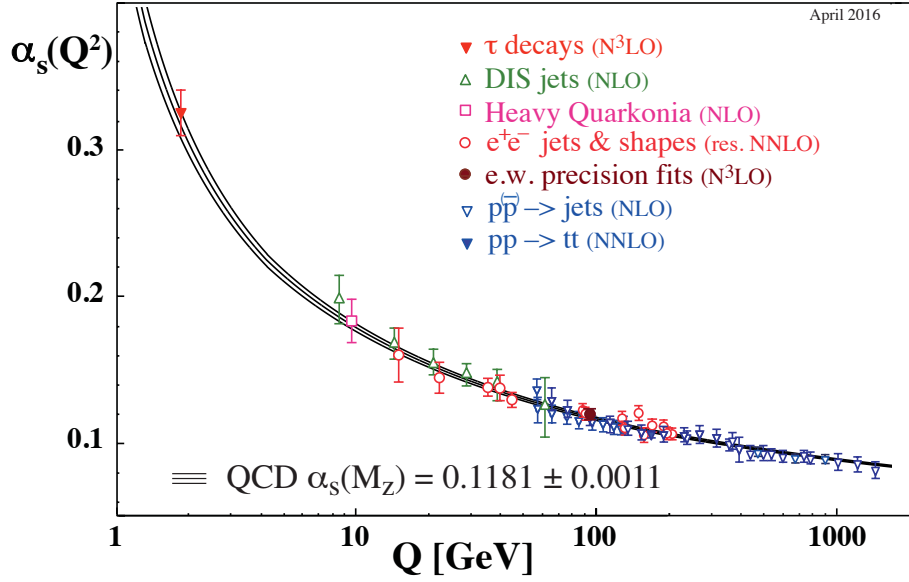


Figure 1.2.1: Summary of measurements of strong coupling constant as a function of the energy scale  $Q$ . The figure is from Ref.[3], P155.

In ordinary conditions, quarks are confined among hadrons and exhibit color neutrality, thereby making free quarks unobservable. However, when the energy density is high enough or the medium reaches a sufficiently high temperature, the color charge will be revealed from the tightly confined state due to the extremely environment. This process leads to a new state of matter that

we call the Quark-Gluon Plasma (QGP), which has been shown to be produced in experiments located at RHIC and LHC. The QCD phase diagram shown in Fig. 1.2.2 depicts the transition between hadronic matter and the QGP at varying baryon chemical potential and temperature. At high temperature and vanishing baryon chemical potential ( $\mu_B = 0$  MeV), Lattice QCD calculations reveal that the transition between hadronic matter and QGP is a smooth crossover and occurs at a temperature of  $T_c = 156$  MeV [22, 23]. Conversely, QCD-based model calculations suggest that there is a first-order phase transition at large baryon chemical potential, which should end at a critical point (CP) toward the crossover region [24, 25, 26, 27, 28, 29]. If the theoretical predictions hold, the phase transition line of first order is expected to terminate at a CP near the crossover region. A key challenge is to identify experimentally the location of this CP in the QCD phase diagram at finite baryon density. The experimental detection of this critical point would constitute a major achievement in the quest to unravel the QCD phase structure.

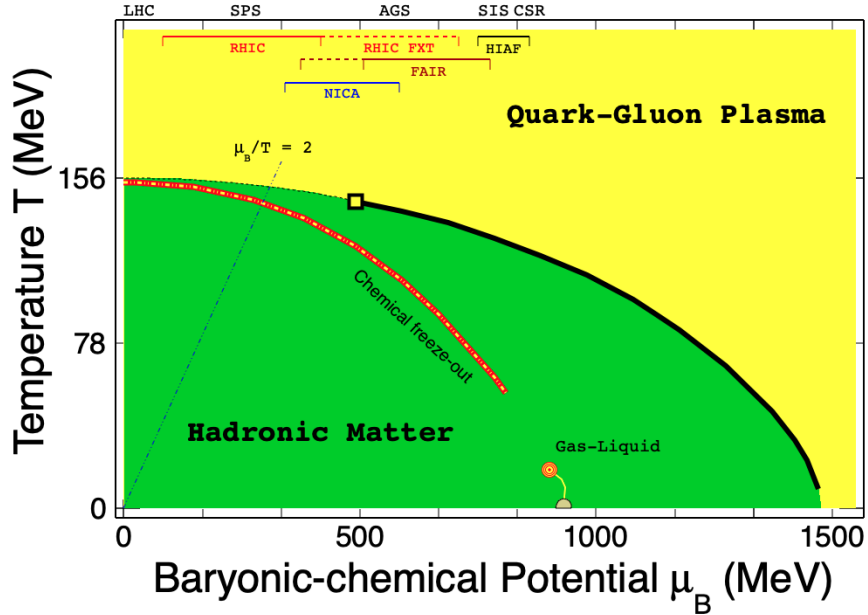


Figure 1.2.2: The QCD phase diagram in terms of temperature and baryon chemical potential. The red line indicates a freeze-out line while the black line indicates the QCD phase transition boundary. The black open square is the conjectured QCD critical point. The figure is from Ref.[4].



### 1.3 Relativistic Heavy Ion Collision (HIC)

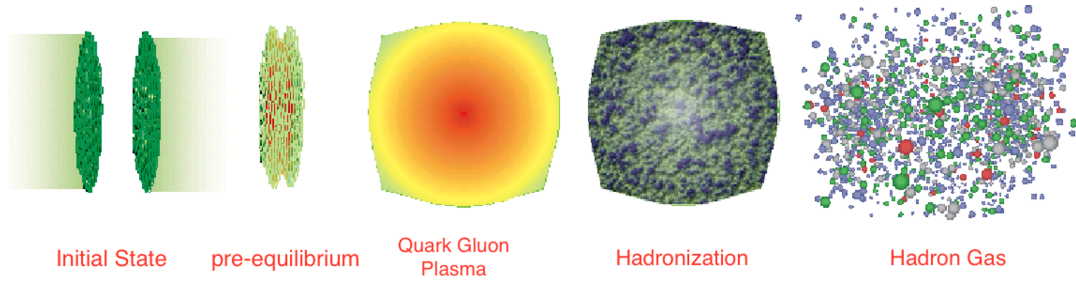


Figure 1.3.1: Simplified picture of a central collision of two high energy nuclei in the centre-of-mass frame. Colliding nuclei appear as thin discs due to Lorentz contraction. The figure is from Ref. [5].

Relativistic heavy-ion collisions offer an effective method to study strong interactions. When two nuclei moving close to the speed of light collide, or collide in a fixed target mode, the enormous energy deposited at the center of the collision produces thousands of new particles. The identification of these end-state particles, as well as their kinematic characteristics, provides new insights into elementary particles and their interactions. The space-time evolution of relativistic heavy-ion collisions can be roughly divided into several processes as shown in Fig. 1.3.1, the first of which occurs under the nucleon center-of-mass reference frame of two colliding nuclei close to the speed of light, during which the colliding nuclei become Lorentz-contracted, similar to the overlap of two discs. In the central collision region, the energy density reaches the highest, leading to the creation of a new state of matter known as QGP, in which the system consists of gluons saturated in phase space. During the initial  $1 fm/c$ , the quantum fluctuation of the classical field is considered the reason for the system achieving spatial anisotropy as well as local thermalization, while after a few  $fm/c$ , the system reaches local thermalization. With the expansion and cooling of the QGP, the quarks combine into hadrons, which is the beginning of the hadronization phase. The initially produced hadrons have high energy, and the inelastic collisions start to stop at a short time after hadronization, which is also known as the chemical freeze-out of the system. Following the chemical freeze-out, the chemical components of the system remain unchanged, and only the decay of resonance and annihilation of positive and negative particles can alter the particle yields. The multiple scattering between hadrons is elastic collisions after the chemical freeze-out, and a collective flow continues to build up until the average distance between hadrons exceeds the range

of their interactions. At this point, all collision has ceased, which is referred to as kinetic freeze-out, and free hadrons move towards the detectors [30, 31]. The identification and kinematical characteristics of these end-state particles will provide new insights into elementary particles and their interactions.

## 1.4 Light Nuclei Production in HIC

### 1.4.1 Importance of Light Nuclei Production

Light nuclei are relatively stable nuclei consisting of two or more nucleons, typically containing no more than 40 nucleons, also known as nucleon clusters. These nuclei are generally classified according to the number of nucleons and the binding energy, as illustrated in Fig. 1.4.1. The binding energy of a nucleus reflects the tightness of the binding between protons and neutrons, and is best measured by the average binding energy of each nucleus. Measurements show that the average binding energy is slightly greater than 8.6 MeV for nuclei with mass numbers ranging from 40-120, but is smaller than 8.6 MeV for nuclei with mass numbers outside of this range. Light nuclei are significant objects of study in low-energy (Projectile energy  $E < 30$  MeV), intermediate-energy ( $50 \text{ MeV} < E < 1 \text{ GeV}$ ) nuclear physics, and high-energy heavy-ion collisions [32]. Despite being seemingly simple nucleon systems, especially in the non-relativistic approximation, the two-body problem can be solved rigorously. However, the study of light nuclei becomes more complex as more nucleons are introduced, enabling the exploration of nuclear forces and the discovery of rich nuclear structures.

In nucleon-nucleon collisions, when the energy per nucleon in the momentum center-of-mass system exceeds about 20 MeV, the nucleon is shattered, leading to multiple end-state particles due to induced nuclear reactions. Any final state is allowed, as long as the charge and baryon numbers are conserved. Among the end-states, the relative abundance of neutrons, protons, deuterons, tritons, etc., is not significantly restricted by energy, momentum, and angular momentum conservation. In high-energy heavy-ion nuclear reactions, the excess energy, momentum, and angular momentum are carried by the various nuclei in the final state. Therefore, it is impossible to enumerate the ways in which end-states are combined, especially when larger nuclei are involved. As a result, to understand the mechanism of light nuclei formation, we first need to conduct a large

---

<sup>1</sup>[https://en.wikipedia.org/wiki/Nuclear\\_binding\\_energy](https://en.wikipedia.org/wiki/Nuclear_binding_energy)

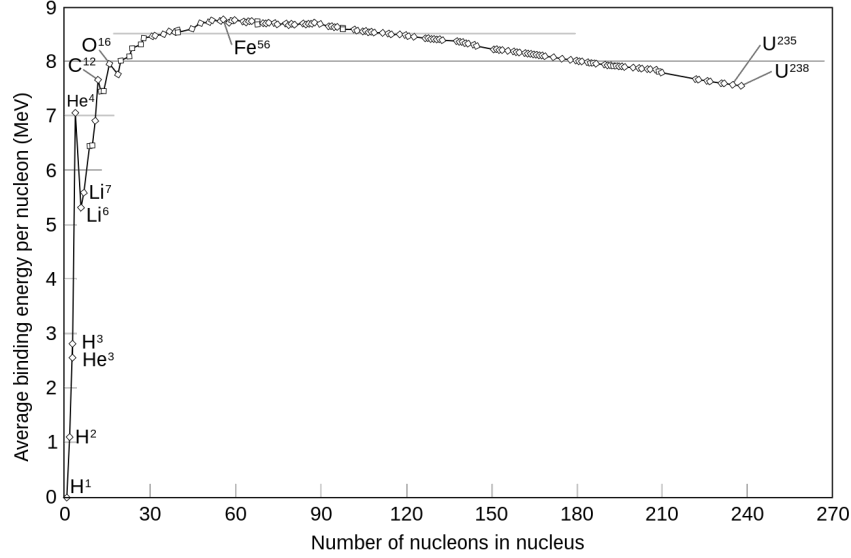


Figure 1.4.1: Binding energy per nucleon for a selection of nucleus<sup>1</sup>.

number of studies on the reaction and states of proton-nucleus. Deuterons are the most representative light nuclei product in proton-nucleus reactions and thus, the easiest pathway for studying the mechanism. The proton-neutron pair production kinetics into deuterons in collisional nuclear reactions is a fundamental part of this study. Specifically, the interaction of the field excited by the proton-neutron pair with other nuclear matter in the final state and the nuclear forces between the proton-neutrons allow them to combine into stable deuterons. Similar principles apply to clusters of light nuclei with more nucleons.

## 1.4.2 The Formation Mechanism of Light Nuclei in HIC

Over more than fifty years of research and development, many theories have been proposed to better understand the process of light nuclei formation in HIC. Out of these, two theories that have shown significant success are the nucleon coalescence model and thermodynamic statistical model. In the case of the coalescence model, perturbation theory has been introduced among theoretical physicists for calculations. The core mechanism of the coalescence model is that the probability of cluster formation is determined by the inner product of the Wigner function of the cluster in phase space and the freeze-out distribution function of each component particle in phase

space. Such as, the momentum space density of deuterons can be represented as a square of the distribution of nucleon number density. The correlation coefficient that arises here is related solely to the binding energy of the nucleon and the optical potential of the nucleus, while also being a momentum-dependence factor and a Lorentz-invariant quantity. This simple model offered a relatively effective prediction for heavy-ion experiments in the past century [33]. However, with nuclear physics experiments becoming ever-more complex, the coalescence model has occasionally resulted in discrepancies that scientists have attributed to other mechanisms, such as quasi-elastic knock-out of clusters or indirect nucleon dissociation. These effects have continued to appear in nucleon collision experiments, underscoring the importance of continued research and development in this area [34, 35, 36].

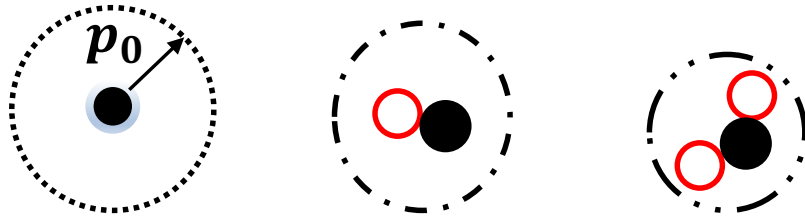


Figure 1.4.2: The cartoon shows the coalescence of nucleons.  $p_0$  is the effective interaction radius.

The proposed idea that the formation of deuterons in proton-nucleus reactions is independent and their momentum distribution should be proportional to the product of the proton and neutron momentum distributions has been discussed based on phase space. The nuclei density in momentum space is proportional to the proton density times the probability of finding a neutron within a small sphere of radius  $p_0$  around the proton momentum as shown in Fig. 1.4.2. In this context,  $p_0$  is a momentum-dependent parameter that is experimentally determined, and not predicted by the model. However, it has been proposed that this parameter applies only to a small momentum interval, and can be interpreted either as the Fermi momentum of the target nucleus or as the meson mass that mediates its interaction. When nuclei collide at high energies, a significant amount of the longitudinal momentum (in the beam direction) is converted into excitation energy during the nuclear reaction. However, when it comes to violent heavy-ion collisions, referring to a static nucleon optical potential does not hold much meaning. Therefore, the validity of kinetic models in high-energy heavy-ion collisions is brought into question. The coalescence mechanism



in high energy heavy-ion collisions has been studied extensively, with particular attention paid to the phase space reasoning of the mechanism. A formula for nucleon coalesce related to the number of nucleons,  $A$ , has been developed, with coefficients varying according to the specific situation. However, subsequent experiments on coefficients measurements and corrections have revealed that the ratio between observed nuclear fragmentation and original proton momentum distribution is often not accurate, as the actual data show a distribution between observed nuclear fragmentation and observed proton momentum. Furthermore, the coalescence model does not provide insights into the dynamics of nucleon coalesce, such as how the coalescence parameter changes depending on nuclear fragmentation, nucleus-target combination, or beam energy.

The collision of large nuclei in the center results in the compression and excitement of nuclear matter at enormous energies. While the correlation between nucleons is likely to be greater in higher density nuclear matter, the presence of clusters of light nuclei is still unclear. The time scale for independent nucleons to coalesce into light nuclei is assumed to be higher than the interparticle collision rate, and the sudden approximation in quantum mechanics is used to estimate the probability of forming clusters from  $Z$  protons and  $N$  neutrons,  $N = A - Z$ . The Wigner function distribution of nucleons in phase space is used to form the wave functions of light nuclei, including the position and momentum of their internal wave functions. Late studies have shown that this mechanism is similar to the coalescence model in the phase space structure [37]. When assuming the distribution of all nucleons in phase space is uniform, it takes the form of the coalescence model, like the given formula.

$$E_A \frac{d^3 N_A}{d^3 p_A} = B_A \left( E_p \frac{d^3 N_p}{d^3 p_p} \right)^Z \left( E_n \frac{d^3 N_n}{d^3 p_n} \right)^{A-Z} \approx B_A \left( E_p \frac{d^3 N_p}{d^3 p_p} \right)^A \quad (1.4.1)$$

where  $E_p \frac{d^3 N_p}{d^3 p_p}$  is the Lorentz-invariant momentum distribution of proton before coalescence into nuclear fragments,  $A$  is the mass number,  $Z$  is the proton number.  $p_A = Ap_p$ . The coalescence parameter  $B_A$  reflects the probability of nucleon coalescence, which is related to the nucleon freeze-out correlation volume [38, 39].

Followed by the introduction of the thermodynamic model assumption. After the high temperature and high density nuclear matter expansion ceases, the system reaches a state of chemical equilibrium among the proton, neutron, and light nuclei. As time progresses, the elastic collisions between particles completely disappear, causing all particles to move along a straight line trajectory until they reach the detector. The temperature of the system, the chemical potential of the

protons and neutrons, and the volume  $V$  can be used to describe the state of the system after freezing and dissociation. States consistent with the conservation of charge and baryon numbers are populated based on the Boltzmann factor in the statistical mechanics partition function. It should be noted that the conservation law still holds even if the nucleus under consideration is not in the ground state.

For a multicomponent hadron gas system with volume  $V$  and temperature  $T_{ch}$ , the particle multiplicity density is

$$N_i/V = \frac{g_i}{(2\pi)^3} \gamma_S^{S_i} \int \frac{1}{\exp(\frac{E_i - \mu_B B_i - \mu_S S_i}{T_{ch}}) \pm 1} d^3p \quad (1.4.2)$$

where  $N_i$  is the abundance of particle species  $i$ ,  $g_i$  is the spin degeneracy,  $B_i$  and  $S_i$  are the baryon number and strangeness number, respectively,  $E_i$  is the particle energy, and the integral is taken over all momentum space. The model parameters are the chemical freeze-out temperature ( $T_{ch}$ ), the baryon ( $\mu_B$ ) and strangeness ( $\mu_S$ ) chemical potentials, and the strangeness suppression factor ( $\gamma_S$ ). Usually, we use the statistical model THERMUS [40] and assume that the system can be represented by a Grand Canonical Ensemble in HIC.

### 1.4.3 Neutron Density Fluctuation - The Light Nuclei Compound Yield Ratio

Similar to the critical opalescence phenomenon observed in the liquid-gas phase transition, when the system reaches its critical point, the correlation length of the system diverges, causing the wavelength of the incident light to be comparable to the correlation length, leading to enhanced light scattering [41]. The production of matter in relativistic heavy-ion collisions can lead to a large baryon number density fluctuation when the conditions of its system reach a first-order phase transition or vicinity of the critical point. The correlation length increases dramatically near the critical point, leading to a density rise in the number of baryons formed, which reaches a maximum. If this density rise can be retained during the hadron evolution of heavy-ion collisions, there should be a strong fluctuation in the nucleon number density, resulting in a significant inhomogeneity in the phase space distribution of the end-state particles during chemical freezing, as shown in Fig. 1.4.3. Based on the nucleon coalescence model, the theory predicts that the production of light nuclei is directly related to the fluctuation of the system in local baryon number density. The yields of deuteron and triton are simply given by Eq. 1.4.3

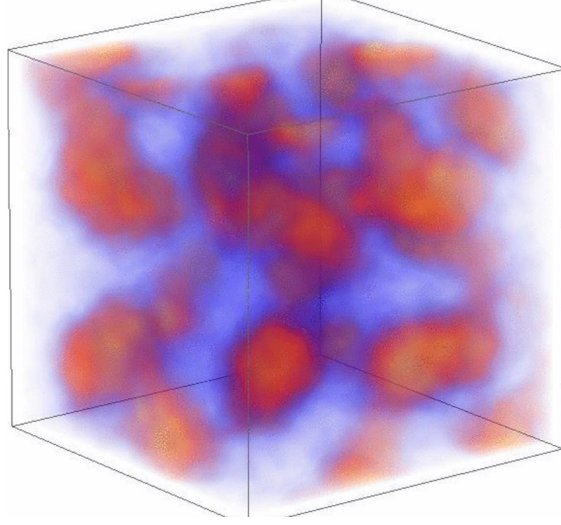


Figure 1.4.3: In the vicinity of the critical point or the first order phase transition, density fluctuations become larger [6, 7].

$$N_d = \frac{2}{2^{1/2}} \left( \frac{2\pi}{m_0 T_{eff}} \right)^{3/2} N_p \langle n \rangle (1 + \alpha \Delta n) \quad (1.4.3)$$

$$N_t = \frac{3^{3/2}}{4} \left( \frac{2\pi}{m_0 T_{eff}} \right)^3 N_p \langle n \rangle^2 [1 + (1 + 2\alpha) \Delta n] \quad (1.4.4)$$

where  $\langle . \rangle$  denotes the average value over space,  $m_0$  is rest mass of the nucleon,  $\alpha$  being the correlation coefficient for proton and neutron,  $\Delta n = \langle (\delta n)^2 \rangle / \langle n \rangle^2$  is a dimensionless quantity that characterizes the relative density fluctuation of neutrons. The ratio of the compound yields,  $N_t \times N_p / N_d^2$ , where  $N_p$  is the primordial proton yield,  $N_d$  is the deuteron yield, and  $N_t$  is the triton yield, is proportional to the neutron density fluctuation of the system evolves [42, 43, 44]. Based on the coalescence model, we understand that the production of light nuclei is strongly dependent on the nucleon emission volume and kinetic freeze-out temperature of the system, which makes their yields highly dynamic, influenced by the nucleon density and system volume. This dynamism makes it challenging to spot any anomalies in the yield of deuteron and triton, without considering the intricate details of the system's dynamic evolution. To cancel out the overwhelming effect of density, volume and etc., we need to take the yield ratios  $(N_t \times N_p / N_d^2)$ . This cancellation provides

a chance for the nucleon density fluctuation hidden in the light nuclei yield to come to the surface.

The nucleon coalescence model and neutron density fluctuation, along with preliminary measurements by the STAR Collaboration [45], have provided theoretical predictions about the potential effects on the production of light nuclei as the system approaches the QCD critical point. These effects are predicted when the system lifetime is sufficiently long in relation to the nucleon coalescent time, and when quantum effects affecting the interaction of several nuclei at finite temperatures are taken into consideration. To further investigate this phenomenon, additional measurements of the light nucleus compound yield ratios are proposed, which may provide more insight into the enhancement due to the fluctuation of the baryon number density. Specifically, the ratios  $N_\alpha \times N_p / N_{^3\text{He}} \times N_d$ ,  $^3\text{He}$  and  $\alpha$  will be included in these measurements [46, 47, 48, 49].

## 1.5 Thesis Motivation

The purpose of this thesis is to systematically measure the production of light nuclei in the STAR BES-I. The main work consists of two major parts. The first part involves the measurement of triton production, the second part involves the proton feed-down correction from the strange particles weak decay. The ultimate goal of this research is to extract the light nuclei compound yield ratio ( $N_t \times N_p / N_d^2$ ) and discuss the associated physics based on the gathered data. The first phase beam energy scans were conducted by the STAR collaboration between 2010 and 2017. During this time, Brookhaven National Laboratory collected critical experimental data, specifically for the final state particle in Au+Au collisions model, with the leading energies of  $\sqrt{s_{\text{NN}}} = 7.7, 11.5, 14.5, 19.6, 27, 39, 62.4, \text{ and } 200 \text{ GeV}$  under the center-of-mass frame. Additionally, this study includes measurements of the light nuclei and primordial proton of 54.4 GeV produced in 2018.

The triton yield measurements were carried out in a thorough process that involved the entire data analysis process of the STAR experiment. This included selecting relevant data, events and tracks selection, particle identification, extracting signals, correcting for detector efficiency, estimating errors, discussing results and making physical assessments. However, due to the rarity of triton particles, a certain level of statistical requirements had to be met for this analysis. This led to some difficulties in the signal extraction process during the BES-I analysis. To address this, we used various methods such as adjusting bin widths, transforming fitting functions, bin counting and more. We also took into account the systematic uncertainties associated with this aspect in our final results. As a part of triton comes from the beam pipe and detector material, we



carried out a signal background subtraction. This involved using the signal distribution of the anti-triton, under the assumption of no knock-out of the anti-triton, for the background subtraction of triton. However, it is worth noting that anti-triton are largely unmeasured at low energies. As a result, the acceptance of the signal extraction in our measurements has some limitations, starting from transverse momentum greater than 1.2 GeV/c. In heavy-ion collisions, strange baryons and their (anti)particles, which include  $\Lambda$ ,  $\Sigma^+$ ,  $\Xi^0$ ,  $\Xi^-$ , and  $\Omega^-$ , undergo weak decay, resulting in the production of (anti)protons. The primordial yields of (anti)protons are often analyzed to study the properties of the hot dense medium formed in such collisions. However, to obtain accurate results, it is essential to subtract the (anti)protons produced through weak decay contributions from the inclusive yields. A data-driven method has enabled a smooth correction process.

The main objective of this study was to evaluate the ratio of light nuclei compound yields through the formula  $N_t \times N_p / N_d^2$ . Although the research had some challenges, the data necessary to calculate the ratio was obtained successfully. However, there were difficulties in estimating the systematic error. To address this problem, the researchers engaged in methodological discussions, and as a result, they were able to estimate the systematic error by implementing five fit functions to each individual particle spectra using the same function for all particles. The researchers varied the yield and ratio with distinct functions to derive the difference in the ratio. It was concluded during this phase that the primary source of error was the unmeasured interval, and there was a connection between these errors in the energy-dependent distribution. Therefore, the final error was divided into two parts: energy-dependent correlated and random.

Our research findings demonstrate interesting and important results regarding the energy-dependent light nuclei compound yield ratio in central collisions. We observed a non-monotonic behavior that was not seen in peripheral collisions or models without a critical point. Our study employed the coalescence model, which revealed that the yield of light nuclei strongly depends on the nucleon emission volume and kinetic freeze-out temperature of the system. We recognize that the yield of light nuclei is dynamic and closely associated with the nucleon density and system volume. This makes it challenging to identify any anomaly in the yield of deuteron and triton without knowing the specifics of the dynamical system evolution. We utilized the yield ratios of  $N_t \times N_p / N_d^2$  to cancel out the overwhelming density and volume effects, allowing the possible nucleon density fluctuation hidden in the light nuclei yield to surface. Further studies are necessary to determine whether the enhancements seen in heavy-ion collisions are attributable to large baryon density fluctuations near the critical point.

## Chapter 2

# Experiment Setup

### 2.1 Relativistic Heavy Ion Collider

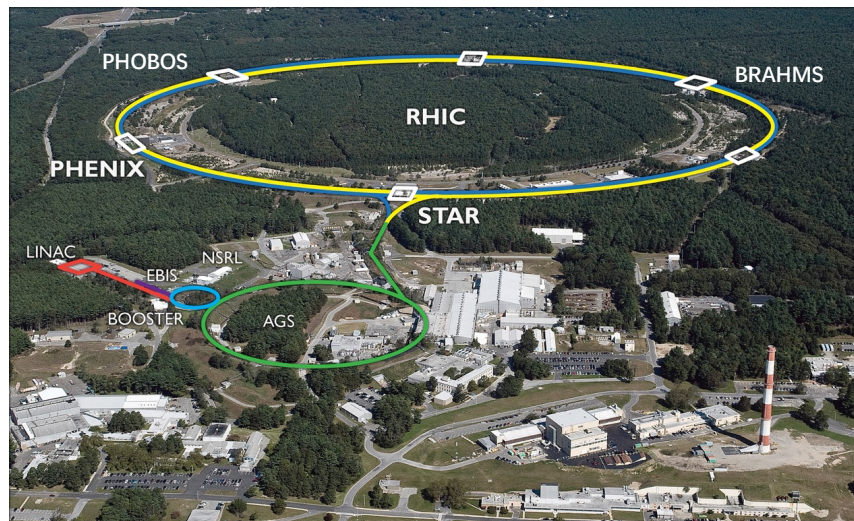


Figure 2.1.1: The Relativistic Heavy Ion Collider located in Brookhaven National Laboratory, USA. Accelerated heavy ions can collide at six intersection points on the RHIC ring.



The Relativistic Heavy Ion Collider (RHIC) at Brookhaven National Laboratory on Long Island <sup>1</sup> is considered the highest brightness proton spin-polarization collider in the world shown as in Fig. 2.1.1 [50]. This machine plays a crucial role in enabling physicists to study the high energy density and high temperature matter produced microseconds after the Big Bang. The project, which began in 1991 and completed in 1999, and it includes four detectors, namely, BRAHMS, PHENIX, PHOBOS, and STAR <sup>2</sup>. RHIC is a cross-storage ring particle accelerator that contains two hexagonal-shaped storage rings (“yellow” and “green”) with a circumference of 3834 m. The particles in these storage rings are deflected and focused using 1749 superconducting magnets. The bird’s eye view of RHIC, as shown in Fig. 2.1.1, includes six intersections at the midpoint of each of the six sides where particles can collide. Additionally, the entire process of accelerating gold atoms at RHIC is multi-stage, involving electron stripping outside the nucleus and the use of several accelerators, including the Electron Beam Ion Source (EBIS) accelerator, the small Booster, and the Alternating Gradient Synchrotron (AGS). Finally, the gold nucleus, with a +79 charge, is injected into the storage ring through a beam line into the two rings of RHIC [51]. Since its operation in 1999, RHIC has been an incredibly successful operation, enabling researchers to gather valuable information about the universe’s formation.

In January 2020, the U.S. Department of Energy announced its plans to construct an Electron Ion Collider (EIC) <sup>3</sup> at BNL. Consequently, the STAR experiment conducted on the RHIC ring will soon come to an end, marking a significant chapter in history. However, the announcement also means that the RHIC ring will be assigned a new mission, and they assert that “While advancing the state of the art of particle colliders, the EIC will enable the U.S. nuclear physics community, with world-wide participation, to take a giant step forward in the centuries-old quest to understand the nature of matter at its most fundamental level, providing the clearest picture yet of how the elemental quarks and gluons interact to form the basic structure of atoms and nuclei.” [52].

## 2.2 STAR Detector System

The STAR detector is a crucial component of heavy-ion collision detection systems on the RHIC ring and is one of the few such systems in the world. It is situated at 6 o’clock on the

---

<sup>1</sup><https://www.bnl.gov>

<sup>2</sup><https://www.star.bnl.gov>

<sup>3</sup><https://www.bnl.gov/eic/>

<sup>4</sup><https://www.bnl.gov/rhic/images.php>

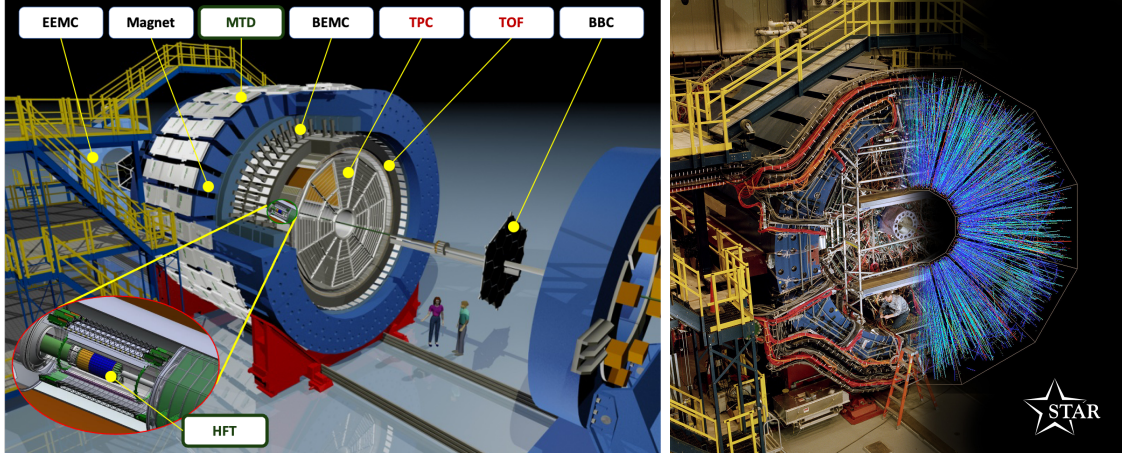


Figure 2.2.1: Left: Perspective view of the STAR detector, with a cutaway for viewing inner detector systems. Right: Beam's eye view of a STAR detector. The event on the right side was drawn by the STAR level-3 online display<sup>4</sup>.

ring and has a very large uniform acceptance and azimuthal angle covering the mid-rapidity. Fig. 2.2.1 provides a visual representation of the STAR detector. The primary objective of the STAR experiment is to investigate whether a new state of matter exists at extremely high energy density and to examine the QCD phase structure. The experiment is on the lookout for indications of the presence of the QGP phase transition and the underlying nature of strong interactions at high energy densities by simultaneously measuring various observables. To achieve this goal, the detector is designed to measure hadron products at a wide solid angle, with a focus on particle identification and momentum analysis using high spatial and time resolution.

### 2.2.1 Time Projection Chamber

The Time Projection Chamber (TPC) serves as the primary tracking device at STAR, as depicted in Fig. 2.2.2. It has been designed to record particle trajectories and provide relevant information about particle momentum and ionization energy loss ( $dE/dx$ ) as the particle passes through the TPC gas. STAR's TPC is currently the second-largest in the world, situated in a large solenoidal magnet operating at 0.5 T. It has a cylindrical geometry with one central membrane cathode and two end-caps, covering about  $\pm 1$  units of pseudorapidity ( $\eta$ ) and the full azimuthal

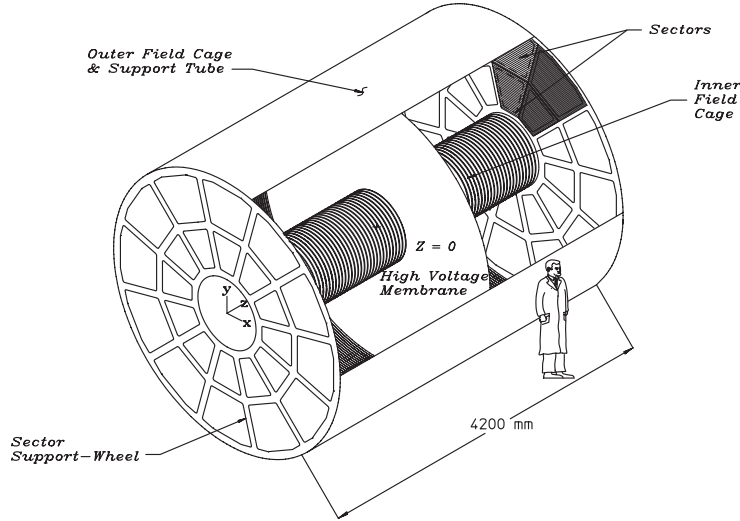


Figure 2.2.2: The time projection chamber of the STAR detector system. The collisions take place near the center of the TPC in collision model.

angle coverage ( $0 < \phi < 2\pi$ ). The entire TPC is divided equally into left and right parts by the central membrane, which can reach a high voltage of  $28 \text{ kV}$ . The field cage is a  $4.2 \text{ m}$  long cylinder that is  $4 \text{ m}$  in diameter, containing 183 resistive and equipotential rings along the inner and outer field cages of the TPC, which create a uniform drift electric field ( $135 \text{ V/cm}$ ). The end-caps contain thin-gap, Multi-Wire Proportional Chambers (MWPCs) with a pad plane readout surface on the outermost cathode surface. Each TPC end-cap is divided into 12 identical super-sectors, each of which comprises an outer sector and an inner sector. The outer sector has 3940 rectangular pads of  $6.2 \text{ mm}$  by  $19.5 \text{ mm}$  in size, which are arranged in 32 rows. The inner sector has 1750 rectangular pads of  $2.85 \text{ mm}$  by  $11.5 \text{ mm}$  arranged in 13 rows, as shown in Fig. 2.2.3 [53]. For each segment of an ionized track, the primary signal electrons are multiplied by avalanches near the anode wires. The amplitudes of these signals are digitized as a function of time, and the measurement of drift time allows determination of the  $z$ -coordinate (perpendicular to the MWPCs and parallel to the RHIC beam), while the pads provide the  $(x, y)$  coordinates (perpendicular to the beam). This three-dimensional tracking capability of a TPC allows the determination of individual momenta of charged particles by tracking them through a solenoidal magnetic field and identifying them with

multiple energy-loss ( $dE/dx$ ) measurements. The sensitive volume of the TPC contains P10 gas (10% methane, 90% argon) regulated at 2 mbar above atmospheric pressure. The drift velocity of electrons in this gas is relatively fast, at 130 V/cm, and generally stable at 5.45 cm/ $\mu$ s. Charged particles can be identified by the TPC in a wide range of the transverse momentum from 0.15-30 GeV/c, and if the magnetic field is reduced to 0.25 T, the lowest lower limit of particle momentum is 0.075 GeV/c.

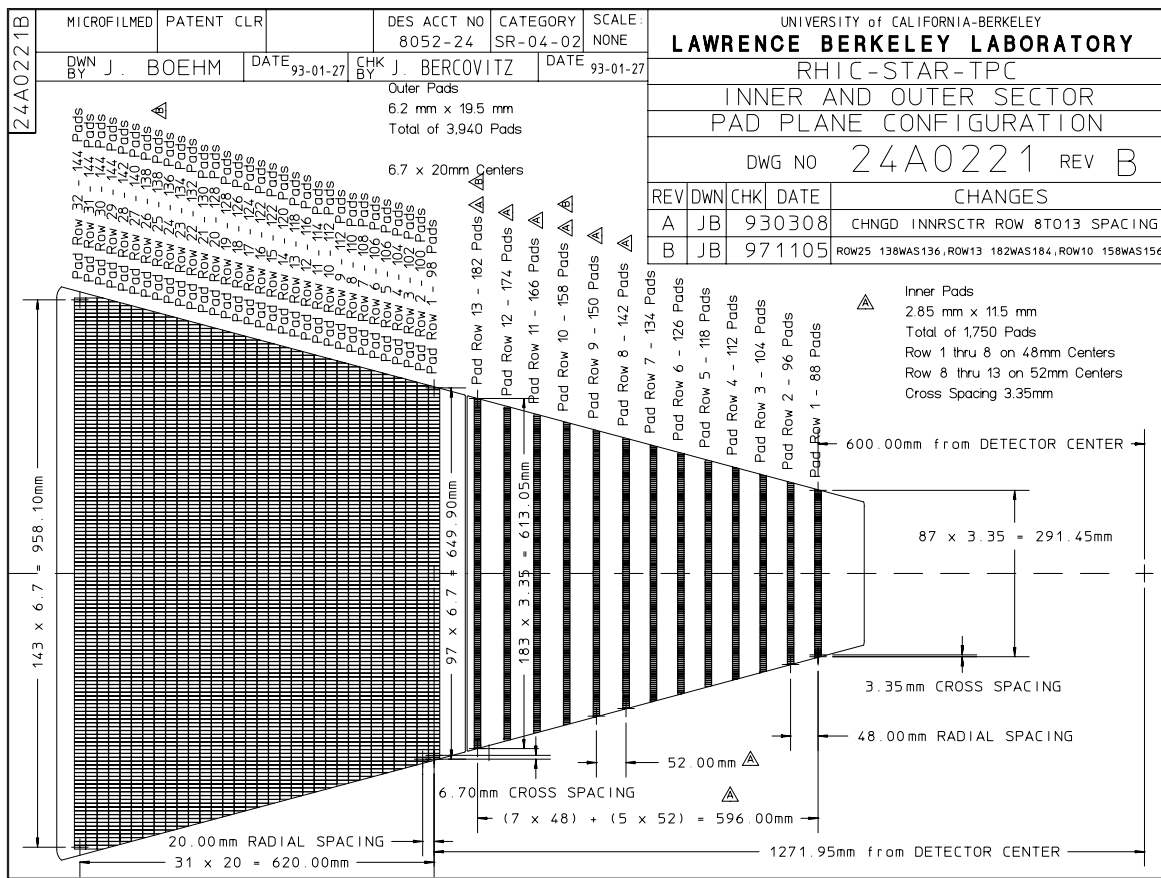


Figure 2.2.3: Pad plane layout for one super-sector.

In the STAR experiment, the Bethe-Bloch equation is utilized to calculate the theoretical energy loss that is experienced by a charged particle while passing through the STAR TPC. The



energy loss is commonly referred to as the mass stopping power and can be expressed using the following equation [3]

$$-\frac{dE}{dx} = Kz^2 \frac{Z}{A} \frac{1}{\beta^2} \left[ \ln \frac{E_{kin}^{max}}{I} - \beta^2 - \frac{\delta}{2} \right] \quad (2.2.1)$$

where  $K = 4\pi N_A r_e^2 m_e c^2$  is a constant equal to  $0.307075 \text{ MeV mol}^{-1} \text{ cm}^2$ ,  $z$  represent the charge number of the incident particle,  $Z$  and  $A$  is the atomic number of absorber and atomic mass of absorber,  $E_{kin}^{max}$  is the maximum transfer kinetic energy transferred from the incident particle to the stationary electron.  $I$  is the average excitation energy, is the density effect correction parameter. The Fig.2.2.4 shows as an example, the mass stopping power for a positive muons in copper as a function of  $\beta\gamma = p/Mc$  over nine orders of magnitude in momentum. For the STAR TPC, the main operating work in the Bethe range.

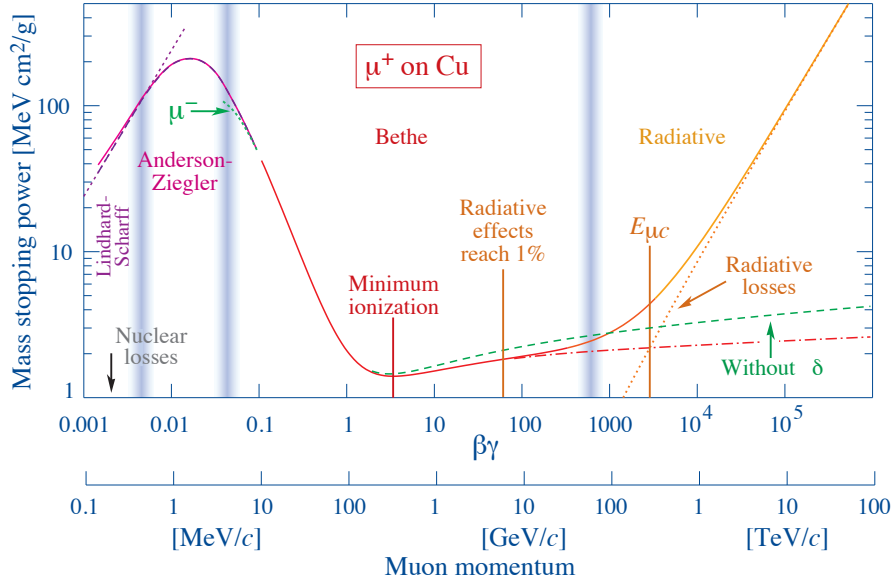


Figure 2.2.4: Mass stopping power ( $-dE/dx$ ) for positive muons in copper as a function of  $\beta\gamma$  over nine orders of magnitude in momentum. Vertical bands indicate boundaries between different approximations region.

### 2.2.2 Time of Flight

The STAR detector in the high momentum interval has been enhanced with the proposed barrel Time of Flight (TOF) detector, which was implemented in the STAR experiment in 2010 [54, 55]. The TOF detector is based on the Multi-gap Resistive Plate Chamber (MRPC) technology and is mounted in the outer cylinder of the TPC installation. It is made up of a total of 120 trays, 60 on each side of the east and west, with each tray containing 34 modules. The TOF detector covers a range of pseudo-rapidity ( $\eta$ ) of 0.9, as well as the azimuthal angle coverage with  $2\pi$ . The TOF intrinsic time resolution is 80 ps, and particle identification by TOF can significantly improve the identification of particles with high transverse momentum. It should be noted that the start time of the TOF system is provided by the vertex detector upVpd. Fig. 2.2.5 shows the TOF detector, and Fig. 2.2.6 shows the side view of each MRPC module schematic.

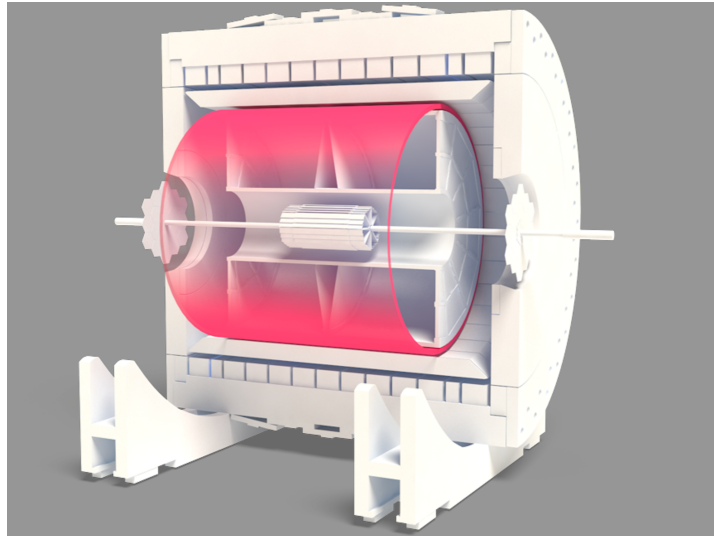


Figure 2.2.5: The Time of Flight detectors are pink cylinders with patches covering the external cylindrical field cage of the TPC. <sup>5</sup>

The MRPC is a resistive plate chamber that operates in avalanche mode. The gas gap in the MRPC is divided into multiple small gas gap cells by a series of resistive plates, which are “transparent” to the induced signal generated by the gas avalanche. The STAR MRPC module has

<sup>5</sup><https://nsw.org/projects/bnl/star/sub-systems.php>



six gas gaps of  $220 \mu\text{m}$  operating at  $14 \text{ kV}$  with a gas mixture 95%  $\text{C}_2\text{H}_2\text{F}_4$  and 5% iso-butane at 1 atmosphere. The onset time of the time-of-flight (TOF) detector is determined by the pseudo-vertex position detectors (pVPD) on both sides, which are located  $5.4 \text{ m}$  from the center of TPC along the beam pipe. The starting time resolution is corrected to  $85 \text{ ps}$ . TPC detector is used to obtain the path length ( $L$ ) and momentum ( $p$ ) of the particle. The velocity of flight  $\beta$  as well as particle mass  $m$  are then calculated by

$$\beta = \frac{L}{ct} \quad (2.2.2)$$

$$m^2 = p^2 \left( \frac{1}{\beta} - 1 \right) \quad (2.2.3)$$

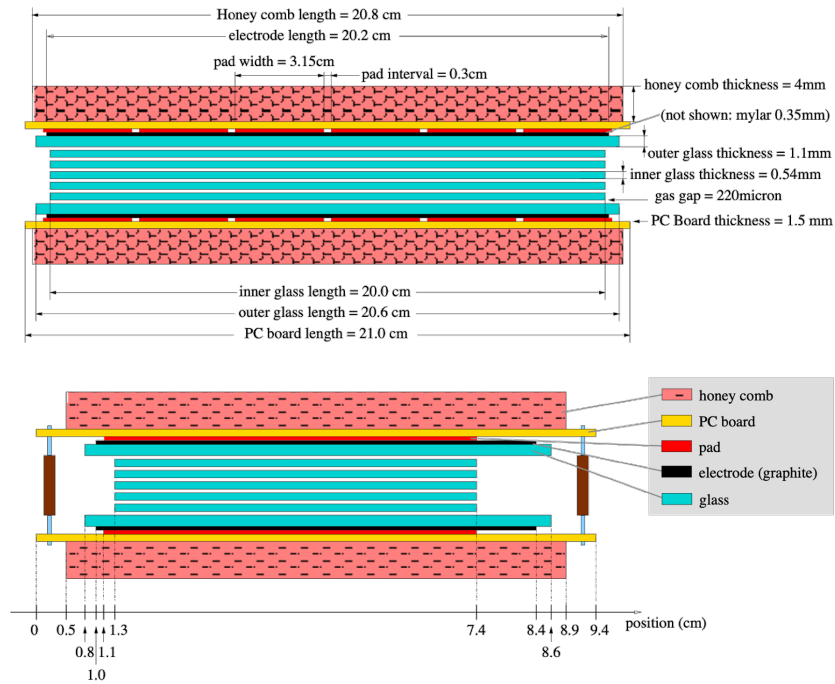


Figure 2.2.6: The time projection chamber of the STAR detector system. The collisions take place near the center of the TPC in collision model.

## 2.3 Simulation of STAR Experiment

**GSTAR/Starsim** is a simulation framework that is used for STAR detectors using GEANT<sup>6</sup> simulation package. The **Starsim** package currently includes multiple modules that consist of the geometries of different sub-detectors, beam pipe, vertex detectors, TPC, etc. Additionally, it also contains execution tasks under user control such as i/o, particle generation, on-flight analysis, and other operational programs. We should note that in the current case, there are may be reference to **GSTAR** which was a prototype for the current system - **Starsim**. Due to the large degree of backward compatibility in **Starsim**, all previously known information remains valid. Procedures that are experiment specific are used to read event generator information, detector geometries, new particles properties and decays, definition of hits are then compiled into shared libraries and loaded in the framework for execution.

The **StMiniMcMaker** package is highly relevant in our analysis as it provides data on the acceptance efficiency of the sub-detector TPC and the simulation data on the weak decay of strange particles into protons. **StMiniMcMaker** is essentially responsible for filling in the classes in **StMiniMcEvent**, which are used to store basic information about the simulated and reconstructed tracks for both embedded and fully simulated events (e.g. Hijing + GEANT + TRS). The trees in the output file are then used to make the histograms needed for efficiencies. The output file contains eventwise information at the top level and several branches for each event. The Monte Carlo tracks are saved in their individual trackwise branch so that all of the original Monte Carlo information is available. The other branches are pairwise, with each entry representing a pair of tracks: one MC and one Reconstructed. For the reconstructed tracks, important information like the global track parameters, the primary track parameters, the number of fit points, etc., are stored. On the other hand, For the Monte Carlo tracks the GEANT ID, four momentum, number of MC tpc hits, etc., is stored. In addition, pairwise information, e.g. the number of common hits between the tracks found by the association maker is stored in several pairwise branches which are used for different purposes [56]:

- MC Tracks: Holds all Monte Carlo tracks in the event. Uses class **StTinyMcTrack**.
- Matched Pairs: Holds MC track to primary track matches. Uses class **StMiniMcPair**, which inherits from **StTinyMcTrack** and from **StTinyRcTrack**, and adds additional information.

---

<sup>6</sup><https://geant4.web.cern.ch>



- Contamination Pairs (weak decay products, secondary tracks): Holds MC tracks that are not daughters of the primary vertex that are matched to reconstructed primary tracks. This happens when a MC that can come from a decay or from a secondary interaction is deemed by the tracking software to come from the reconstructed primary vertex. Uses class **StContamPair**.
- ...

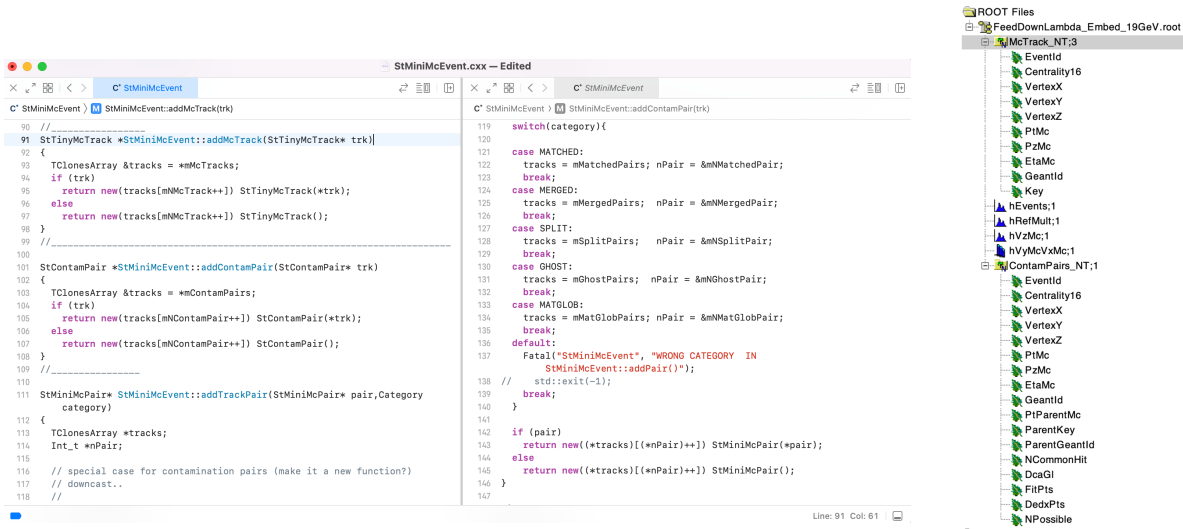


Figure 2.3.1: Left: In STAR simulation, the class **StMiniMcEvent** mainly stores the types of tracks, and different types of tracks are used for different physical analyses. Right: The tracks are stored in the form of a tree for the example of the decay of strange particle into proton in the STAR simulation.

The remaining tracks in this class have not been individually listed. Fig. 2.3.1 partially displays the MC tracks and Contamination pairs analysis code utilized to determine the correction for proton weak decay feed-down. On the right-hand side, the information retained in various tracks after data reading is visible, enabling identification and tracing of every track for the extraction of pertinent physical information.

# Chapter 3

## Analysis Details for Triton

### 3.1 Data Set

In this analysis, data was collected by the STAR experiment at RHIC for Au+Au collisions at  $\sqrt{s_{\text{NN}}} = 7.7, 11.5, 14.5, 19.6, 27, 39, 54.4, 62.4$  and 200 GeV. The 7.7, 11.5, 39, and 62.4 GeV data were collected in 2010, the 19.6, 27, and 200 GeV data were collected in the year 2011, while the 14.5 GeV data were collected in 2014. Moreover, the 54.4 GeV data were collected in 2018 with high statistical significance, colleague Hui Liu completed this part of the work [57]. The data set was obtained using a minimum bias trigger, which was defined by a coincidence of hits in the zero degree calorimeters (ZDCs) [58], vertex position detectors (VPDs) [59], and beam-beam counter (BBCs) [60, 61]. For this analysis, two sub-detector were used. The first one was the Time Projection Chamber (TPC) [53], and the second one was Time of Flight (TOF) [54]. These detector systems of the STAR experiment provide tracking and identification of triton ( $t$ ) and other charged hadrons. The number of events for each center of mass energy, its trigger and event cuts are shown in Table 3.1. The detailed analysis procedure using these detectors is given in the following subsections.

Prior to conducting physical analysis, the aforementioned data underwent a thorough evaluation to ensure that only good runs were included, called run-by-run Quality Assurance (QA) in the official centrality definition of STAR. The selection process involved from the event level, like Refmult,  $V_z$ ,  $V_r$ , from the track level, like  $p_T$ ,  $\phi$ ,  $\eta$ , **DCA**, and other variables for run-by-run QA. These variable depend on the runID are obtained, and some of the outlier events are excluded.



Table 3.1: Event cuts and total numbers of minimum bias events

Energy(GeV)	Trigger ID (minimum bias)	Vr(cm)	Vz (cm)	Event(M)
7.7	290001,290004,290003	2	40	2.37
11.5	310004,310011,340021,310013	2	40	8.52
14.5	440001,440004,440005,440006, 440007,440015,440016,440017	1	40	16.69
19.6	340001,340011,340021,340012,340022	2	40	19.64
27	360001,360002	2	40	38.41
39	280001,280002	2	40	116.78
54.4	580021	2	40	566.15
62.4	270001,270011,270021,270005	2	40	61.69
200	350003,350013,350023,350033,350043	2	30	465.07

For the remaining data, the mean and standard deviation were calculated, and typically  $\pm 3\sigma$  was chosen as a good runs. The process ensures that the selected data is of high quality and reliable, and can be used for further analysis. In our analysis, the data were produced at relative early, we have not included the details of this procedure as it has been covered in the centrality section 3.2.

### 3.1.1 Event Selection

To determine the primary vertex for each event, the most probable point of the common origin of the tracks measured by TPC is found. The distributions of  $V_z$  are presented in Fig. 3.1.1, represent the results presented are analyzed from minimum bias events of Au+Au collisions, occurring within  $\pm 30$  cm for 200 GeV and  $\pm 40$  cm for other energies of the nominal interaction point along the beam axis. The lower energy vertex distribution is flat while that at great than 39 GeV is peaked. The wide  $z$ -vertex distribution at lower energies is due to the fact that the beam is more difficult to focus at lower energy. The transverse  $x, y$  positions of the primary vertices in 7.7~200 GeV Au+Au collisions are shown in Fig. 3.1.2. In order to reject background events involving interactions with the beam pipe of radius 3.95 cm, the event vertex radius (defined as  $\sqrt{V_x^2 + V_y^2}$  where  $V_x$  and  $V_y$  are the vertex positions along the  $x$  and  $y$  directions) must be within 2 cm and 1 cm for 14.5 GeV. These values are chosen in order to achieve uniform detector performance and sufficient statistical significance of the measured observables.

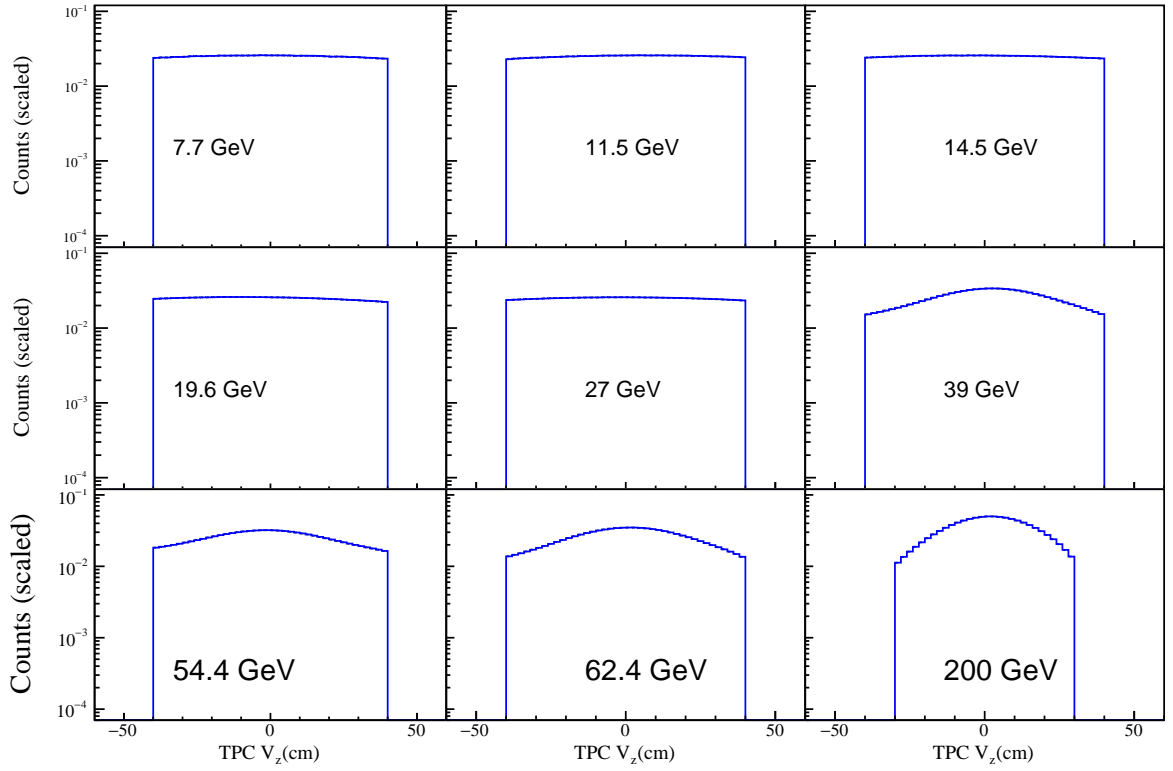


Figure 3.1.1: The variation of  $z$  position of event vertex in Au+Au collisions at  $\sqrt{s_{NN}} = 7.7 \sim 200$  GeV.

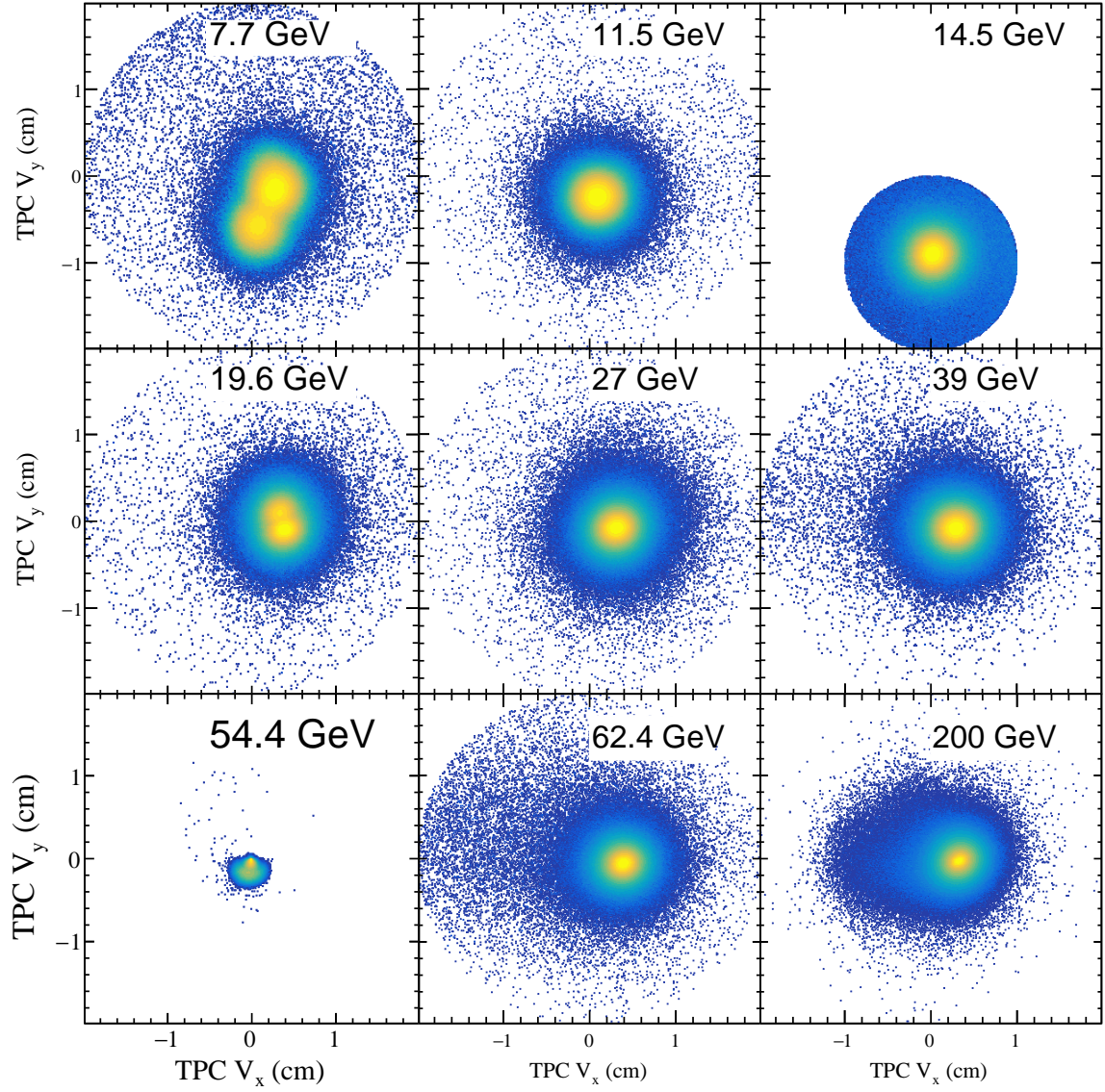


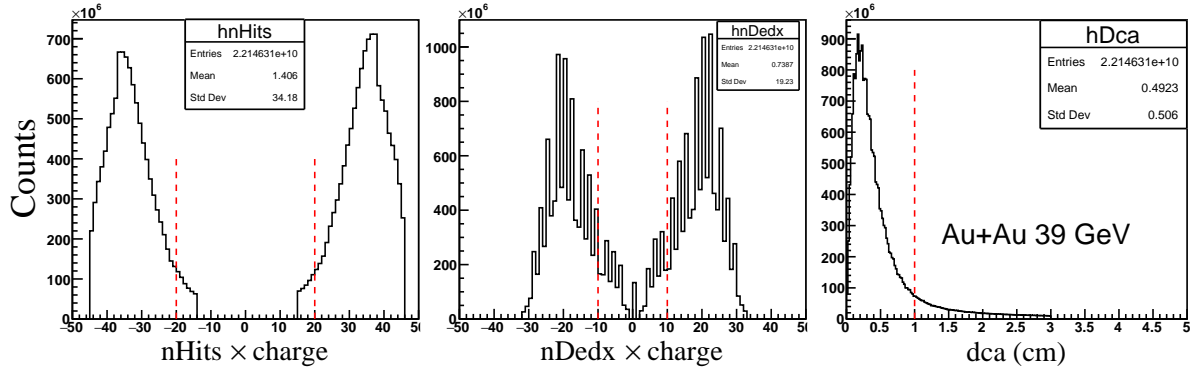
Figure 3.1.2: The variation of  $x$  and  $y$  position of event vertex in Au+Au collisions at  $\sqrt{s_{NN}} = 7.7\sim 200$  GeV.

### 3.1.2 Track Selection

Table 3.2: Tracks quality cuts applied to all energies

nHits	nHits/nHitsposs	ndEdxHits	DCA	$ \eta $	$ y $	$p_T$
$> 20$	$> 0.52$	$> 10$	$< 1$ cm	$< 1$	$< 0.5$	$> 0.2$ GeV

Table 3.2 shows the track quality cuts for all nine energies. To avoid the mixing of tracks from secondary vertices, a requirement of less than 3 cm is placed on the distance of closest approach (DCA) between each track and the event vertex. Moreover, tracks must have at least 25 points used in track fitting out of the maximum of 45 hits possible in the TPC, as depicted in Fig. 3.1.3. To prevent multiple counting of split tracks, at least 52% of the total fit points are necessary. Additionally, there is a condition placed on the number of  $dE/dx$  hits used to derive  $dE/dx$  values. The results presented here are within in rapidity  $|y| \leq 0.5$  and have same tracks cuts for all energy.

Figure 3.1.3: The example of tracks selection criteria for  $\sqrt{s_{NN}} = 39$  GeV Au+Au collisions.

## 3.2 Centrality Determination

In high energy heavy-ion collisions, the centrality of nucleus-nucleus collisions is an essential parameter. It can be defined using various parameters, with the most common being the collisional parameter  $b$ , which is the distance between the geometric center of the colliding nuclei in the cross-



section and their direction of motion. Other geometric parameters used include the number of participant ( $N_{part}$ ), and the number of nucleon-nucleon collisions,  $N_{coll}$ . The number of participants is defined as the number of nucleons, which undergo at least one inelastic nucleon-nucleon collision and the number of binary collisions is defined as number of inelastic nucleon-nucleon collisions. With this geometrical knowledge, we can compare the dependence of the observed quantities on the centrality in different experiments. However, these geometric quantities cannot be observed directly in the experiment and must be derived from a combination of observable measurements in the experiment and Monte Carlo simulations. The figure shown in Fig. 3.2.1 provides more clarity on the centrality parameter.

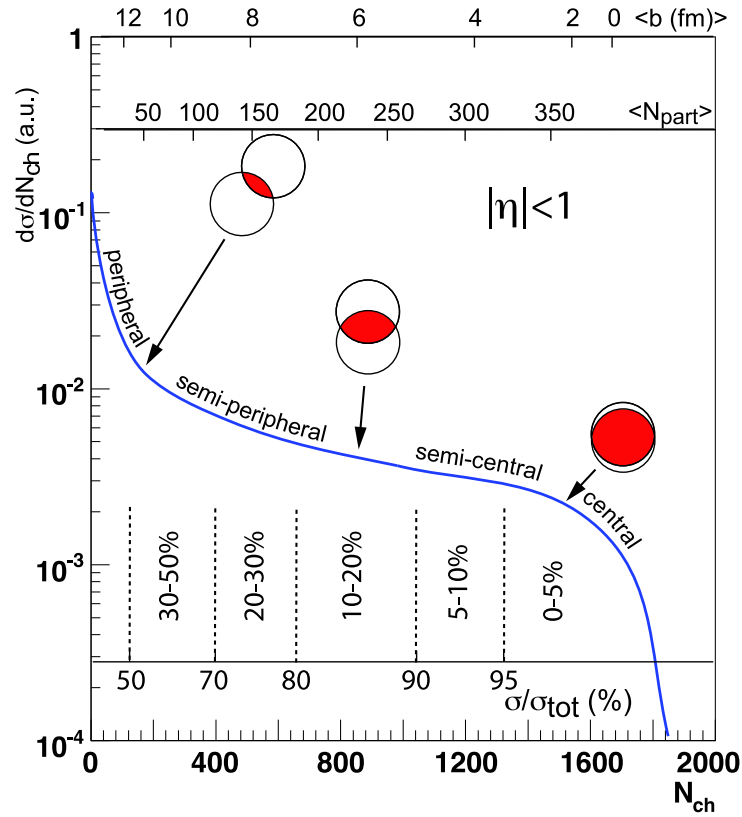


Figure 3.2.1: The cartoon example of the correlation of the final state observable  $N_{ch}$  with Glauber calculated quantities ( $b$ ,  $N_{part}$ ). Figure from [8].

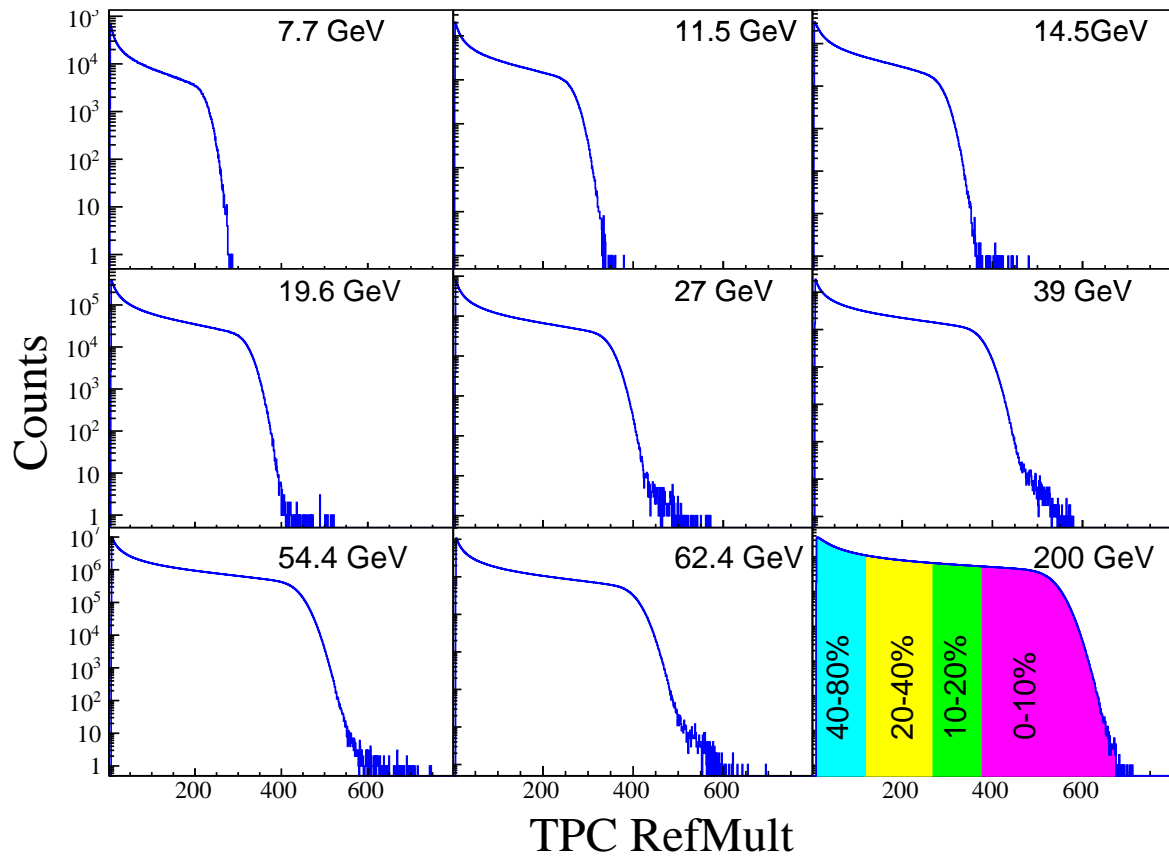


Figure 3.2.2: The distribution of TPC RefMult.



In the context of collisions between nucleons, the quantity of particles generated in the final state is in direct proportion to the centrality of the collision. When the nucleon-nucleon pair is at the center, more particles are produced, followed by semi-central collisions, and the least number of particles are produced in peripheral collisions. Additionally, the number of charged particles in the end state can reflect the initial geometric orientation of the collision. Therefore, the charged-particle distribution can be analyzed to determine the centrality of different collision events.

The centrality of Au+Au collision at  $\sqrt{s_{\text{NN}}} = 7.7\sim 200$  GeV cannot be directly defined through impact parameter in the experiment. Instead, it is defined by utilizing the uncorrected charged particle multiplicity  $dN/d\eta$  within  $|\eta| \leq 0.5$  (also known as reference multiplicity). To define centrality bins, a Monte Carlo Glauber calculation was used to compare with the  $dN/d\eta$  distribution of the data. Moreover, the efficiency and acceptance change on the measured  $dN/d\eta$  were addressed by considering the dependence on collision vertex  $z$ -position and luminosity. Figure 3.2.2 displays the uncorrected  $dN/d\eta$  distribution measured within vertex cuts for Au+Au collision  $\sqrt{s_{\text{NN}}} = 7.7\sim 200$  GeV. Further details can be found at <http://www.star.bnl.gov/protected/common/common2010/centrality/index.html>.

The centrality classes in this analysis were determined based on fractions of the reference multiplicity distribution. The events were divided into nine centrality classes, ranging from 0-5%, 5-10%, 10-20%, 20-30%, 30-40%, 40-50%, 50-60%, 60-70%, and 70-80%. However, for the purposes of our analysis with triton yields extracted, we combined some of these classes. Specifically, we combined the 0-10%, 10-20%, 20-40%, and 40-80% centrality classes.

### 3.3 Triton Identification

In the analysis presented, TPC and TOF detectors were utilized to identify tritons. The TPC  $dE/dx$  measurements were plotted as a function of rigidity ( $p/q$ ), and the resulting dashed curves show the Bichsel expectation values [62] in Fig. 3.3.1. It is evident that the TPC can identify various particles at low momentum, as indicated by the color bands; however, its resolution is reduced at higher transverse momentum, and TOF is necessary to identify these high momentum particles. The TOF measurements of  $m^2$  were also presented as a function of rigidity ( $p/q$ ) with tracks quality cuts, and the expectation values for proton, deuteron, and triton were shown as the dashed curves in Fig. 3.3.2. Interestingly, the plot of  $m^2$  distribution revealed an unexpected

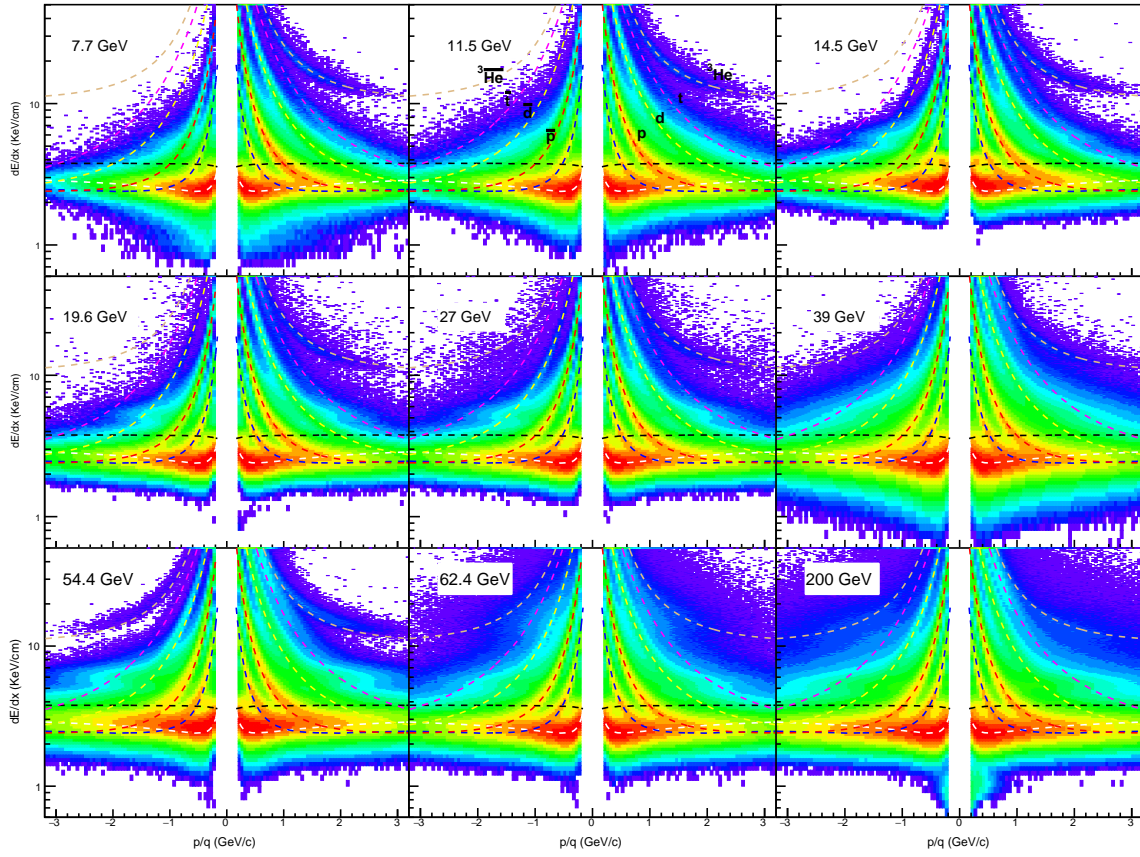


Figure 3.3.1: Energy loss  $dE/dx$  as a function of rigidity for Au+Au collisions at  $\sqrt{s_{NN}} = 7.7 \sim 200$  GeV. Dashed lines correspond to the theoretical predicted values for different nuclei. The black line represent electron, from low to up is  $\pi$ ,  $k$ , proton, deuteron, triton, and  ${}^3\text{He}$  respectively.

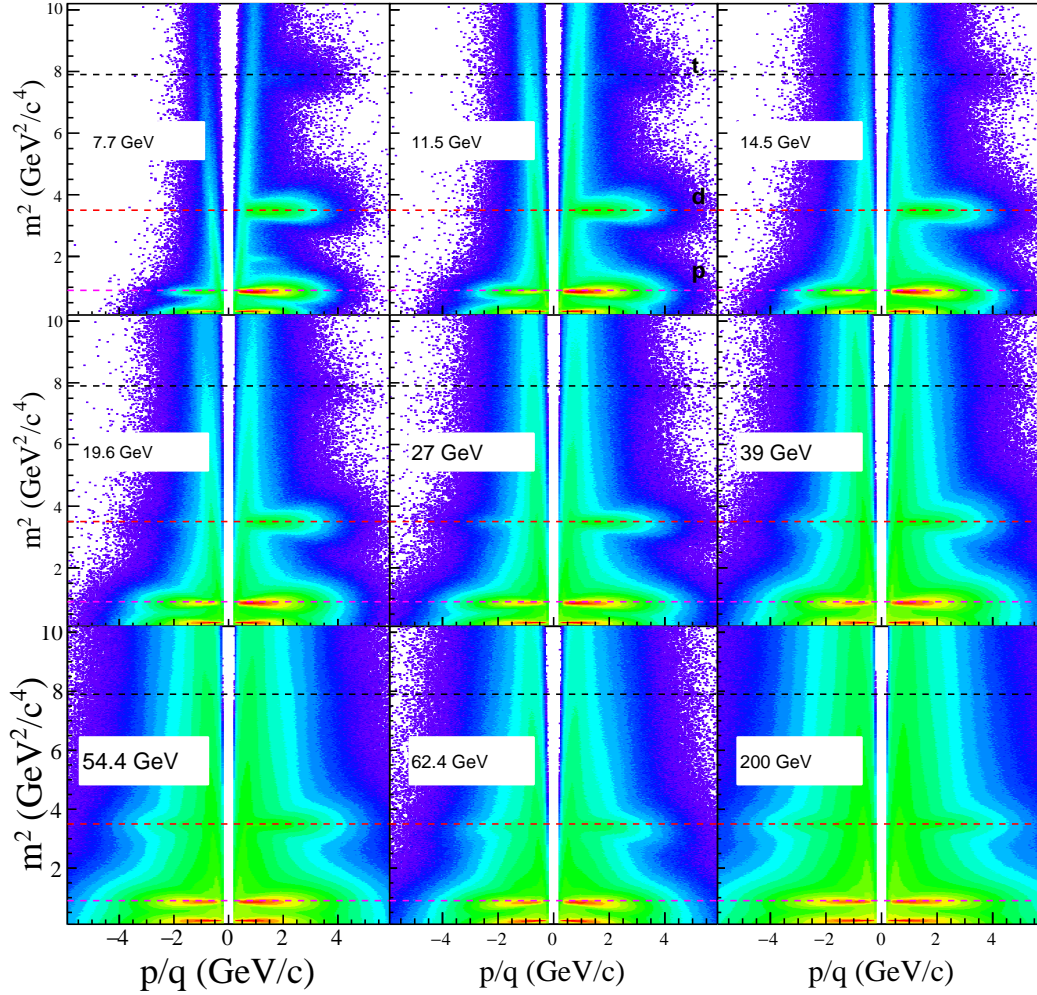


Figure 3.3.2:  $m^2$  as a function of rigidity for Au+Au collisions at  $\sqrt{s_{\text{NN}}} = 7.7\sim 200$  GeV. Dashed lines correspond to  $m^2$  for different nuclei.



vertical band from very low to high values, which could be attributed to particles exceeding the speed of light. Since it is impossible for any particle to travel faster than the speed of light, this unusual fraction of particles is likely to come from either end-state particles knock-out of the detector material or decay daughter particles of relatively long-lived but unstable particles that fly past the vertex detector. As none of the TOF detectors can record the time of flight starting of these particles, this could lead to the estimation of their velocities exceeding the speed of light with the same algorithm, thus presenting them as vertical bands on the  $m^2$  distribution.

Based on the measurement of the specific ionization energy deposited ( $dE/dx$ ) by charged particles in the TPC, a new variable  $z$  is defined to properly deconvolve these effects into a Gaussian. It is defined as

$$z_X = \ln \left( \frac{\langle dE/dx \rangle}{\langle dE/dx \rangle_X^B} \right). \quad (3.3.1)$$

where  $X$  is the particle type and  $\langle dE/dx \rangle_X^B$  is corresponding Bichsel function for each particle species as discussed in Eq. 2.2.1 [62, 3].

In high energy heavy-ion collisions, the rapidity  $y$  is often use to quantify the longitudinal momentum of particle motion, which means that the beam direction is consistent. In the experiments, the rapidity of a particle can be determined by the magnitude of the measured energy and longitudinal momentum, as shown below

$$y = \frac{1}{2} \ln \frac{E + p_z}{E - p_z} = \frac{1}{2} \ln \frac{1 + v_z}{1 - v_z} = \tanh^{-1}(v_z) \quad (3.3.2)$$

where  $v_z = p_z/E$  is the velocity along  $z$  direction. Rapidity is a measure of velocity but it stretches the region around  $v = c$  to avoid the relativistic scrunch, the two-dimensional plot of the transverse momentum ( $p_T$ ) and rapidity ( $y$ ) directly reflects the phase space distribution of the measured particles, and also show the acceptance performance of the detector. Fig. 3.3.3 shown the triton phase space for Au+Au collisions at  $\sqrt{s_{NN}} = 7.7 \sim 200$  GeV, the identification of triton is achieved through the combination of  $z_t$  from TPC with TOF's  $m^2$  cut.

Next, we will extract signals step by step from each centrality and transverse momentum interval, and quantitatively obtain the invariant mass spectrum of tritons. The main content is the separation of signal and background. The  $z_X$  distribution is constructed for a particular particle type within a given  $p_T$  bin at mid-rapidity. For the particle  $X$ , the most probable value of  $z_X$  is 0. Fig 3.3.4 shows the  $z_t$  distribution for triton in various  $p_T$  bins in Au+Au collisions at  $\sqrt{s_{NN}} = 39$  GeV, 0-10% centrality with  $|y| \leq 0.5$ . In order to extract the raw yields within a

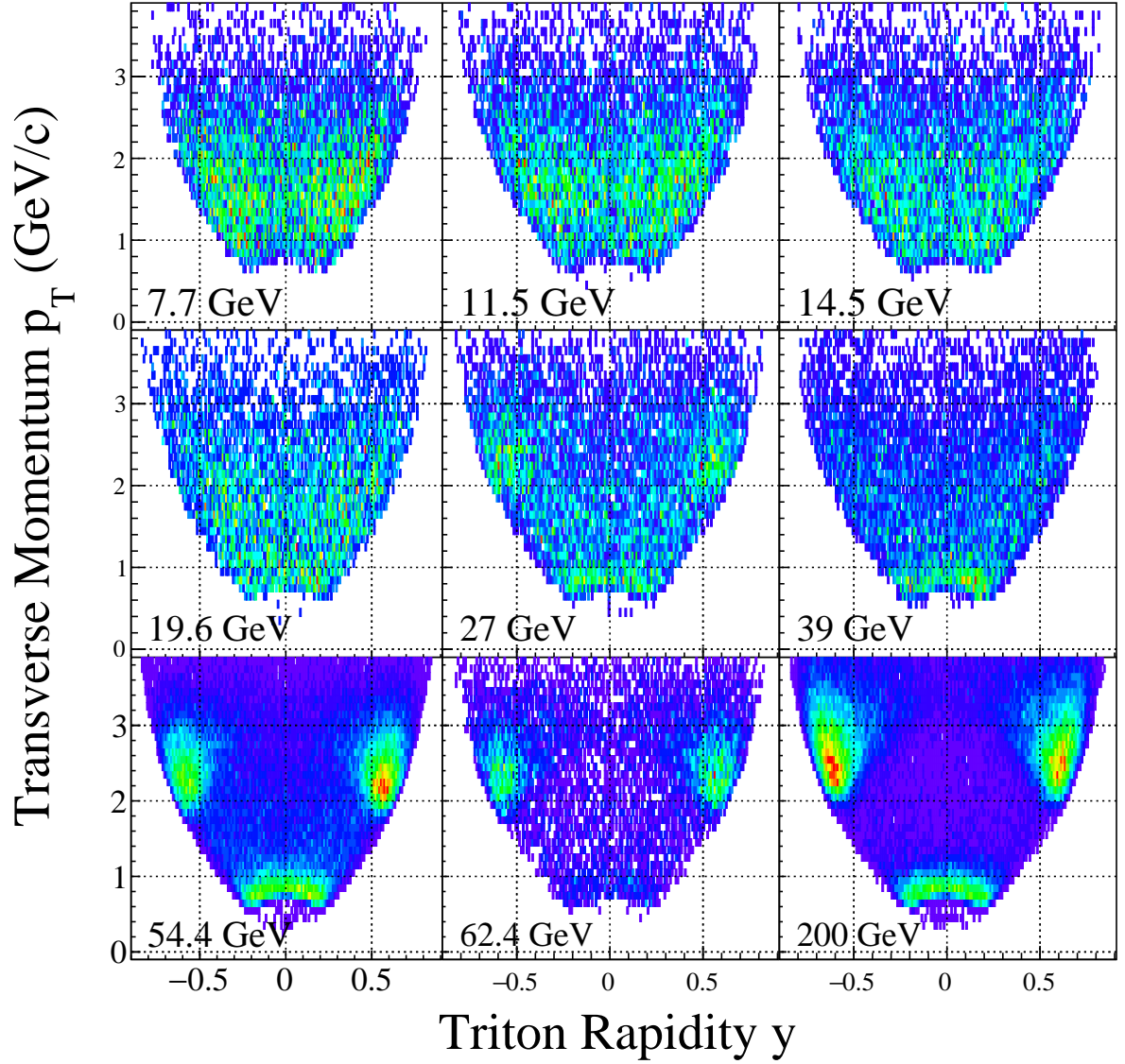


Figure 3.3.3: Triton phase space for Au+Au collisions at  $\sqrt{s_{NN}} = 7.7\sim 200$  GeV. For example, triton at 19.6 GeV is selected by a cutoff criterion of  $|z_t| < 0.2$  and  $6.9 \leq m^2 \leq 8.9$  ( $GeV^2/c^4$ ).

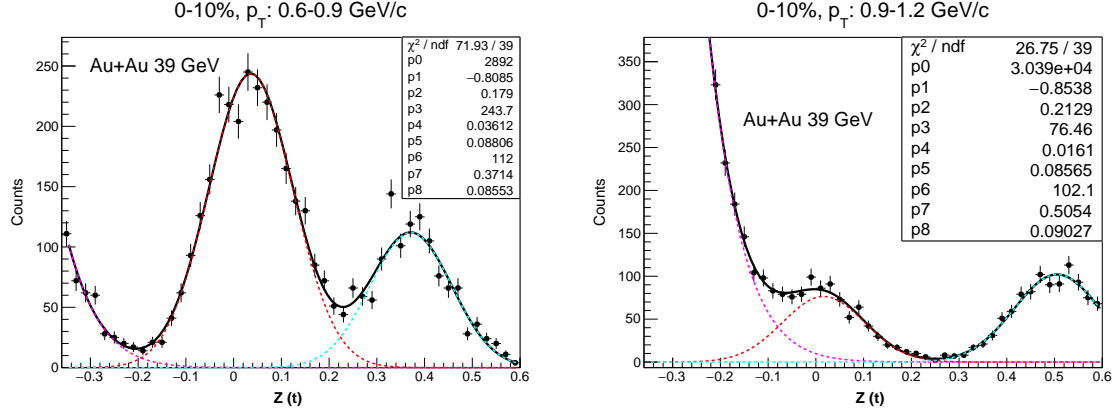


Figure 3.3.4: The  $z(t)$  distributions for triton from the TPC detector for different  $p_T$  bins and 0-10% centrality in Au+Au collisions at  $\sqrt{s_{\text{NN}}} = 39$  GeV. The curves are Gaussian fits. Errors are statistical only.

specific  $p_T$  bin, a three-Gaussian fit is utilized on the  $z_t$  distributions, as illustrated in Fig. 3.3.4. The region of the Gaussian function with a mean value of 0 is that corresponds to the particle of interest provides the yield for that particle within the given  $p_T$  bin. At low  $p_T$ , the peaks of the triton, deuteron, and proton distributions are clearly differentiated. However, to distinguish most of the triton from the beam pipe at low  $p_T$ , we rely on the DCA distribution. In our analysis, we exclude the  $0.3 < p_T < 1.2$  GeV/c region, although we will discuss this further in detail later.

When  $p_T \geq 1.2$  GeV, it becomes difficult to distinguish triton from other particles based on the energy loss  $dE/dx$  alone. Therefore, both the TPC and TOF were used to identify triton. Initially, a cut of  $|z| \leq 0.3$  was applied to remove most of the contamination from the triton raw signals. Then, to extract the raw triton yields, the mass squared distribution obtained from the TOF detector was used, which is defined as Eq. 2.2.2. The  $m^2$  distribution was fitted with a superposition of a Gaussian function and an exponential tail to distinguish the triton signal from the background, respectively.

To extract the triton signal from the  $m^2$  distribution, there are primarily three cases. Firstly, for low collision energies ( $\sqrt{s_{\text{NN}}} < 39$  GeV) and relatively small intervals of transverse momentum or peripheral collisions, the background contamination is negligible for the triton signal. In these scenarios, the distribution of the signal can be directly fitted with a Gaussian function, and the raw counts can be obtained by the integral function. It is also important to verify that the signal

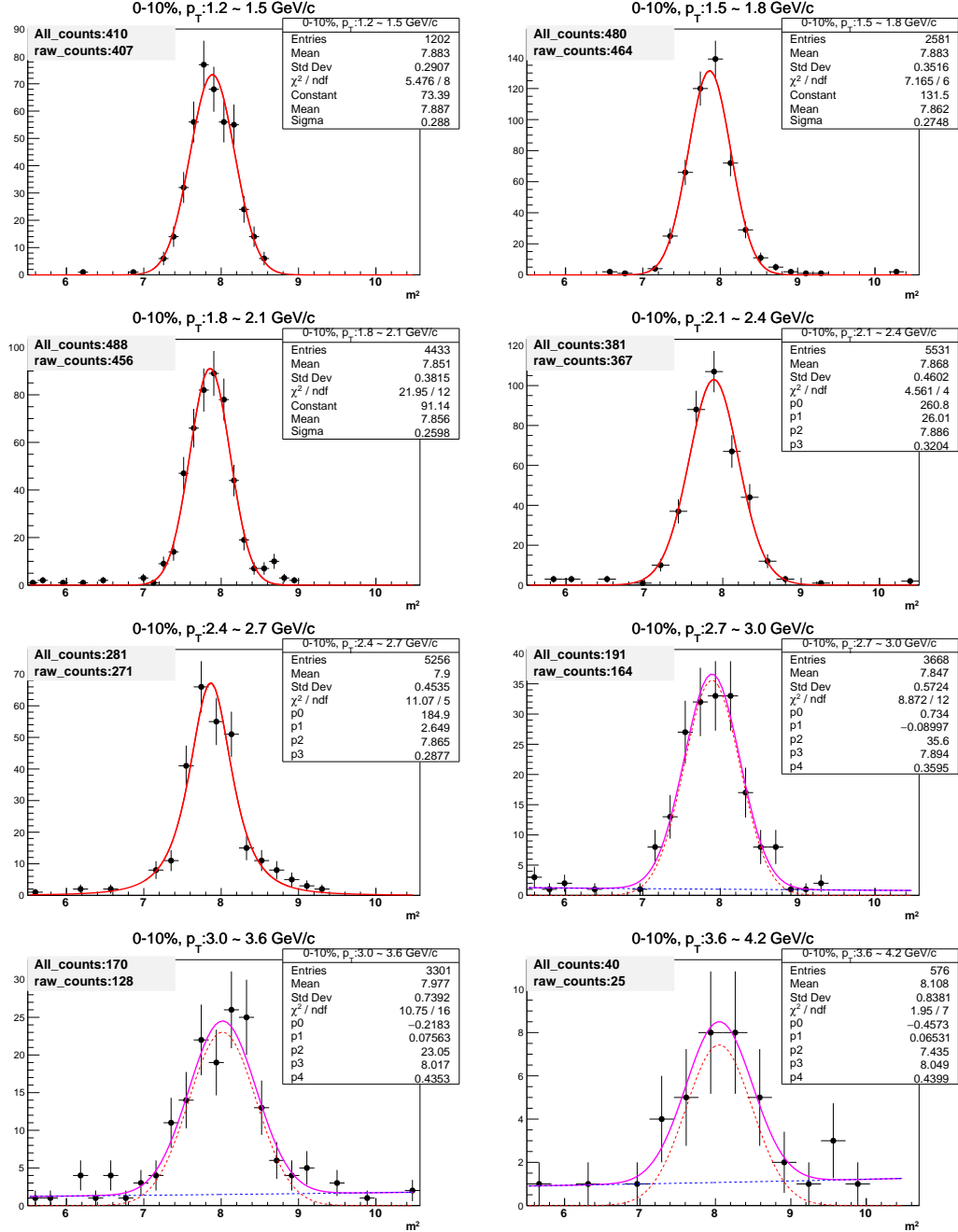


Figure 3.3.5: The  $m^2$  distributions for triton in the TOF in Au+Au collisions at  $\sqrt{s_{NN}} = 7.7$  GeV, 0-10%. The curves are Gaussian and exponential function fits. Errors are statistical only.

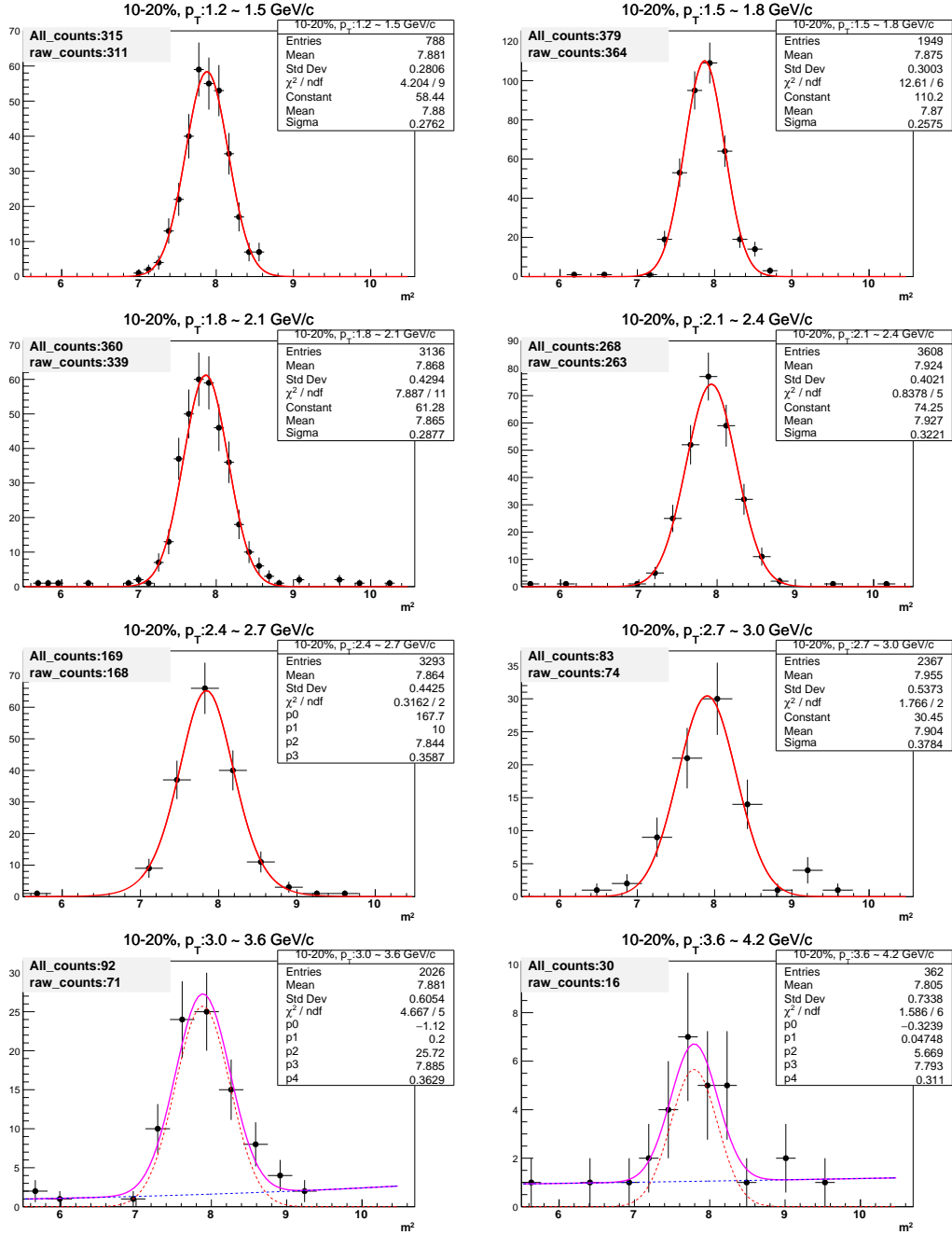


Figure 3.3.6: The  $m^2$  distributions for triton in the TOF in Au+Au collisions at  $\sqrt{s_{NN}} = 7.7$  GeV, 10-20%. The curves are Gaussian and exponential function fits. Errors are statistical only.

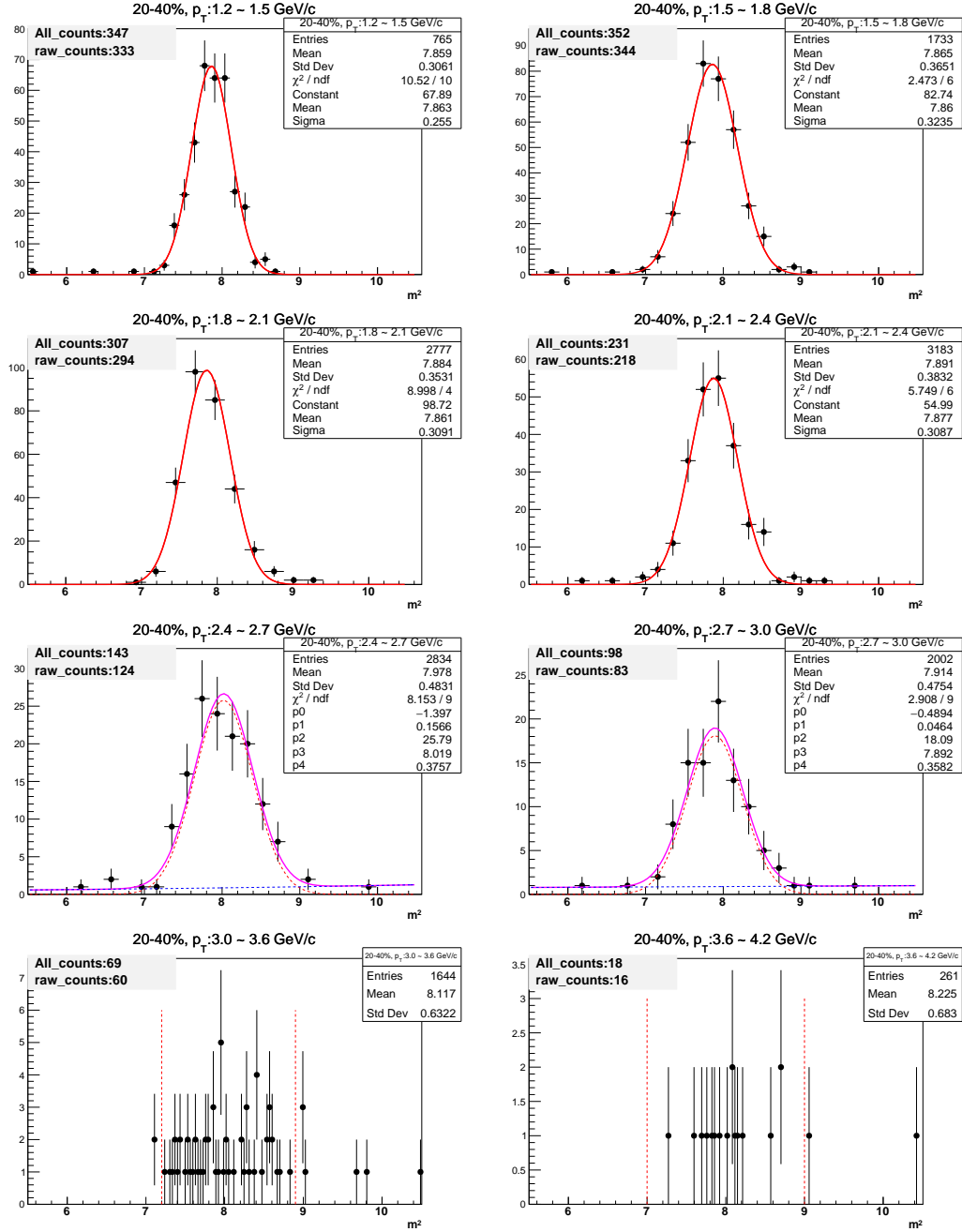


Figure 3.3.7: The  $m^2$  distributions for triton in the TOF in Au+Au collisions at  $\sqrt{s_{NN}} = 7.7$  GeV, 20-40%. The curves are Gaussian and exponential function fits. Errors are statistical only.

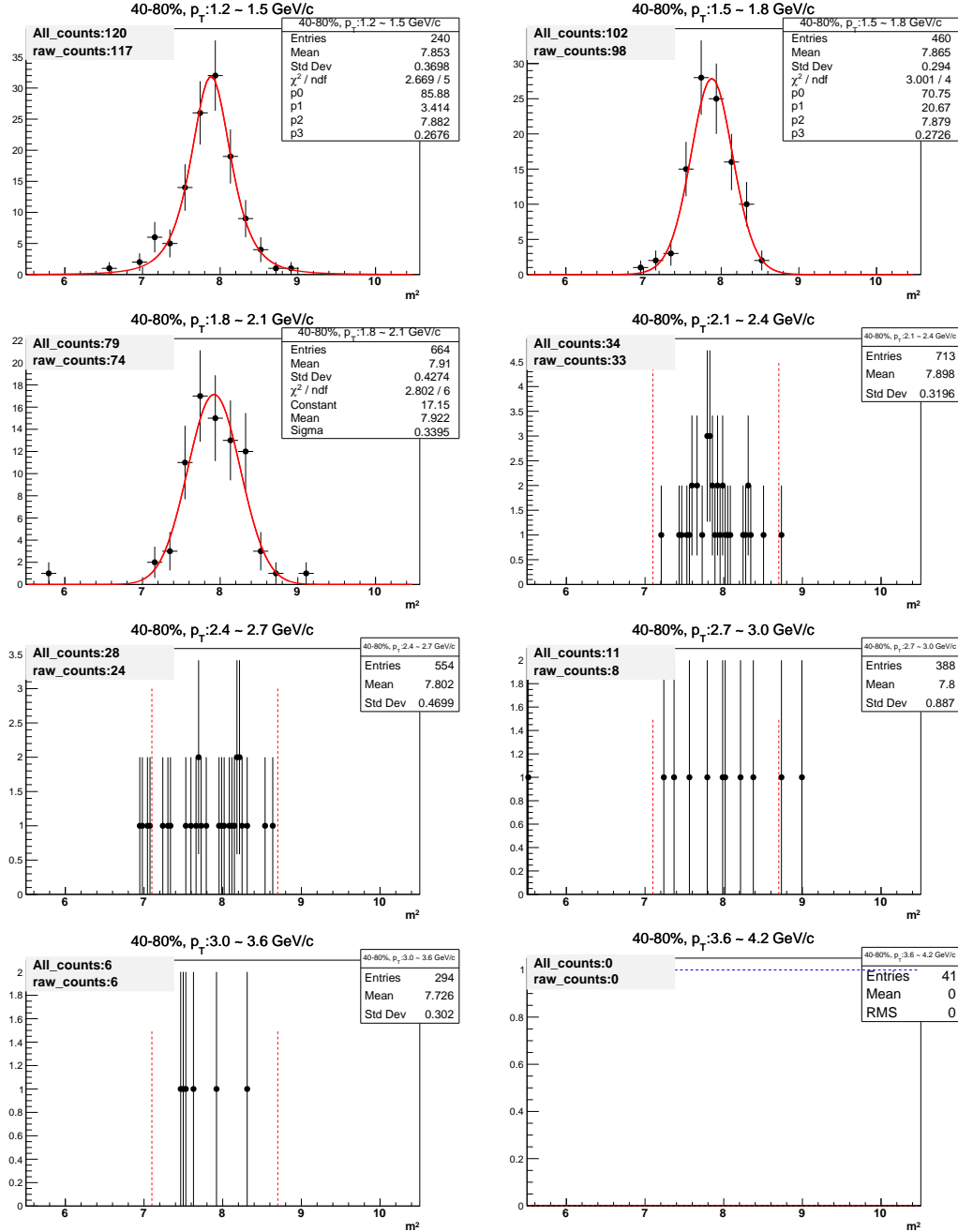


Figure 3.3.8: The  $m^2$  distributions for triton in the TOF in Au+Au collisions at  $\sqrt{s_{NN}} = 7.7$  GeV, 40-80%. The curves are Gaussian and exponential function fits. Errors are statistical only.

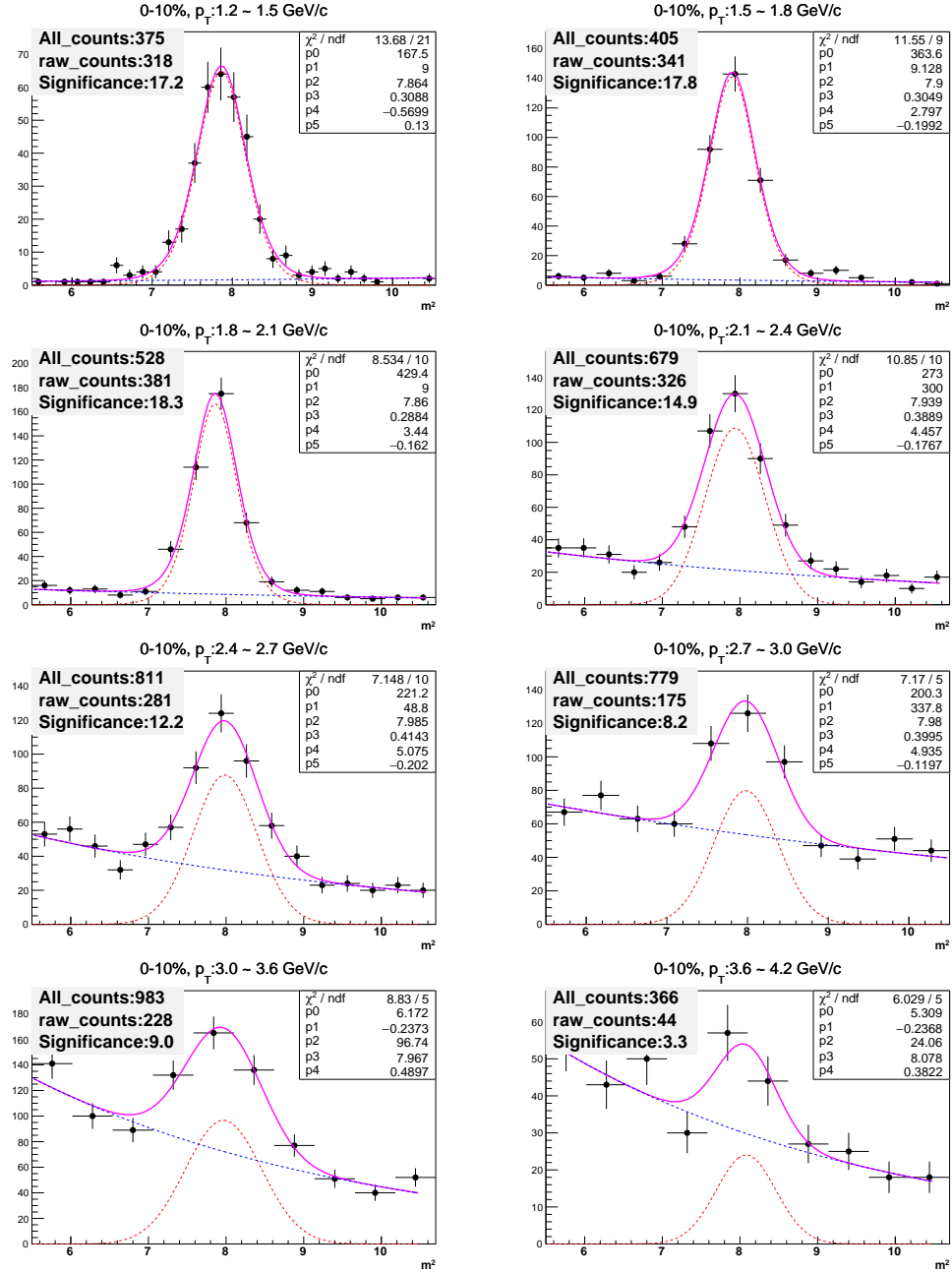


Figure 3.3.9: The  $m^2$  distributions for triton in the TOF for different  $p_T$  bins in Au+Au collisions at  $\sqrt{s_{NN}} = 39$  GeV, 0-10%. The curves are Gaussian and exponential function fits. Statistical error only.

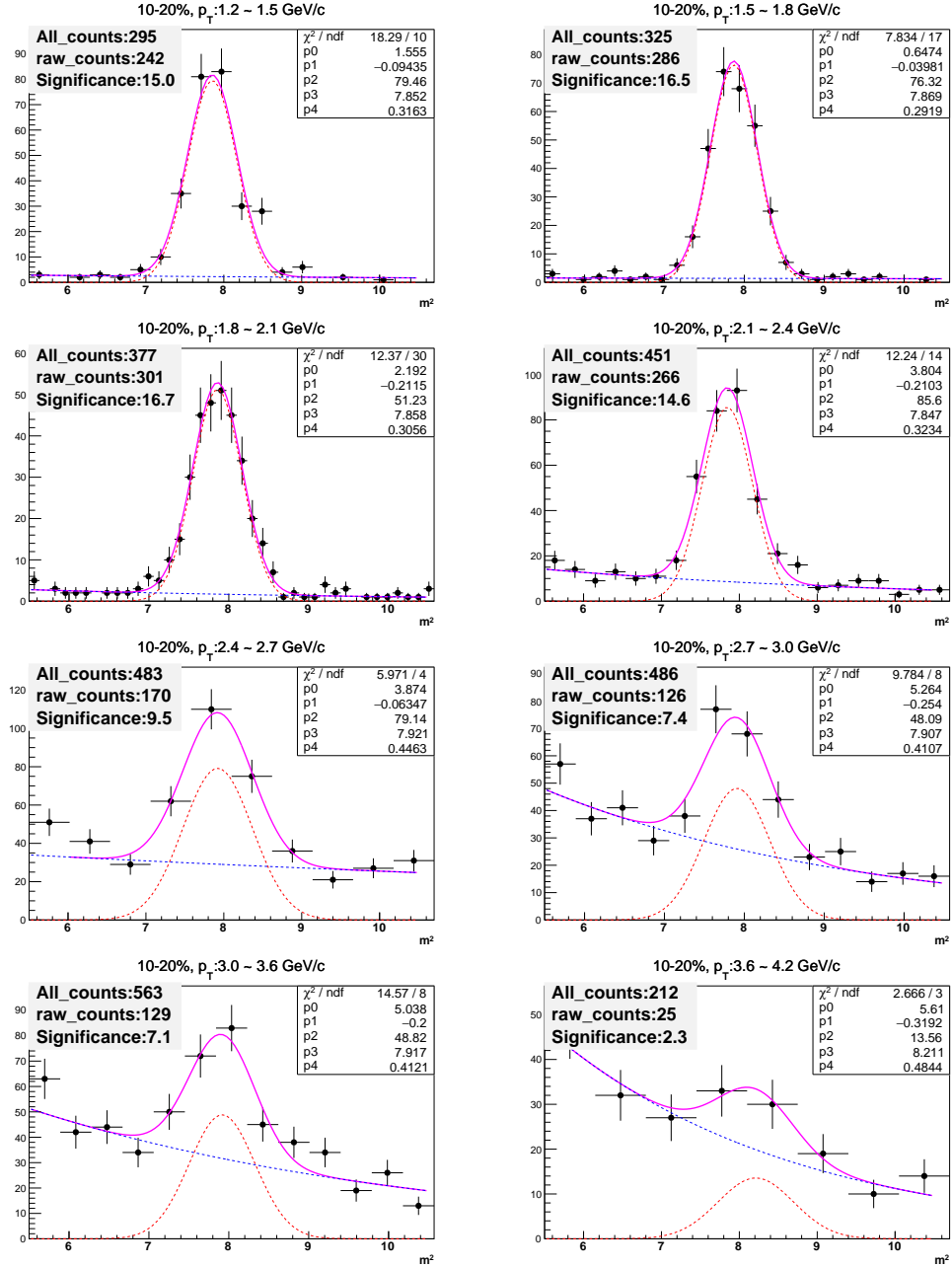


Figure 3.3.10: The  $m^2$  distributions for triton in the TOF for different  $p_T$  bins in Au+Au collisions at  $\sqrt{s_{NN}} = 39$  GeV, 10-20%. The curves are Gaussian and exponential function fits. Statistical error only.

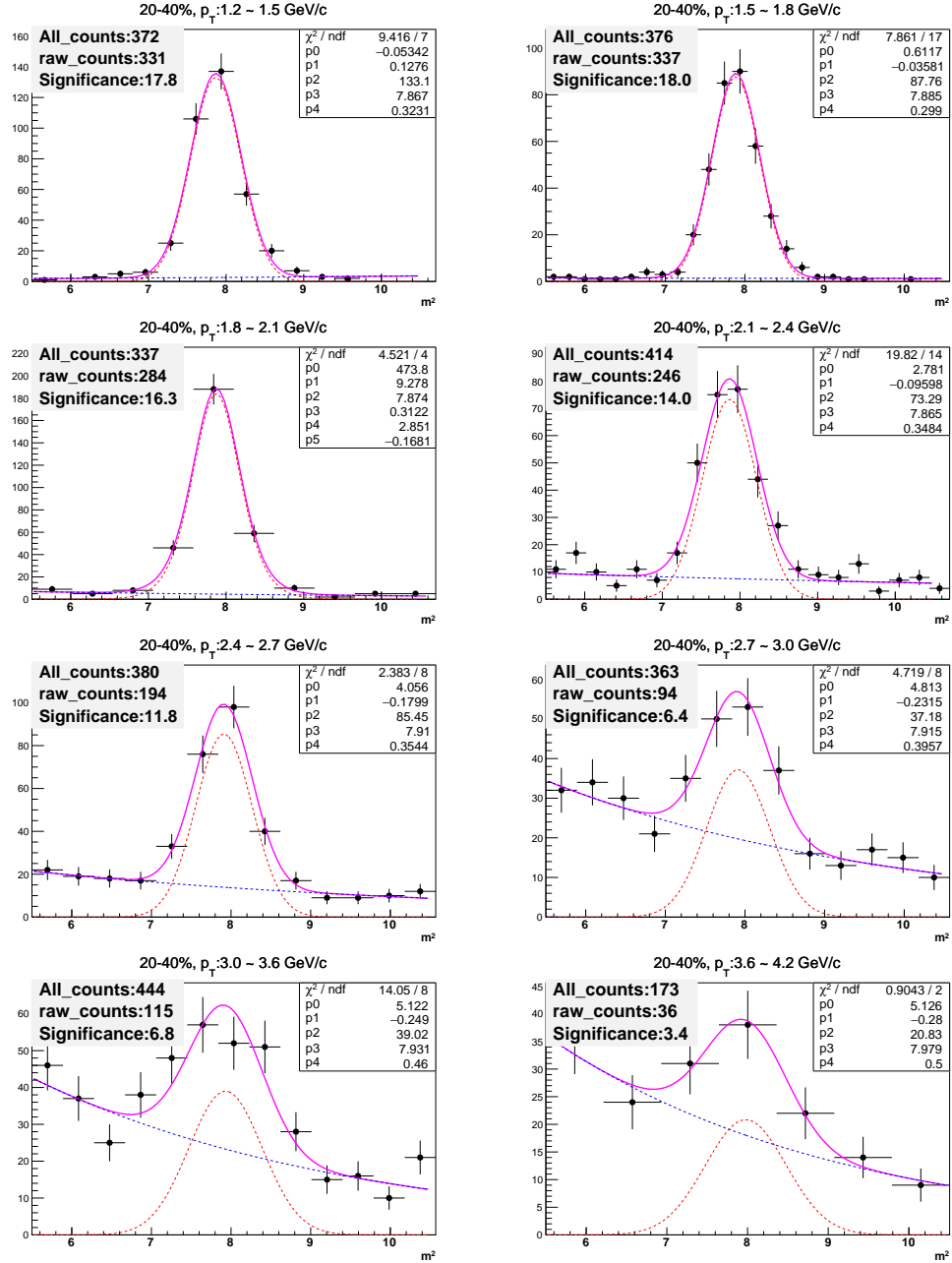


Figure 3.3.11: The  $m^2$  distributions for triton in the TOF for different  $p_T$  bins in Au+Au collisions at  $\sqrt{s_{NN}} = 39$  GeV, 20-40%. The curves are Gaussian and exponential function fits. Statistical error only.

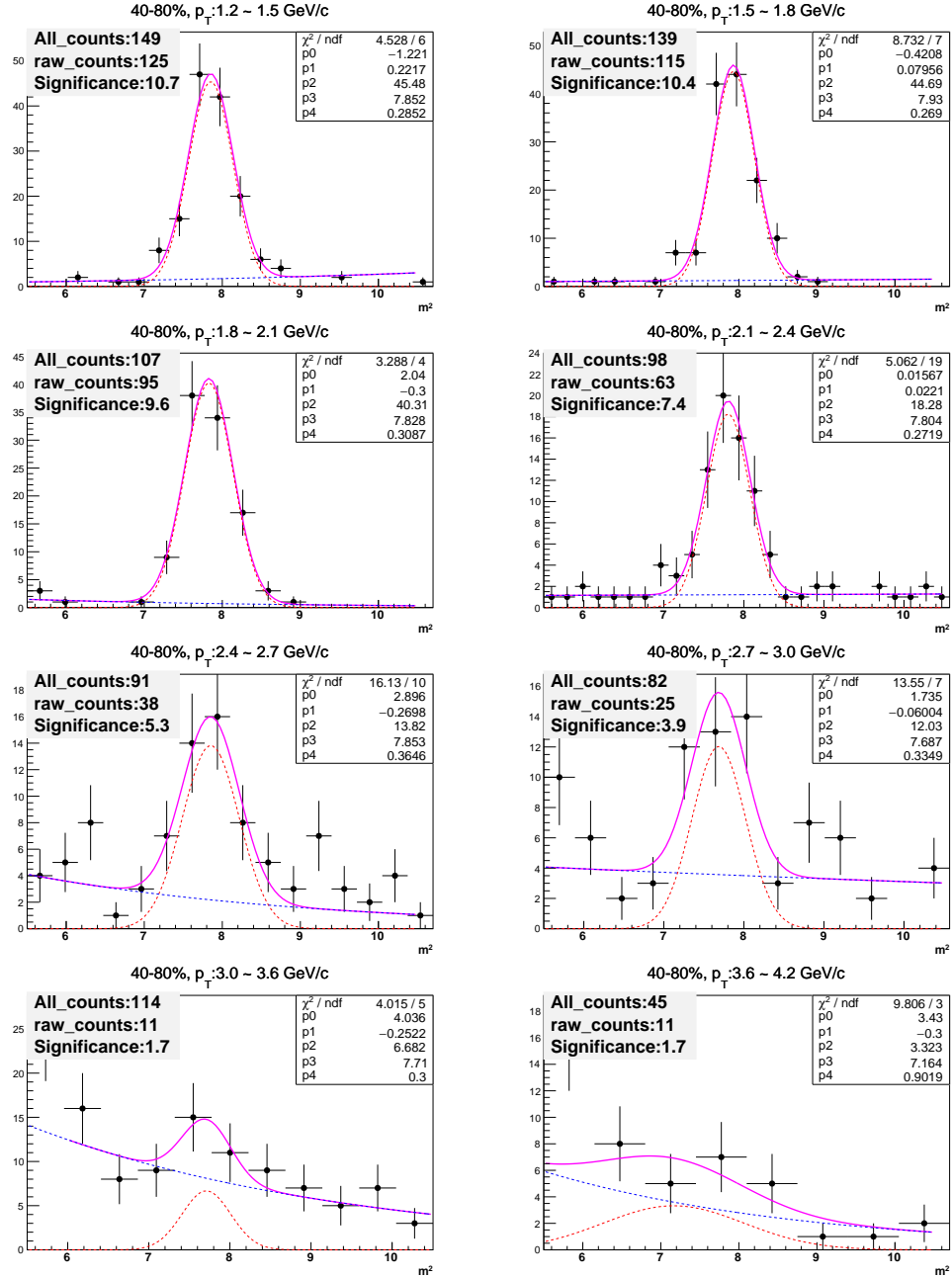


Figure 3.3.12: The  $m^2$  distributions for triton in the TOF for different  $p_T$  bins in Au+Au collisions at  $\sqrt{s_{NN}} = 39$  GeV, 40-80%. The curves are Gaussian and exponential function fits. Statistical error only.



counts are consistent with the results obtained by counting bin by bin for the  $p_T$  intervals without background contamination. Secondly, as the  $p_T$  increases, the resolution of the TPC deteriorates, resulting in more background after the  $z_t$  cut. In such cases, background reduction techniques must be employed to extract the triton signal. The Gaussian+Exponential function is defined to fit the total  $m^2$  distribution, with initial parameters derived from the fitting of the signal at  $6.9 \leq m^2 \leq 8.9$  ( $GeV^2/c^4$ ) and background intervals of  $m^2 \leq 6.9$   $GeV^2/c^4$  or  $m^2 \geq 9.0$   $GeV^2/c^4$ . The Gaussian function parameters obtained from this step are used to select the triton candidates. Lastly, for the  $p_T$  range where there is a limitation in statistics, only the number of signals in the signal interval can be counted. However, this is only applicable to low collision energies.

Fig. 3.3.5 - Fig. 3.3.12 illustrate the distribution of  $m^2$  for triton at different  $p_T$  bins and collision centralities in Au+Au 7.7 GeV and 39 GeV respectively. To extract the triton signal, we have applied the methods mentioned above. The solid red line and magenta dashed line represent signal, while the blue dashed line represents background in all plots. after careful analysis, it was found that the statistical of data are not sufficient enough for extracting the triton signal, so we set different bin widths for different  $p_T$  ranges of  $m^2$  distribution in order to mitigate the fluctuations in the triton spectra, which will contribute to the systematic uncertainty of triton yield. The  $m^2$  distribution for other energy can be found in the STAR triton note [63].

## 3.4 Data Correction

### 3.4.1 TPC Tracking Efficiency

The detector acceptance and efficiency of reconstructing particle tracks are determined by embedding together. The simulated triton is generated and pass through GSTAR as discussed in section 2.3. The ratio of the distribution for reconstructed and original Monte Carlo tracks gives the TPC tracking efficiency (efficiency  $\times$  acceptance  $\varepsilon_{\text{TPC}}$ ) correction as a function of  $p_T$ . The typical TPC tracking efficiency for triton in different collision centralities at mid-rapidity ( $|y| < 0.5$ ) in Au+Au 39 GeV is shown in Fig. 3.4.1. TPC tracking efficiency does not have a strong energy dependence, and for other energy can be found in Ref. [63].

The TPC tracking efficiency is fitted by the function 3.4.1, which has been used in our raw yield correction.

$$\varepsilon_{\text{TPC}}(p_T) = a \exp - \left( \frac{b}{p_T} \right)^c + d \exp \frac{-\frac{1}{2}(p_T - e)^2}{f} \quad (3.4.1)$$

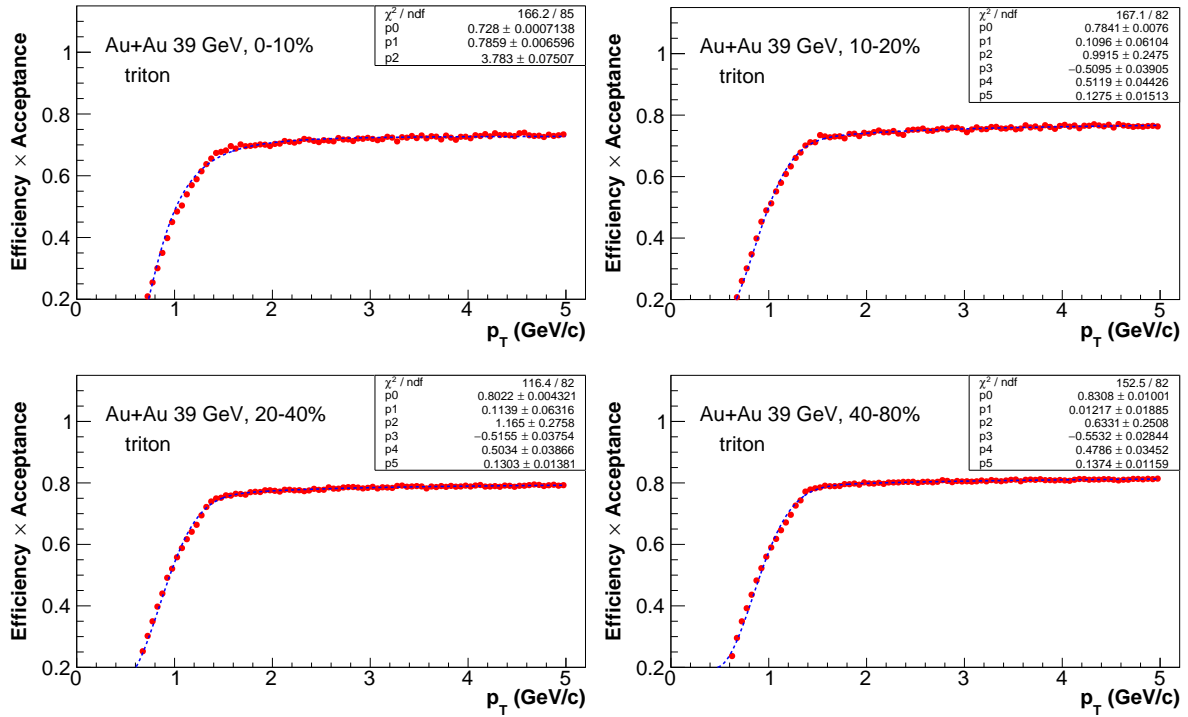


Figure 3.4.1: Efficiency  $\times$  acceptance for reconstructed triton at  $\sqrt{s_{NN}} = 39$  GeV in the TPC as a function of  $p_T$  at mid-rapidity ( $|y| < 0.5$ ) in Au+Au collisions. The lines are fitting by the function shown in the text.

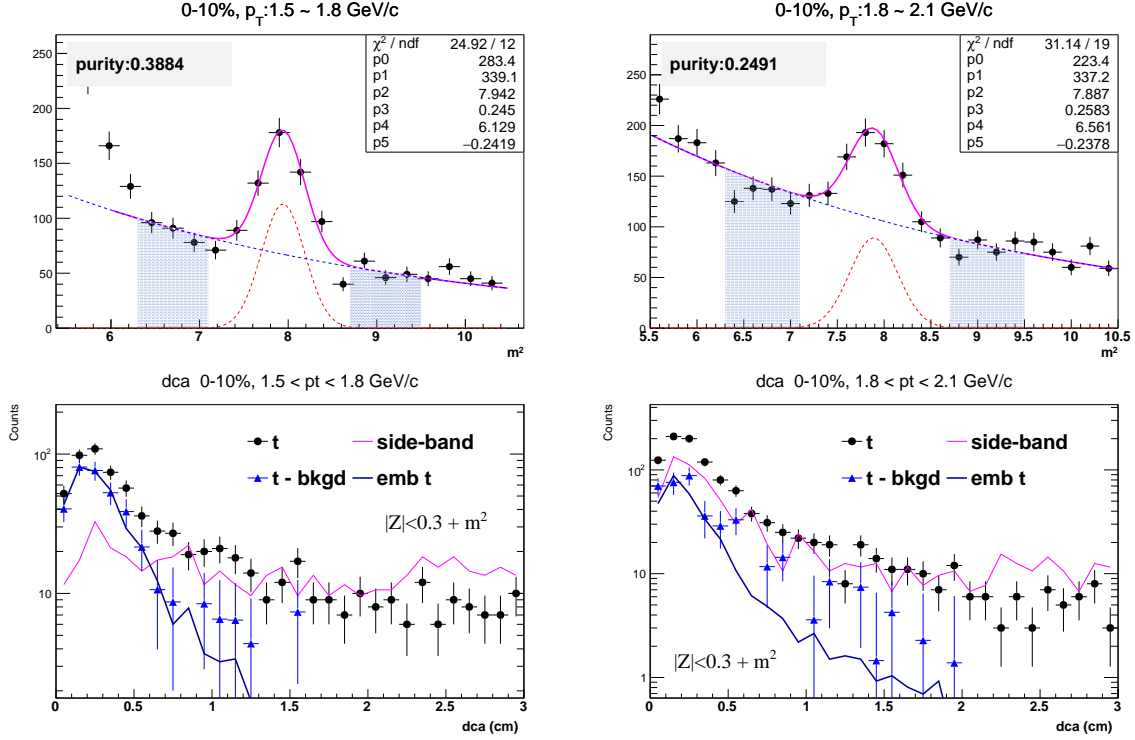


Figure 3.4.2: First row: Triton signal extraction from 200 GeV, the region of side-band is  $m^2 \in [6.3, 7.1] \& [8.7, 9.5] \text{ GeV}^2/c^4$ , the signal region is  $7.1 < m^2 < 8.7 \text{ GeV}^2/c^4$ . Second row: normalized side-band  $\times$  background counts.

When using embedding data, it is crucial to ensure that the embedding data can be matched to the real data. To verify this, a further check was performed and the results are depicted in Fig. 3.4.2. The top row of each panel exhibits the  $m^2$  distribution at varying  $p_T$  bins. Since the triton mass square is approximately  $7.9 \text{ GeV}^2/c^4$ , the signal region in the  $m^2$  distribution was selected to be  $7.1 - 8.7 \text{ GeV}^2/c^4$ , whereas the background region from the side-band is defined as  $m^2 \in [6.3, 7.1] \& [8.7, 9.5] \text{ GeV}^2/c^4$ . In the signal region, the triton signal and background are included as two components. However, it is not possible to count the background from the signal region. To compare the DCA distribution with the embedding DCA distribution of triton, it was assumed that the background from the signal region is the same as the side-band background. The second row of Fig. 3.4.2 shows the normalized side-band DCA distribution, which was used to scale the total counts in the side-band from the  $m^2$  distribution. The magenta solid line represents the

side-band distribution. The signal region DCA distribution was then subtracted from the magenta line, and the resulting triton DCA distribution is represented by the blue triangle. The consistency between the DCA distribution from the embedding data can be observed.

### 3.4.2 TOF Matching Efficiency

The TPC and the TOF are separate detectors. While the TPC identifies low- $p_T$  ( $\leq 1.2$  GeV/c) particles well, the TOF gives better particle identification than the TPC at higher momentum. However, not all TPC tracks give a hit in the TOF, so there is an extra correction called TOF matching efficiency correction needed for the spectra obtained using the TOF detector. This is done with a data-driven technique. The matching efficiency from TPC to TOF ( $\varepsilon_{\text{TOF}}$ ) is studied via comparing the number of the tracks which match TOF and the total number of TPC primary tracks from real data and the definition is shown in Eq. 3.4.2. The tracks selection is the necessary tracks quality cuts and  $|z_t| < 0.3$  for triton the same as what we used in  $m^2$  fitting. Typical TOF matching efficiency for triton in different collision centralities at mid-rapidity ( $|y| < 0.5$ ) in Au+Au 39 GeV is shown in Fig. 3.4.3. TOF matching efficiency does not have a strong energy dependence, and for other energy can be found in Ref. [63]. TOF matching efficiency is fitted by the function of 3.4.3.

$$\varepsilon_{\text{TOF}}(p_T) = \frac{\text{the number of TOF Matched Tracks}}{\text{the number of TPC Tracks}} \quad (3.4.2)$$

$$\varepsilon_{\text{TOF}}(p_T) = a \exp\left(-\frac{b}{p_T}\right)^c \quad (3.4.3)$$

The TOF system consists of 60 trays, each containing several MRPC modules. Each module is further divided into 6 readout pads. TOF's primary algorithm for track recording involves matching the points measured on the TOF with the TPC (global) tracks. If multiple tracks in the TPC appear in one pad of the TOF simultaneously, they are not recorded as tracks measured by the TOF. When a track corresponds to several hit points in the TOF, the closest hit point is selected. During the TOF track reading process, every track contains various pieces of information. As following

- **mMatchFlag**: 0 - no matching; 1 - one to one matching; 2 - one to two matching, but the one with higher TOT picked; 3 - one to two matching, but the one with smaller  $|y_{\text{Local}}|$  got picked.

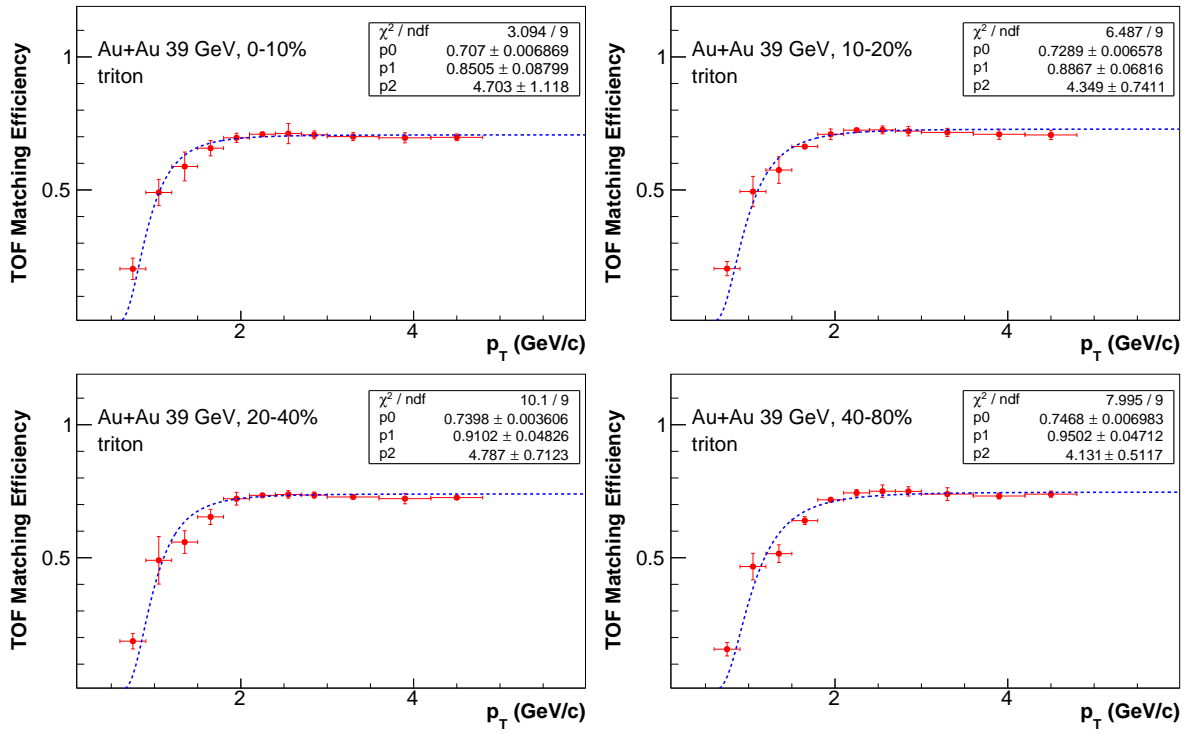


Figure 3.4.3: TOF matching efficiency for triton as a function of  $p_T$  at mid-rapidity ( $|y| < 0.5$ ) in Au+Au collisions at 39 GeV. The lines are fitting by the function shown in Eq. 3.4.3.

- **mYLocal/mZLocal/mThetaLocal**: hit local position/incident angle.
- **mPosition**: track projected point position in the STAR global coordinates.
- **mTimeOfFlight**: time of flight for matched TOF hit (with respect to the primary vertex).
- **mPathLength**: track path length from primary vertex to TOF.
- ... ..

In high energy central collisions where the track density is high and detector resolution is not optimal, it may be necessary to use **mYLocal/mZLocal/mThetaLocal** cut information to reduce background noise and improve signal detection. However, it is important to note that implementing these track cuts may affect the efficiency of TOF matching, and careful consideration must be given to track cut conditions in the analysis.

### 3.4.3 Energy Loss Correction

The particle will lose energy while traversing the detector material. The energy loss for TPC tracks was studied by embedding the sample with the full detector simulation. Figure 3.4.4 shows the difference between reconstructed triton  $p_T^{\text{rec}}$  and input  $p_T^{\text{MC}}$  from embedding sample for Au+Au 39 GeV collisions. The distribution was parametrized by the function defined in Eq. 3.4.4, where parameter  $A$  approaches zero at high  $p_T$ . It is shown in Fig. 3.4.4.

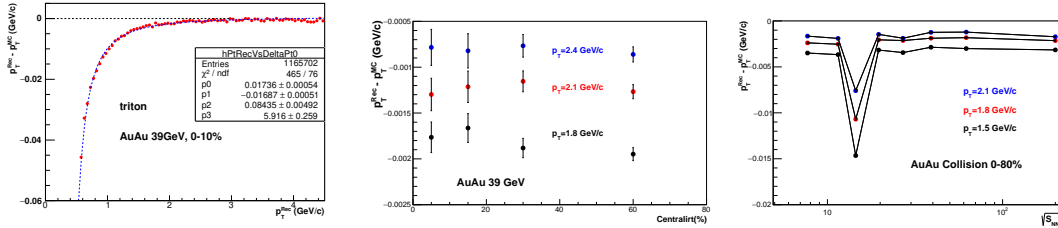


Figure 3.4.4: Left: The  $p_T$  difference of reconstructed and embedded triton as a function of  $p_T^{\text{rec}}$  in Au+Au collision at 39 GeV, 0-10% centrality. Middle: The energy loss of the triton as a function of collision centrality. Right: The energy loss of the triton as a function of collision energy.

$$f(p_T) = A + B \left( 1 + \frac{C}{p_T^2} \right)^D \quad (3.4.4)$$



It was found that the energy loss for a given  $p_T$  range is collision centrality independent, and collision energy independent, except 14.5 GeV because at Run14 the HFT detectors [64] were installed. The middle and right side of the Fig. 3.4.4 shows the centrality and energy dependence of energy loss correction for these  $p_T$  bins.

### 3.4.4 Absorption Correction

In the embedding simulation, the GEANT3 was used to extract the reconstruction efficiency. There are no cross-sections available for light (anti-)nuclei, GEANT3 basically treats light (anti-)nuclei as generic hadrons ( $p$  and  $\bar{p}$ ). So, embedding efficiencies of light (anti-)nuclei are too high. Every STAR publication so far, all on (anti-)nuclei, typically treats this deficiency with an additional ‘‘Absorption correction’’. These corrections were studied using GEANT4, which has extensively validated cross-sections for light (anti-)nuclei based on experimental data. The detail can be found at [http://www.star.bnl.gov/protected/lfsupc/yuning/BES/pwg/bill\\_llope\\_20130524.pdf](http://www.star.bnl.gov/protected/lfsupc/yuning/BES/pwg/bill_llope_20130524.pdf) by Bill Llope. We used the absorption correction function for triton by a polynomial of degree eight as below,

$$f(t) = p_0 + p_1 p_T + p_2 p_T^2 + p_3 p_T^3 + p_4 p_T^4 + p_5 p_T^5 + p_6 p_T^6 + p_7 p_T^7 + p_8 p_T^8 \quad (3.4.5)$$

The parameter are shown in the Table. 3.3

Table 3.3: Parameters for absorption correction

	$p_0$	$p_1$	$p_2$	$p_3$	$p_4$
$t$	1.19534	-0.276449	0.172299	-0.0578214	0.0118125
	$p_5$	$p_6$	$p_7$	$p_8$	
$t$	-0.00152635	0.000122568	-5.60466e-06	1.11765e-07	

### 3.4.5 Triton Background Estimation

Same with other particles, the triton sample contains background triton knocked out from the beam pipe and the detector materials [65]. Most of these triton have large DCA (*the distance of closest approach*) and are not reconstructed as primary particles. However, some of these background tritons have small DCA and are therefore included in the primary track sample, and a

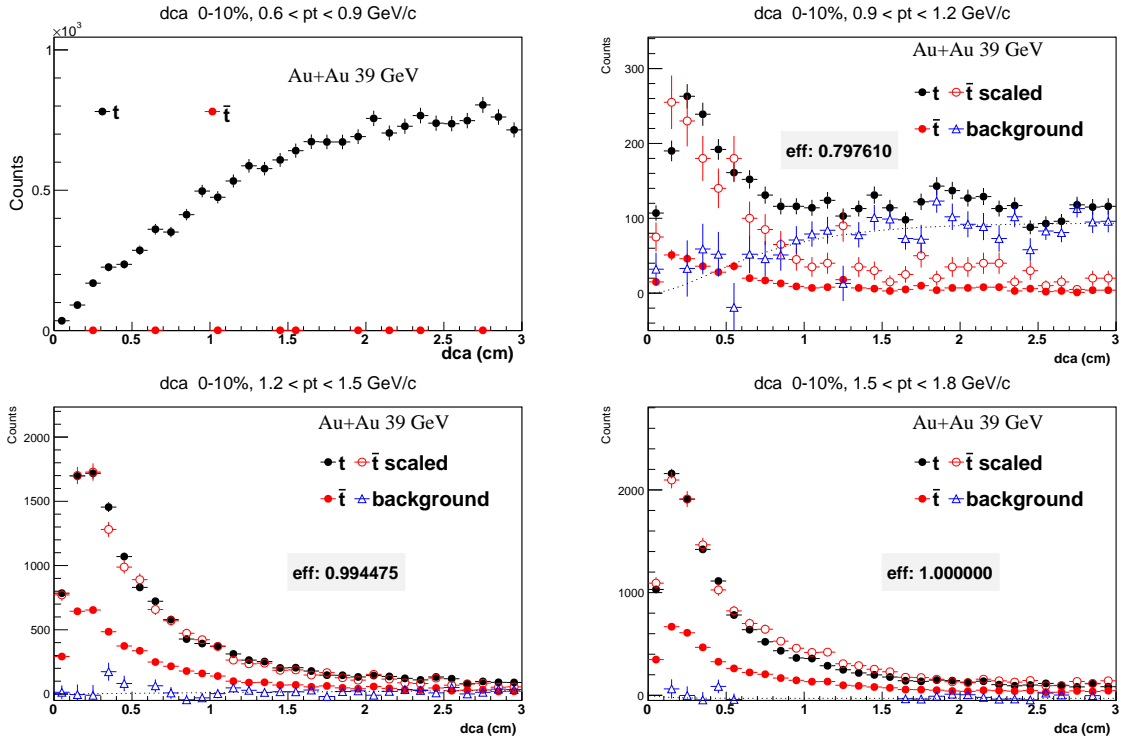


Figure 3.4.5: DCA distributions of triton for  $0.60 < p_T < 0.9 \text{ GeV}/c$ ,  $0.9 < p_T < 1.2 \text{ GeV}/c$  and  $1.2 < p_T < 1.5 \text{ GeV}/c$  up to  $3.9 \text{ GeV}/c$  in  $39 \text{ GeV Au+Au}$  collisions. Errors shown are statistical only. The dashed curve is the fit triton background. The red circles are the scaled  $\bar{t}$  distribution.



correction is needed [66]. Fig. 3.4.5 shows the DCA distribution of triton for selected by a  $dE/dx$  cut of  $|z_t| < 0.2$  in 39 GeV Au + Au collisions, where  $z_t$  is given by Eq. 3.3.1. We take the triton DCA distribution from 39 GeV at 0-10% centrality to explain the low  $p_T$  ( $p_T < 1.2$  GeV/ $c$ ) signal we cannot extracted due to the large background contamination. For  $0.6 < p_T < 0.9$  GeV/ $c$ , the triton counts increase with DCA increasing, that mean the knock-out triton dominated at this  $p_T$  region. The anti-triton almost zero. For  $0.9 < p_T < 1.2$  GeV/ $c$  we can see the DCA distribution with long nearly flat tail, which also the knock-out triton contribution. The anti-triton has rarely statistic. When the  $p_T > 1.2$  GeV/ $c$ , the tail become significantly diminished. The anti-triton is increase with  $p_T$  increasing. Brief summary, the long nearly flat DCA tail in the triton distribution comes mainly from knock-out triton. The effect is obviously at low  $p_T$  and significantly diminished at high  $p_T$ . Anti-triton have no knock-out background, the flat DCA tail is absent from their DCA distribution. The triton background fraction decreases with increasing  $p_T$  and decreasing energy which can be seen from Fig 3.4.5 with the cut DCA  $< 1$  cm. Because of the insufficient statistics, the DCA distribution of the anti-triton cannot be obtained, and we have to abandon the signal extraction in the low pt interval ( $p_T < 1.2$  GeV/ $c$ ). DCA distribution for other centralities and energies can be found in Ref. [63].

From the 200 GeV triton signal distribution (first row of the Fig. 3.4.2), we can see that the signal significance of triton decreases very quickly as  $p_T$  increasing. We made a further examination of the triton signal and background with embedding data. We first compared the DCA distribution of the experimental measurement triton signals ( $|z_t| < 0.2$  and  $7.1 < m^2 < 8.7$  GeV<sup>2</sup>/ $c^4$ ) with the DCA distribution of the triton in the embedding data, as shown in Fig. 3.4.6. Here, we also learn that we can use embedding data for background subtraction when we cannot get the anti-particles, and this method still needs further study considering the errors introduced.

In the signal extraction, we use the exponential function in the signal interval to subtract a large background, in the signal concentration interval, whether this part of the background will be enhanced? whether the method used is reasonable? We use the side-band method to verify, we take the two sides of the signal, that is, the same width of the region adjacent to the signal interval, this part is called “side-band” as shown in Fig. 3.4.2 first row, their DCA distribution can be obtained from the experiment, and the DCA distribution of the total (signal + background) in the signal interval can also be obtained. We use the total dca distribution, subtract the dca distribution of the background provided by the side-band, we get the blue triangle in Fig. 3.4.2 second and third row, we use its dca distribution in the embedding data for comparison, from the

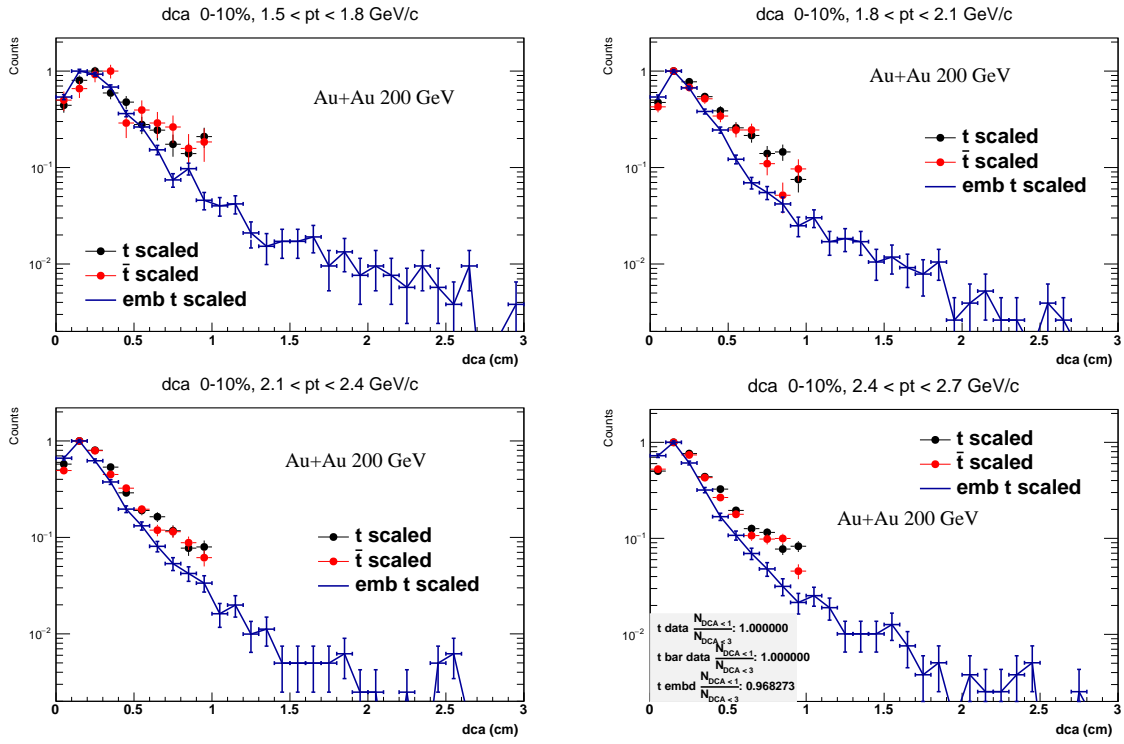


Figure 3.4.6: The DCA distribution of the triton in experimental measurements compared with that in embedding data at  $\sqrt{s_{NN}} = 200$  GeV in Au+Au collision, 0-10% centrality.



figure we can see that the dca distribution of the triton after subtracting the background matches very well with that of the embedding, this also shows that the background subtraction in our signal extraction is not a problem. Again, note that the DCA cut of the triton is taken as 1 cm in our experimental analysis, which shows that our measurement interval does not seem to introduce many knock-out triton.

## 3.5 Systematic Uncertainty Estimation

### 3.5.1 On transverse momentum spectra

Systematic uncertainties on the spectra are estimated by varying cuts and by assessing the purity of identified triton samples from  $dE/dx$  measurements. Details of various sources of systematic uncertainties on the triton yields in Au+Au collisions at  $\sqrt{s_{\text{NN}}} = 39$  GeV, 0-10% are given below. The systematic uncertainties for other energy are estimated in a similar manner and are of a similar order. The point-to-point systematic uncertainties on the transverse momentum spectra are estimated by varying event cuts ( $\sim 4\%$ ), track selection (Table 3.4), PID cuts, i.e.,  $|z_t|$  from 0.3 to 0.25 and 0.35, and bin width of the  $m^2$  distribution. Combined systematic uncertainties due to all these analyses cut around 7%. The systematic uncertainty due to track reconstruction efficiency and acceptance estimates is of the order of 5%, which is correlated with  $p_T$  and obtained by varying parameters of the MC simulation.

Table 3.4: Tracks cuts for systematic error.

	nFitPts $\geq$	ndE/dx $\geq$	DCA $<$
Default cut	20	10	1 cm
Varying cut	15,25	8,12	0.8 cm, 1.2cm

The results presented here are quadrature sums of these systematic uncertainties ( $\sim 10\%$ ), Table 3.5 gives a summary of various sources of systematic uncertainties for 39 GeV, 0-10%. For the other centralities and energies, the estimates of systematic error are of similar source, and the magnitude of the specific values is essentially similar. More detail for other energy can be found in Ref. [63].

The systematic errors are obtained by varying DCA, ndEdxHits, nHits, Bin width of  $m^2$

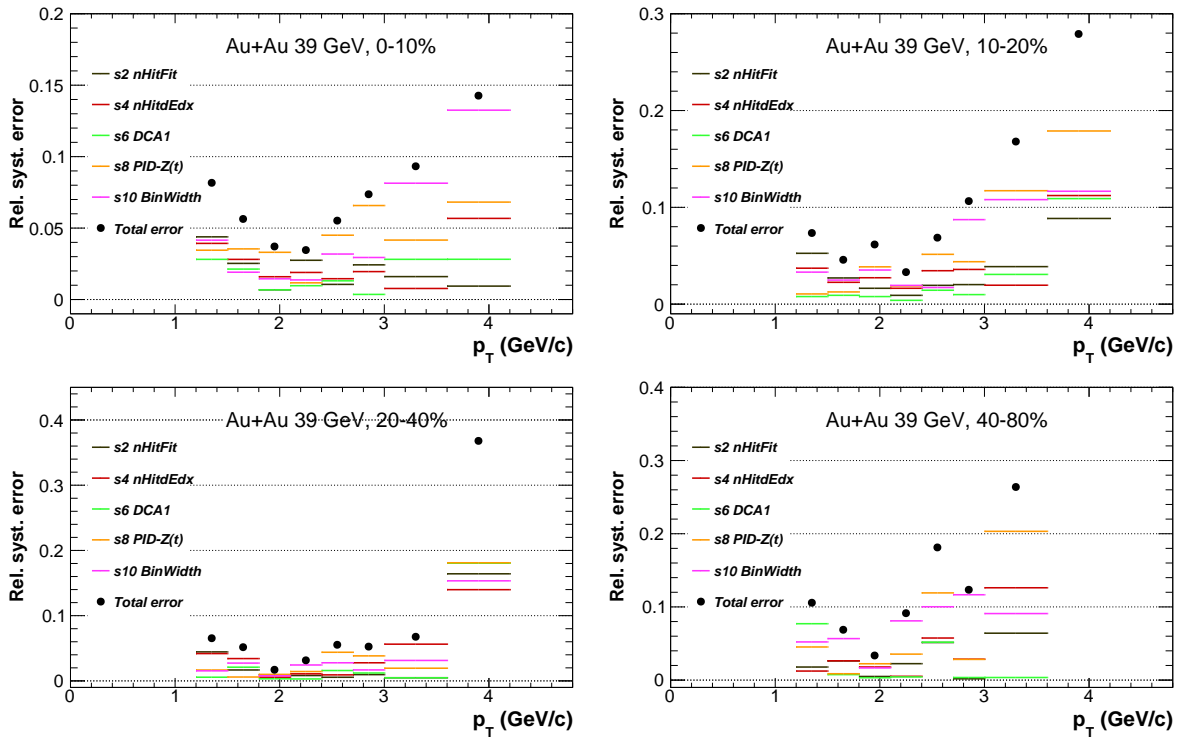


Figure 3.5.1: The relative systematic errors from different source for triton  $p_T$  spectra in Au+Au collisions at  $\sqrt{s_{NN}} = 39$  GeV.



Table 3.5: Sources of percentage systematic uncertainties for triton spectra at 39 GeV, 0-10%.

Source	Track cuts	Tracking eff.	$m^2$ distr. bin width	PID cuts
percentage	2-7%	5%	1-13%	1-7%

distribution and PID cuts in the analysis.

$$RMS = \sqrt{\frac{1}{N} \sum_{i=1}^N \left(\frac{X_i - Y}{Y}\right)^2} \quad (3.5.1)$$

where  $X$  stand for values with varying cuts,  $Y$  for value with default cut. For total systematic error,

$$SumErr = Y \times \sqrt{\sum_i RMS_i^2} \quad (3.5.2)$$

The corresponding system error distribution of 39 GeV is shown in Fig. 3.5.1.

### 3.5.2 On $dN/dy$ and $\langle p_T \rangle$

The triton yield measured at mid-rapidity ( $|y| < 0.5$ ) is calculated from the measured  $p_T$  range and extrapolated to the unmeasured regions with various parameterizations. The percentage contribution to the yields on extrapolation is about 10-20%, unmeasured regions of  $p_T$  are additional source of systematic error. The extrapolation is done by the individual blast-wave model fits [67].

$$\begin{aligned} \frac{1}{2\pi p_T} \frac{d^2 N}{dp_T dy} &\propto \int_0^R r dr m_T I_0 \left( \frac{p_T \sinh \rho}{T} \right) K_1 \left( \frac{m_T \cosh \rho}{T} \right) \\ \rho &= \tanh^{-1} \beta_r \\ \beta_r(r) &= \beta \left( \frac{r}{R} \right)^n \end{aligned} \quad (3.5.3)$$

where the extracted fit parameters are kinetic freeze-out temperature  $T_{kin}$ , average radial flow velocity  $\langle \beta \rangle$ , and the flow velocity profile exponent  $n$ .

The systematic uncertainties on the extrapolated yields are estimated by comparing the extrapolation with those using other fit functions. Another fit function is

$$\text{Double exponential} : A_1 \exp(-p_T^2/T_1^2) + A_2 \exp(-p_T^2/T_2^2) \quad (3.5.4)$$

The systematic uncertainties on the extrapolated total yields are dominated by the uncertainties in the extrapolation, which are estimated to be 10-20% of the extrapolated part of the integrated yields for triton. The 5% overall MC uncertainty is added in quadrature.

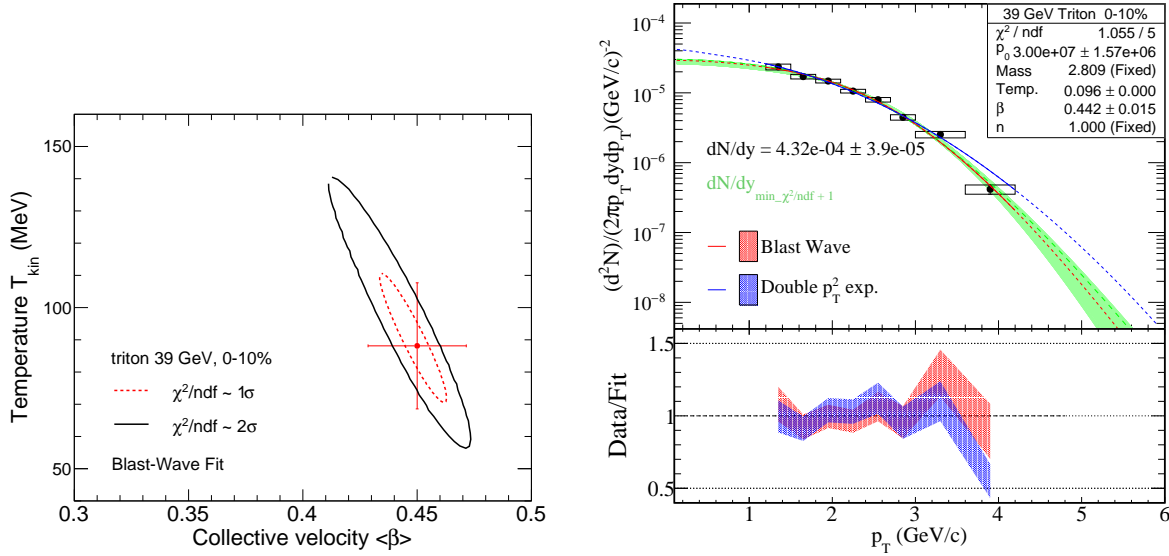


Figure 3.5.2: The  $p_T$  spectra was fitted using the method of parametric scan, left: contours returned by the parametric fit; right: distribution of the scanned parametric range function in green band.

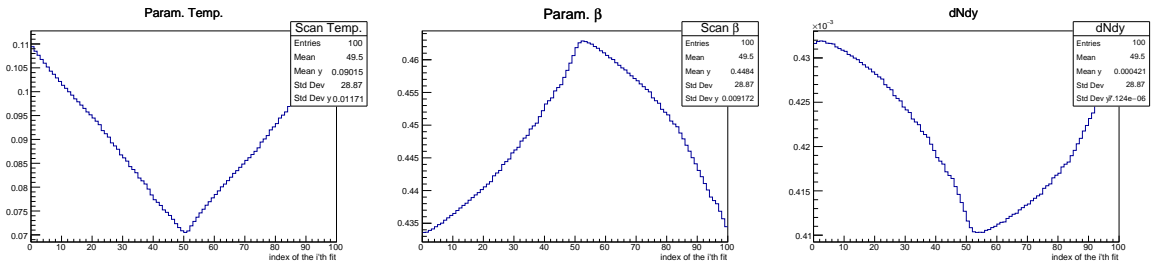


Figure 3.5.3: Variation of the parameters and integral yields within the parameters one sigma error range.



To ensure reasonable systematic error estimations for the different function fits, an alternative method was implemented. The specific procedure involved fitting the measured  $p_T$  spectra with the Blast-wave function to obtain return parameters and errors for temperature  $T_{kin}$  and collective velocity  $\langle\beta\rangle$  while fixing parameters mass and  $n$ . After the fitting, a parameter scan was performed within the parameter error, and the results for the two and one sigma error range were shown in the contours on the left of Fig. 3.5.3. All of the parameters used in the scan were then brought into the Blast-wave function, and the specific results were shown in the range presented in the middle panel of the figure in green. The rightmost part of the figure showed the variation range of the parameters (upper for  $T_{kin}$ , middle for  $\langle\beta\rangle$ ) and the integral  $dN/dy$  (lower) due to the variation in the one sigma range of the parameter error. The calculations showed that the error estimated through this alternative method is comparable to that obtained using different functions, demonstrating the trustworthiness of the error estimation method used.

The triton average transverse momentum  $\langle p_T \rangle$  is also extracted from the measured  $p_T$  range and extrapolation. Systematic uncertainties on  $\langle p_T \rangle$  are also estimated by using the various functional forms mentioned before for extrapolation of the yield.

# Chapter 4

## Analysis Details for Proton

In heavy-ion collisions, one of the main production sources of the (anti)protons is the weak decay of strange baryons and their anti-particles, such as  $\Lambda$ ,  $\Sigma^+$ ,  $\Xi^0$ ,  $\Xi^-$ ,  $\Omega^-$ . The corresponding decay channels and branching ratios are [3]

$$\begin{aligned}\Lambda &\longrightarrow p + \pi^-, \text{ branching ratio} = 63.9\% \\ \Sigma^+ &\longrightarrow p + \pi^0, \text{ branching ratio} = 51.57\% \\ \Xi^- &\longrightarrow \Lambda + \pi^-, \text{ branching ratio} = 99.887\% \\ \Xi^0 &\longrightarrow \Lambda + \pi^0, \text{ branching ratio} = 99.524\% \\ \Omega^- &\longrightarrow \Lambda + K^-, \text{ branching ratio} = 67.8\%\end{aligned}$$

Usually, the primordial yields of (anti)protons are more commonly used to study the properties of the hot dense medium created in heavy-ion collisions. Therefore, those (anti)protons from the weak decay contributions need to be subtracted from their inclusive yields.

### 4.1 Data Set

The STAR experiment has published the inclusive yields of protons and (anti)protons at mid-rapidity in Au+Au collisions at  $\sqrt{s_{\text{NN}}} = 7.7 - 200$  GeV [68, 66, 69, 70, 71]. In STAR, the subtractions are not done on an event-by-event basis, but by subtracting the decayed (anti)protons  $p_T$  spectra from the spectra of inclusive (anti)protons. To simulate the decay kinematics of strange baryons within real detector acceptance, the so-called Monte Carlo (MC) embedding technique is



used. The MC strange baryons with flat  $p_T$  are embedded into the real data and go through a realistic GEANT detector simulation. Then, the MC strange baryons are decayed into (anti)protons based on the branching ratios. Finally, the  $p_T$  spectra of decayed (anti)protons are weighted by a factor, which is the ratio of the measured  $p_T$  spectra of strange baryons over the embedded ones. Experimentally, the  $p_T$  spectra and yields of  $\Lambda$ ,  $\Xi^-$  and  $\Omega^-$  in Au+Au collisions measured at RHIC BES-I energies have been reported in Ref. [72, 73]. As the  $\pi^0$  and their decay daughters are difficult to detect at mid-rapidity in the STAR experiment, the  $\Xi^0$  and  $\Sigma^+$  are not measured. However, we assume that the  $\Xi^0$  and  $\Xi^-$  have the same  $p_T$  spectra due to the similar mass and lifetime. In addition, based on the  $\Sigma^+/\Lambda$  ratio from thermal model, the  $p_T$  spectra of  $\Sigma^+$  are obtained by multiplying the  $p_T$  spectra of  $\Lambda$  by a factor of 0.27, which is  $p_T$  and centrality independent. To account for the uncertainty from this assumption, a 20% relative error is added to the  $\Sigma^+$  spectra.

Table 4.1: Spectra data reference

$\sqrt{s_{NN}}$	Year	Inclusive Proton	Strangeness Hadron	Embedding Data
7.7	2010	$ y  \leq 0.1$ [68]	$ y  \leq 0.5$ [73]	Official(2010)
11.5	2010	$ y  \leq 0.1$ [68]	$ y  \leq 0.5$ [73]	Official(2010)
14.5	2014	$ y  \leq 0.1$ [69]	$ y  \leq 0.5$ STAR Prelim.	Official(2014)
19.6	2011	$ y  \leq 0.1$ [68]	$ y  \leq 0.5$ [73]	Official(2011)
27	2011	$ y  \leq 0.1$ [68]	$ y  \leq 0.5$ [73]	Official(2011)
39	2010	$ y  \leq 0.1$ [68]	$ y  \leq 0.5$ [73]	Official(2010)
54.4	2018	$ y  \leq 0.1$ STAR Prelim.	$ y  \leq 0.5$ STAR Prelim.	Official(2018)
62.4	2004	$ y  \leq 0.5$ [70] $ y  \leq 0.1$ [66]	$ y  \leq 1.0$ [72]	New Request(2010)
200	2011	$ y  \leq 0.1$ [66]	[74]	–

Table 4.1 presents the inclusive proton spectra, strange hadron spectra, and STAR official simulation data from **GSTAR** that were used for the proton feed-down correction. At energies of 62.4 and 200 GeV, special instructions are required. For 62.4 GeV, the inclusive proton and strangeness hadron spectra were taken from the same data collected in 2004, but there are two different spectra for inclusive proton with rapidity of 0.1 [66] and 0.5 [70]. Due to changes in the STAR server, only the same collision energy data collected in 2010 is currently accessible, so we have requested new embedding data based on the 2010 data. When performing the proton

weak-decay feed-down correction, the rapidity window for decayed proton cannot be the same as that for inclusive proton; otherwise, we would obtain relatively different results. Therefore, we use the same rapidity as that for strange hadron particles as it yields a more reasonable result. We understand that due to the different data sets, only particles with the same mid-rapidity can be selected. For 200 GeV, the feed-down correction for proton is provided in [66], and we have used the same method as the one in the mentioned paper. Therefore, we have not made any further correction and have directly used the yields and fractions available in the paper data.

## 4.2 Feed-down Correction Procedure

In this study, we performed two main steps. Firstly, we parameterized the strange hadron spectra and calculated the extrapolated uncertainties based on the difference between Blast-wave and Boltzmann functions. Secondly, we weighted the input MC  $\Lambda$ ,  $\Xi^-$ , and  $\Omega^-$  using the corrected spectra and decayed these strange hadrons, while considering the different branching ratios for each hyperon. We obtained daughter protons from the decay process, which were then appropriately scaled using the weight factor obtained from the previous step.

To illustrate the detailed process of the proton feed-down correction, we will use the 39GeV at 0-10% centrality as an example. In Fig. 4.2.1, we present the weighted MC transverse momentum spectra of the strange hadron, where the black circles represent the STAR experimental measurements. This step allows us to obtain the weighting factor at each transverse momentum.

Fig. 4.2.2 depicts the transverse momentum distribution of a proton that has undergone decay from a strange hadron. It is noteworthy that in the STAR embedding data, each particle can be labeled and identified using its respective ID. After the strange hadron decay, open circles can be observed in the figure. The red circles represent the blast-wave function, parameterized based on the strange hadron spectra, whereas the blue ones symbolize the Boltzmann function that is parameterized based on the strangeness hadron transverse momentum distribution. It is important to highlight that the difference between these two functions plays a critical role in the calculation of the systematic error in the decayed proton yield. Additionally, it is worth noting that the embedding data employed in this step relies heavily on the primary relations:

$$\frac{N_{\text{Protons come from the decay of MC strange particles}}}{N_{\text{Strange particles generated by MC}}} = \frac{N_{\text{Protons come from the decay of measured strange particles}}}{N_{\text{Strange particles from measurement}}} \quad (4.2.1)$$

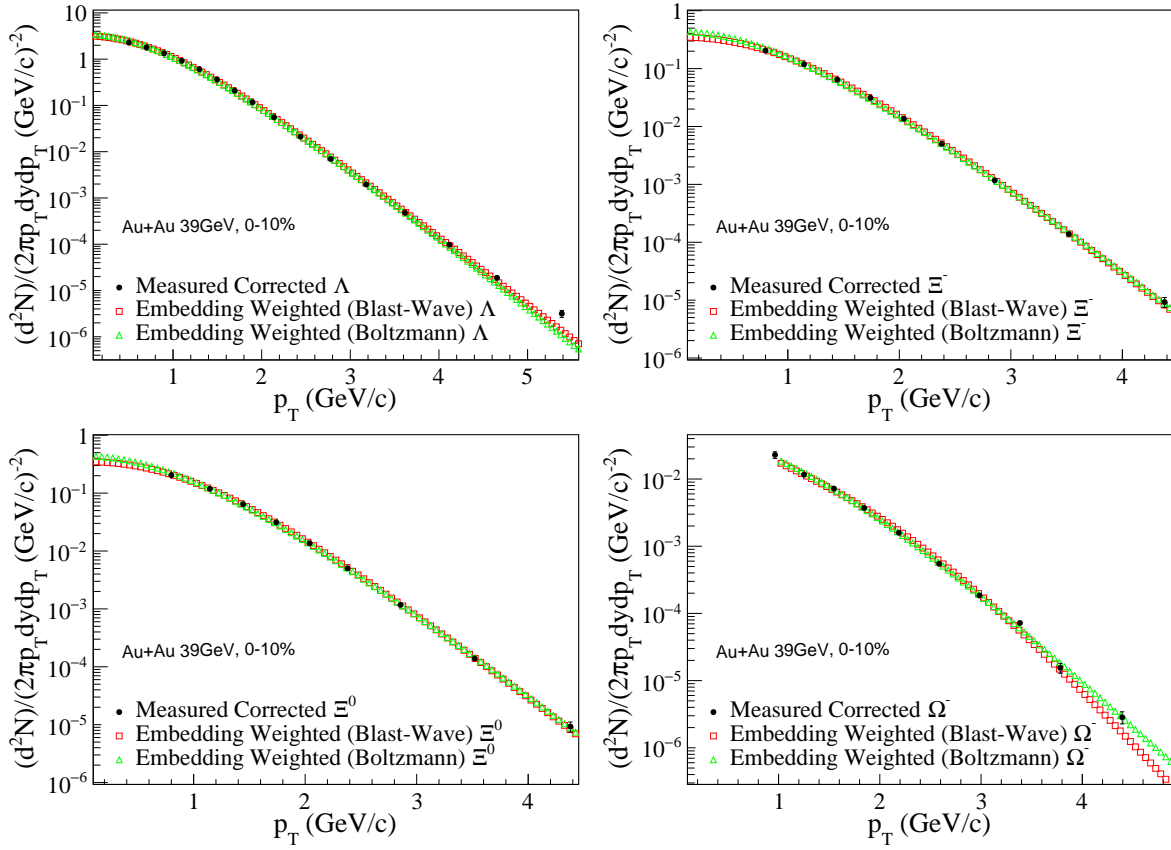


Figure 4.2.1: Input Monte Carlo parent or parentparent particles spectra from Au+Au collision 0-10% centrality at 39 GeV.

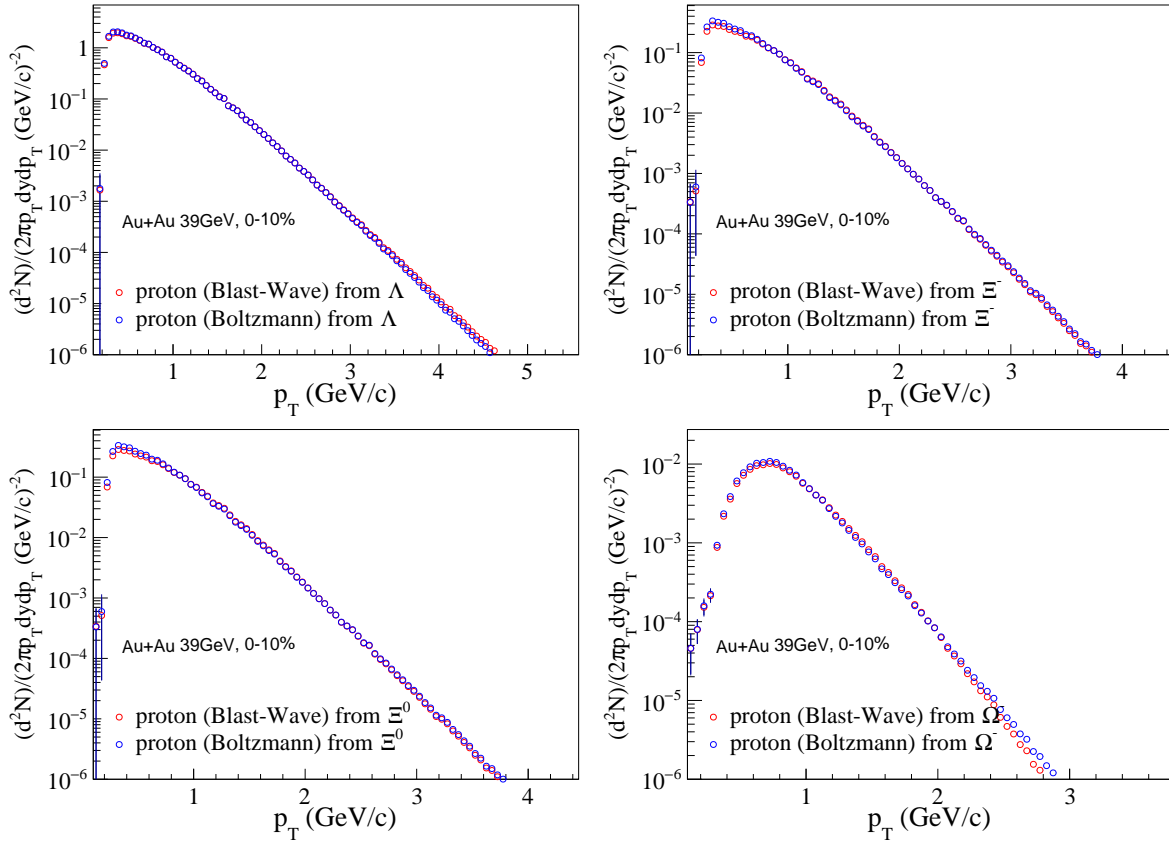


Figure 4.2.2: Decayed proton from the embedding sample from Au+Au collision 0-10% at 39 GeV.



where  $N_i$  represents the differential yield on each particle transverse momentum spectra.

The proton weak decay feed-down fraction is defined as

$$\text{Feed-down fraction} = \frac{dN/dy_{\text{Protons come from the weak decay of strange particles}}}{dN/dy_{\text{Inclusive proton}}} \quad (4.2.2)$$

Fig. 4.2.3 on the left shows all daughter protons from different parent particles on the same plot. The lower panel displays the feed-down fraction, with the decayed proton from lambda being dominant. To obtain a smooth correction as a function of  $p_T$ , a function that approximates the shape of the decayed proton is utilized. We then subtract the daughter proton to obtain the primordial proton, eventually utilizing the standard error propagation formula to handle errors. Fig. 4.2.3 on the right, the red and blue solid circles depict the differential yield for the inclusive and primordial protons, respectively. The open blue circles show the primordial protons from a published paper [75], which have been corrected for weak decay feed-down using UrQMD + GEANT simulation. However, this correction introduces significant uncertainties to the model, and the cause of the difference between the corrected and uncorrected data is not yet fully understood. Therefore, further investigation is necessary to elucidate this issue.

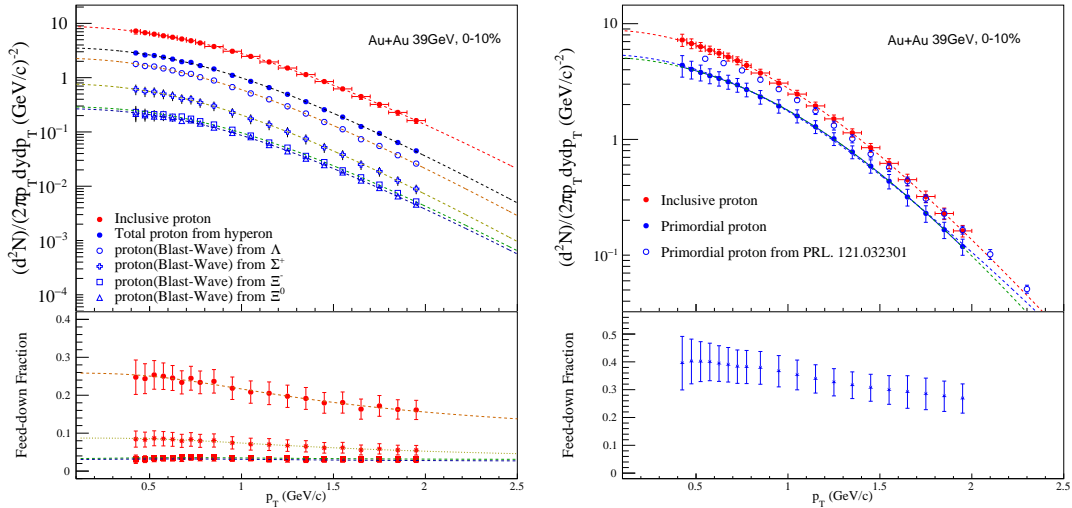


Figure 4.2.3: The primordial proton from total feed-down correction from Au+Au collision 0-10% at 39 GeV.

### 4.3 Feed-down Correction Results

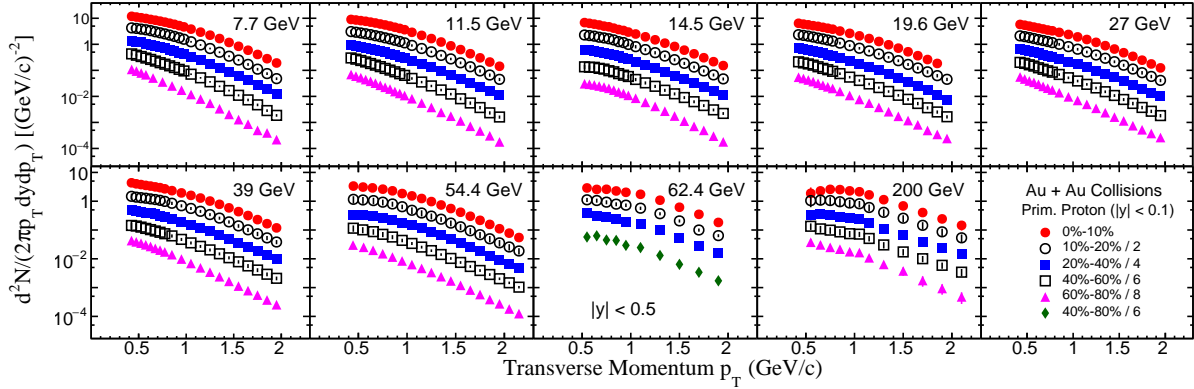


Figure 4.3.1: Mid-rapidity transverse momentum spectra for primordial protons.

After implementing the necessary correction steps, we were able to derive the transverse momentum dependent distribution of the primordial protons, as depicted in Fig. 4.3.1. It is important to note that, for a proton energy of 62.4 GeV, we utilized an inclusive proton with  $|y| < 0.5$ , however, other energies may necessitate different rapidity windows. Recently, the STAR Collaboration updated the strange particle yields of  $\sqrt{s_{NN}} = 62.4$  GeV, which may prompt us to update our primordial proton yield estimates. Our preliminary findings suggest that the updated results will not differ significantly from our present outcomes. With regard to the primordial proton yield of 200 GeV, previous study employed a data-driven method for weak decay feed-down correction with  $p_T$  up to 10 GeV, however, we have only included results before 2 GeV in the plot to enable further comparison with other energy outcomes. Additional details regarding our methodology may be found in Ref. [63].

In Fig 4.3.2, the energy dependence of the weak decay fraction for protons and (anti)protons in 0-10% central Au+Au collisions is presented. The results for protons and (anti)protons are shown using black-filled and black-open circles, respectively. It can be observed that the weak decay feed-down fraction of protons decreases monotonically with decreasing collision energy, while the results for (anti)protons show the opposite trend.

It is worth noting that prior to measuring strange particles, STAR performed weak decay feed-down corrections for protons using UrQMD + GEANT simulation [75]. However, when compared



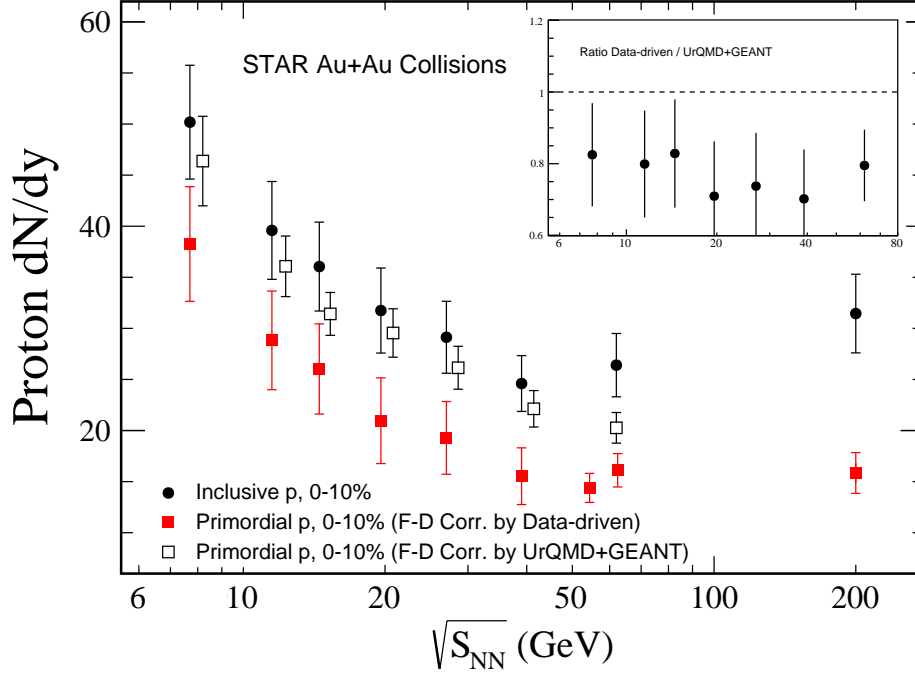


Figure 4.3.3: The energy dependence of the primordial proton yields at mid-rapidity estimated from the data-driven method (red filled squares) and UrQMD+GEANT (open squares). The black filled circles are inclusive protons. The ratio of the data-drive method to UrQMD+GEANT method is shown in the inner panel.

to the results from the data-driven method mentioned above, the UrQMD+Geant simulation overestimated the primordial proton yields at mid-rapidity, as shown in Fig. 4.3.3. For data on the primordial (anti)proton  $p_T$  spectra in Au+Au collisions at 7.7 - 200 GeV, please refer to Ref. [76].

## 4.4 Systematic Uncertainty Estimation

### 4.4.1 On Primordial Proton Yields

We used the standard error propagation formula to transfer the error of the inclusive proton spectra to the error of the primordial proton spectra. For the variable  $x_1, x_2$ , the standard error  $\sigma_{x_1}, \sigma_{x_2}$ , the general error evolution is as follows



$$(x_1 + x_2) \pm \sqrt{\sigma_{x_1}^2 + \sigma_{x_2}^2} \quad (4.4.1)$$

$$(x_1 - x_2) \pm \sqrt{\sigma_{x_1}^2 + \sigma_{x_2}^2} \quad (4.4.2)$$

For the statistical error, the error of the inclusive proton is given in the published data, and the statistical error of the proton from the decay of the strange particle is combined by the statistical error of the simulation data. When the spectrum of the inclusive protons is subtracted from the spectrum of the protons from decay, the error is propagate by Eq. 4.4.1.

For the systematic error on the transverse momentum of the decayed protons, it is obtained by the difference between the different decayed proton spectra, which obtained from the weak decay of the strange particles parameterized by different functions, as shown in Fig. 4.2.2. The systematic error of the primordial proton spectra is then obtained from these two components by Eq. 4.4.1. For the protons from  $\Sigma^+$  decay, because the  $\Sigma^+$  spectra cannot be measured directly, a systematic error of 20% is added in this step with respect to the protons from  $\Sigma^+$  decay.

We fitted the decayed proton spectrum with different functions to obtain the integral yield and statistical error of the decayed protons, as well as the systematic error. As shown in Fig. 4.4.1, the systematic errors are extracted from the differences of the different functions. The primordial proton integral yield is obtained by subtracting the decayed proton integral yield from the inclusive proton integral yield, and its statistical and systematic errors are obtained from the statistical and systematic errors of the inclusive proton integral yield and the integral yield of the decayed proton by Eq. 4.4.1.

#### 4.4.2 On Light Nuclei Yield Ratio ( $N_t \times N_p/N_d^2$ )

The estimation of systematic errors in the light nuclei yield ratio ( $N_t \times N_p/N_d^2$ ) is a complex problem that has undergone much investigation. The ratio is calculated based on the yields of protons, deuterons, and tritons, and the systematic error in the yields of these particles mostly comes from the unmeasured interval. The challenge in the error estimation of the ratio arises from the fact that these different particles are distributed mainly in different transverse momentum intervals. After extensive discussions, the final approach was to employ five different functions to simultaneously fit the proton, deuteron, and tritium nuclei, as demonstrated in Fig. 4.4.2.

The Blast-wave and Double  $p_T$  exponential as shown in Eq. 3.5.3 and Eq. 3.5.4. Other functions are showing at below.

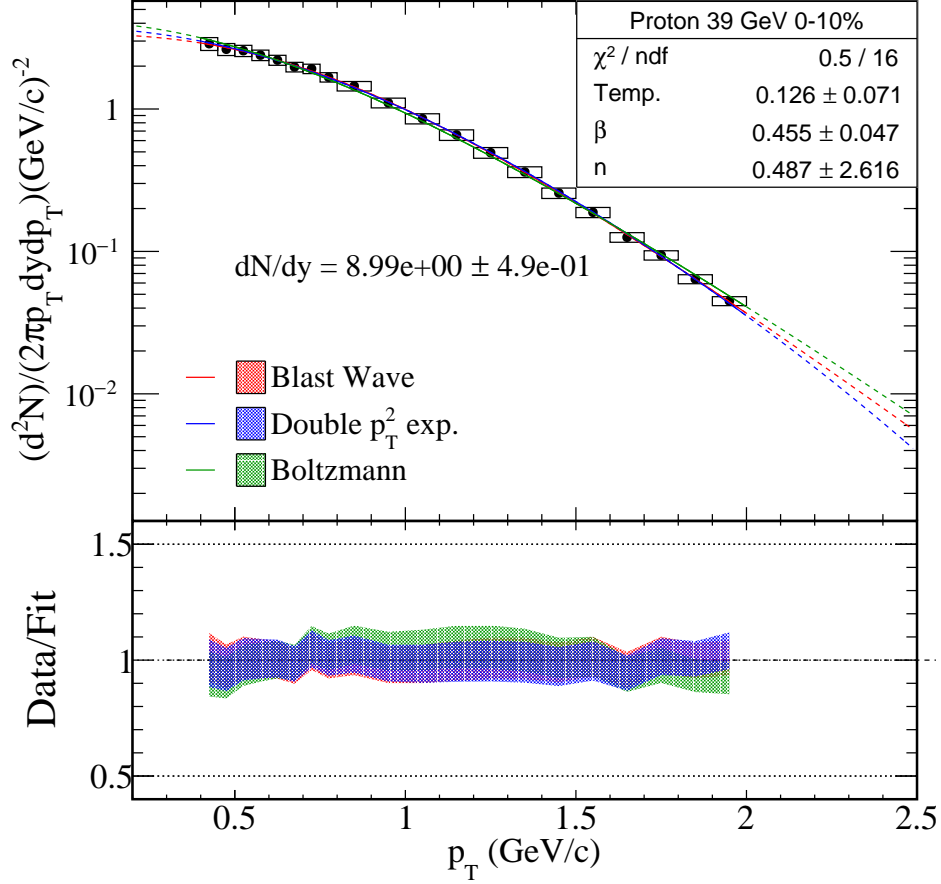


Figure 4.4.1: The decayed proton spectra fitted by different function.

Boltzmann:

$$Am_T \exp(-m_T/T_B) \quad (4.4.3)$$

Levy:

$$p_1 \left(1 + \frac{\sqrt{p_0^2 + p_T^2} - p_0}{p_2 p_3}\right)^{-p_2} \quad (4.4.4)$$

 $m_T$  exponential:

$$p_1 \exp\left(-\frac{\sqrt{p_T^2 + p_0^2}}{p_2}\right) \quad (4.4.5)$$

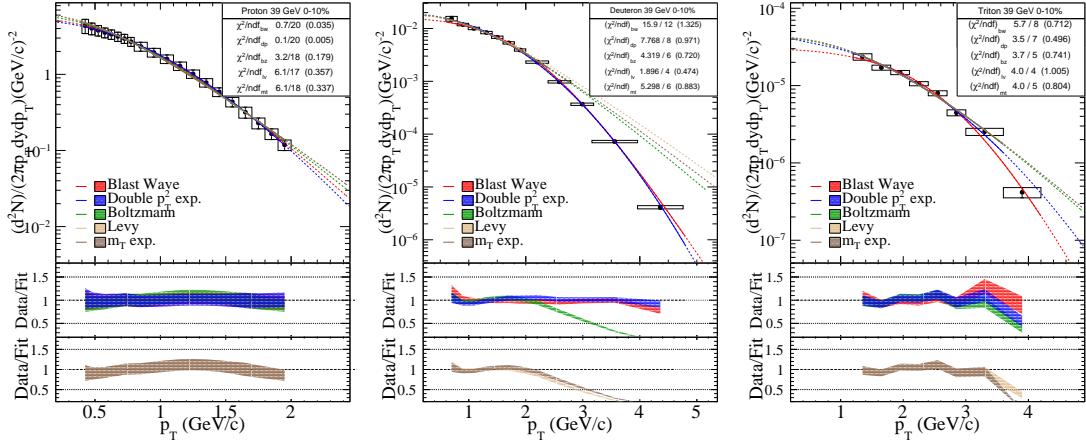


Figure 4.4.2: Applying the same fit function to each individual particle spectra.

To obtain consistent results across different particles, the fits utilized in this analysis are mostly based on the low momentum interval, with adjustments made to the fit interval as needed. The fit criteria are established based on the returned  $\chi^2/ndf$ , ensuring that the same function is fitted to different particles under the same criteria. Once the fit is completed, the yields of the proton, deuteron and triton are obtained under the same function. The  $N_t \times N_p/N_d^2$  ratio is then calculated using the default value obtained from the Blast-wave function, while any difference between this default value and the other functions reflects the systematic error associated with the ratio.

After analyzing the ratios obtained by different functions, as shown in the upper panel of Fig. 4.4.3, which includes Blast-wave ( $r_{bw}$ ), double  $p_T$  exponential function ( $r_{dp}$ ), Boltzmann function ( $r_{bz}$ ), Levy function ( $r_{lw}$ ), and  $m_T$  exponential function ( $r_{mt}$ ), it can be seen that the results of the other functions are significantly larger than Blast-wave. This indicates that there is a correlated systematic error in the distribution of energy dependence obtained in the previous discussion. To estimate the standard deviation w.r.t the default, we used Eq. 4.4.6 and separated the error into two parts: a common and a random part.

$$SD_{bw} = \sqrt{\frac{(r_{dp} - r_{bw})^2 + (r_{bz} - r_{bw})^2 + (r_{lw} - r_{bw})^2 + (r_{mt} - r_{bw})^2}{4}} \quad (4.4.6)$$

The standard deviations of the results of the other functions with respect to Blast-wave were obtained in the lower panel of Fig. 4.4.3, and the experimental standard deviation of the mean

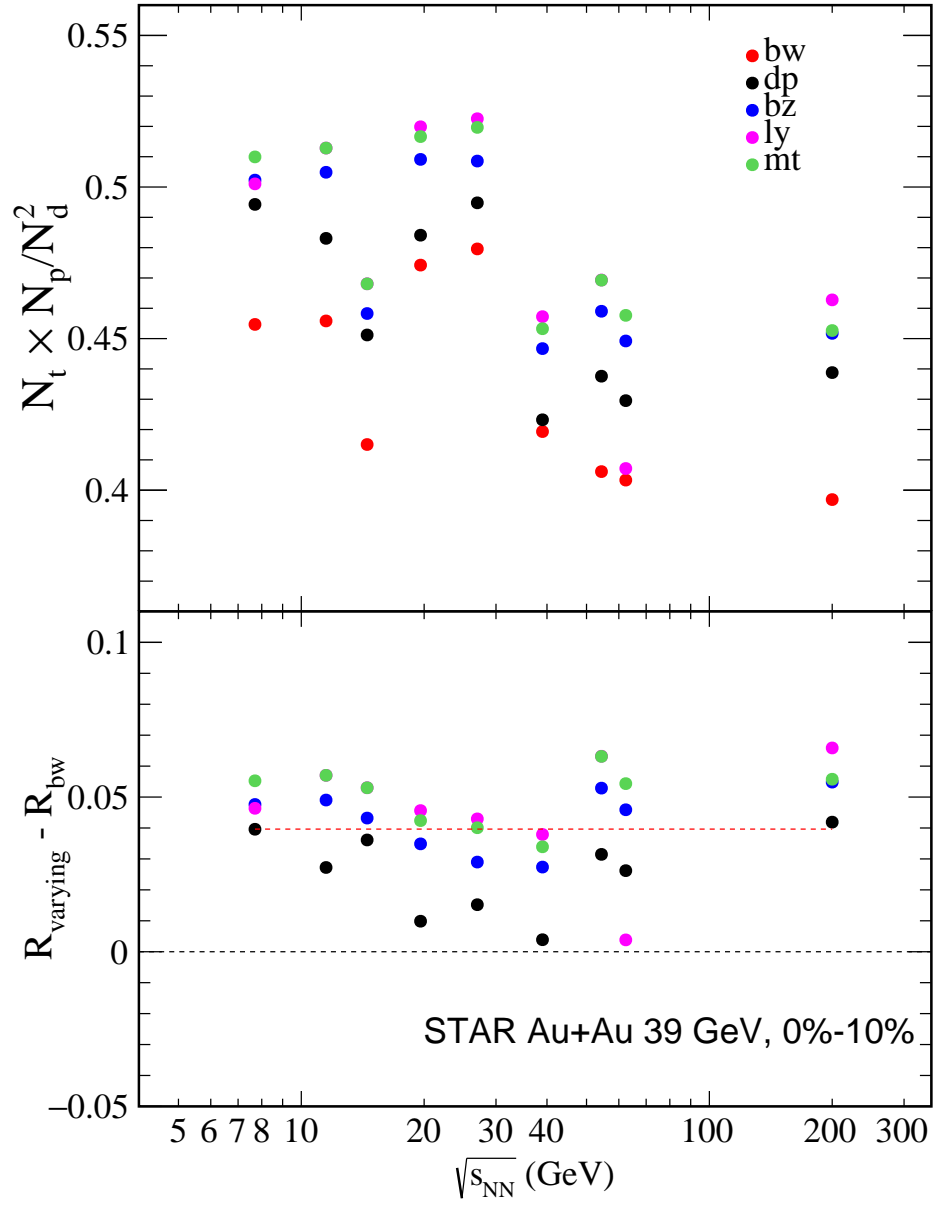


Figure 4.4.3: Upper: The  $N_t \times N_p / N_d^2$  from the different fit function. Lower: The arithmetic mean and variance of the deviations.



calculated by Eq. 4.4.7-4.4.9 ( $x_i$  indicates the each  $R_{varying} - R_{bw}$ ) was obtained as the correlated common error  $\sigma_{sys-comm}$  of  $N_t \times N_p / N_d^2$  as a function of collision energy, as shown the red dashed line in the lower panel of Fig. 4.4.3. The random systematic error ( $\sigma_{sys-random}$ ) was estimated at each energy point using Eq. 4.4.10. In the distribution of  $N_t \times N_p / N_d^2$  as a function of  $dN_{ch}/d\eta$ , the average of the common error of different centrality was taken as the error correlated with  $dN_{ch}/d\eta$ , which is the common error, and the random error of each point was kept, as shown in Fig. 5.4.2 and Fig. 5.4.3.

$$\bar{x} = \frac{\sum x_i}{n} \quad (4.4.7)$$

$$v_i = x_i - \bar{x} \quad (4.4.8)$$

$$\sigma_{sys-comm} = \sqrt{\frac{v_1^2 + v_2^2 + \dots + v_n^2}{n-1}} \quad (4.4.9)$$

$$R_{sys-random} = \sqrt{(SD_{bw})^2 - (\sigma_{sys-comm})^2} \quad (4.4.10)$$

# Chapter 5

## Results and Discussion

### 5.1 Transverse Momentum Spectra

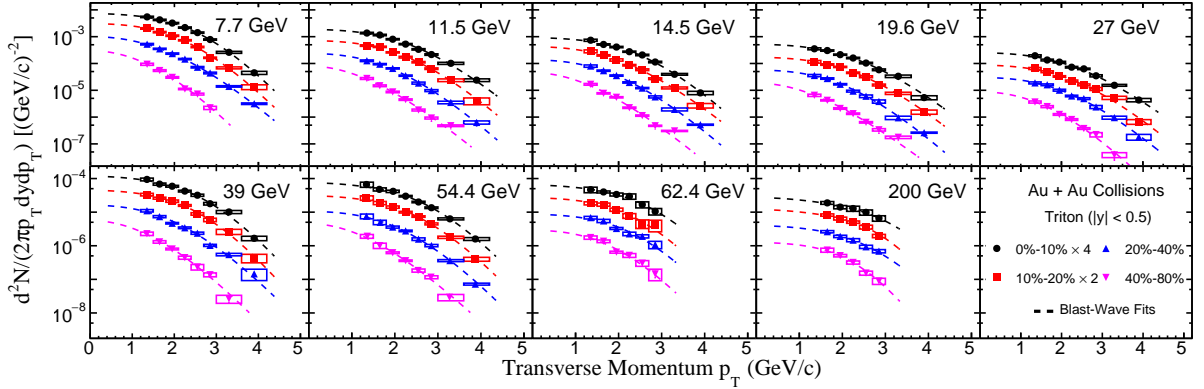


Figure 5.1.1: Transverse momentum ( $p_T$ ) spectra for mid-rapidity ( $|y| < 0.5$ ) tritons from 0%-10%, 10%-20%, 20%-40%, and 40%-80% centralities in Au + Au collisions at  $\sqrt{s_{\text{NN}}} = 7.7, 11.5, 14.5, 19.6, 27, 39, 54.4, 62.4,$  and 200 GeV. Dashed-lines are the corresponding Blast-Wave fits with the profile parameter  $n = 1$ . The statistical and systematic uncertainties are shown as vertical lines and boxes, respectively.

In Fig. 5.1.1, the mid-rapidity ( $|y| < 0.5$ ) transverse momentum spectra for triton ( $t$ ) in



Au+Au collisions at  $\sqrt{s_{\text{NN}}} = 7.7, 11.5, 14.5, 19.6, 27, 39, 54.4, 62.4,$  and 200 GeV for 0-10%, 10-20%, 20-40%, and 40-80% centralities are presented. The systematic error is shown in the boxes and the statistical error is shown separately by vertical lines. The dash lines show the individual fits with the blast-wave function. The  $p_T$  spectra show a clear evolution and become somewhat softer from central to peripheral collisions, this behavior is also observed for other measured hadrons. These spectra can be further characterized by the  $dN/dy$  and  $\langle p_T \rangle$  for the produced tritons.

## 5.2 Coalescence Parameters

In the coalescence picture, the invariant yield of light nuclei is directly proportional to that of nucleons as previously discussed in section 1.4.2. It is essential to note that this assumption considers the ratio of neutrons to protons to be unity. Furthermore, the coalescence parameter, represented by  $B_A$ , serves as a measure of the probability of nucleon coalescence, which is dependent on local nucleon density. In this study, the triton results are analyzed in conjunction with primordial proton spectra, and the data is corrected using a data-driven approach that combines strange hadron spectra.

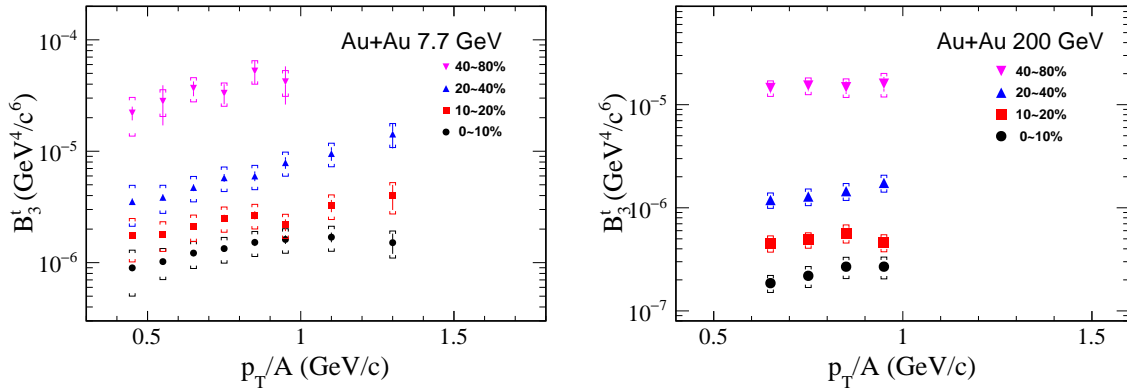


Figure 5.2.1: Coalescence parameter  $B_3$  as a function of transverse momentum scaled with the mass number ( $p_T/A$ ) for triton from 7.7 GeV (left panel) and 200 GeV (right panel) 0-10%, 10-20%, 20-40%, and 40-80% Au+Au collisions. The square brackets show systematic error and vertical lines show the statistical error separately.

The coalescence parameters are presented in Fig 5.2.1. The coalescence parameters  $B_3$  for

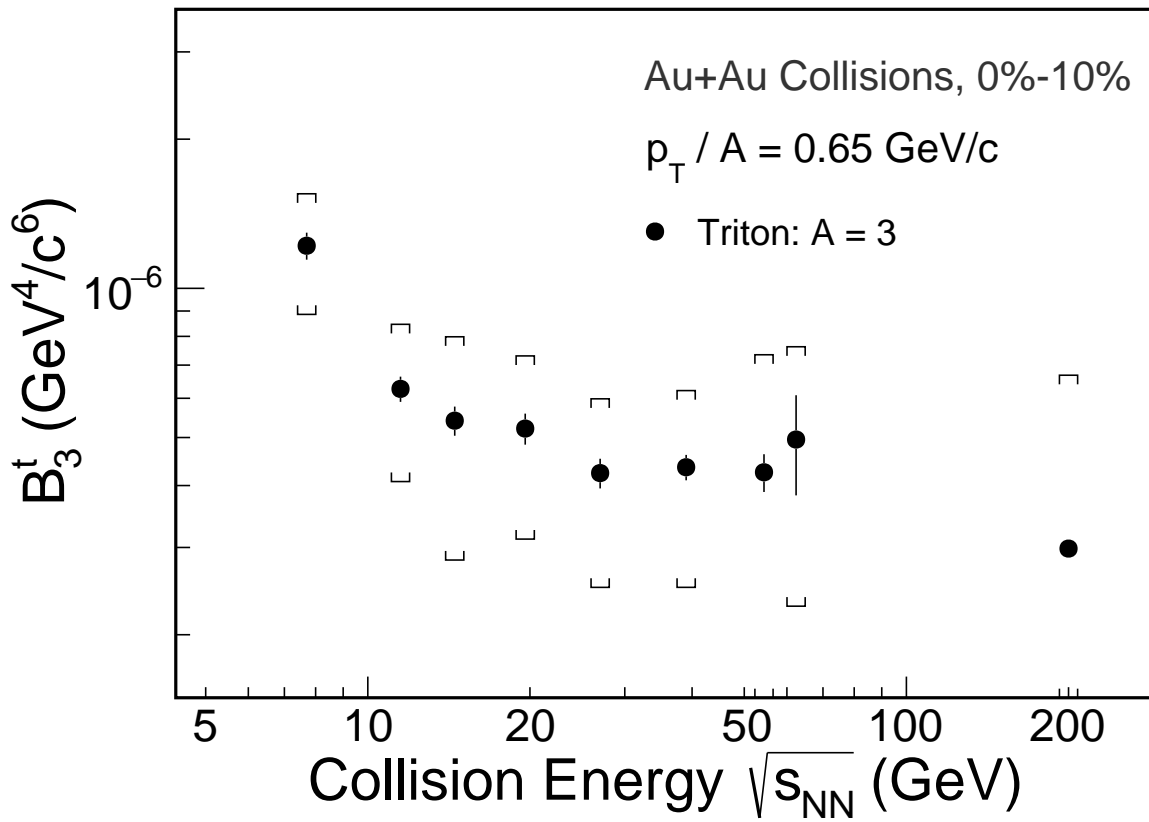


Figure 5.2.2: Coalescence parameter  $B_3$  as a function of collision energy at  $p_T/A = 0.65 \text{ GeV}/c$ .



other energy can be found in Ref. [63]. It can be found that  $B_3$  increase with increasing  $p_T$  which might suppose an expanding collision system.  $B_3$  increase with centrality which can be explained by a decreasing source volume, the smaller the distance between the protons and neutrons which are created in the collision, the more likely it is that they coalesce. Fig. 5.2.2 shows 0-10%  $B_3$  ( $p_T/A = 0.65$  GeV/c) from triton. The coalescence parameters  $B_3$  trend decrease with increasing  $\sqrt{s_{NN}}$  implied that the emitting source increase with decreasing collision energy.

### 5.3 Particle Integral Yields ( $dN/dy$ ) and Average Transverse Momentum ( $\langle p_T \rangle$ )

We used the blast wave function to describe the triton spectra presented in Fig. 5.3.1. Thought the fit, we were able to determine the kinetic freeze-out temperature, transverse radio flow velocity and integral the function, as well as calculate the yield of triton and  $\langle p_T \rangle$ . The blast wave function also provided a fit for the triton spectra at different energies and centralities, which can be found in Ref. [63].

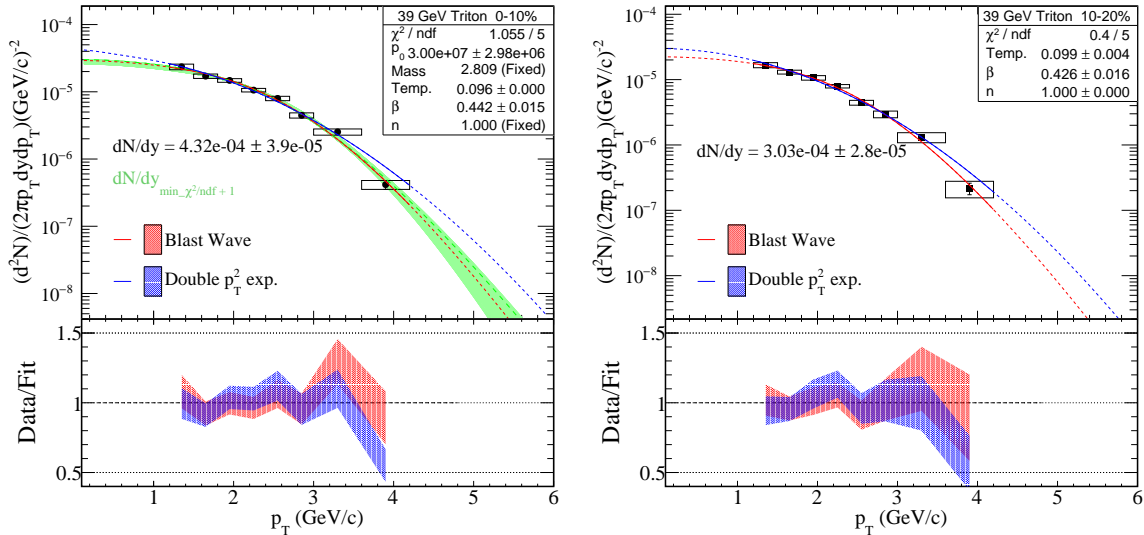


Figure 5.3.1: Blast-Wave function fit for triton spectra. Centrality dependence of 0-10% (left panel) and 10-20% (right panel) in Au+Au collisions at  $\sqrt{s_{NN}} = 39$  GeV.

In Fig. 5.3.2 upper panel, we have shown the  $dN/dy$  results for triton in collisions with  $\sqrt{s_{NN}} = 7.7 \sim 200$  GeV. The statistical and systematic uncertainties are shown separately. The triton yield is higher at lower collision energy, implying a higher baryon density at mid-rapidity due to the baryon stopping effect. Proton production at STAR comes from two mechanisms: baryon stopping and pair production. The observed energy dependence trend for the triton is a result of the interplay between these two mechanisms. Similarly to protons and deuterons, the centrality dependence of the triton shows that the yield decreases from central to peripheral collisions.

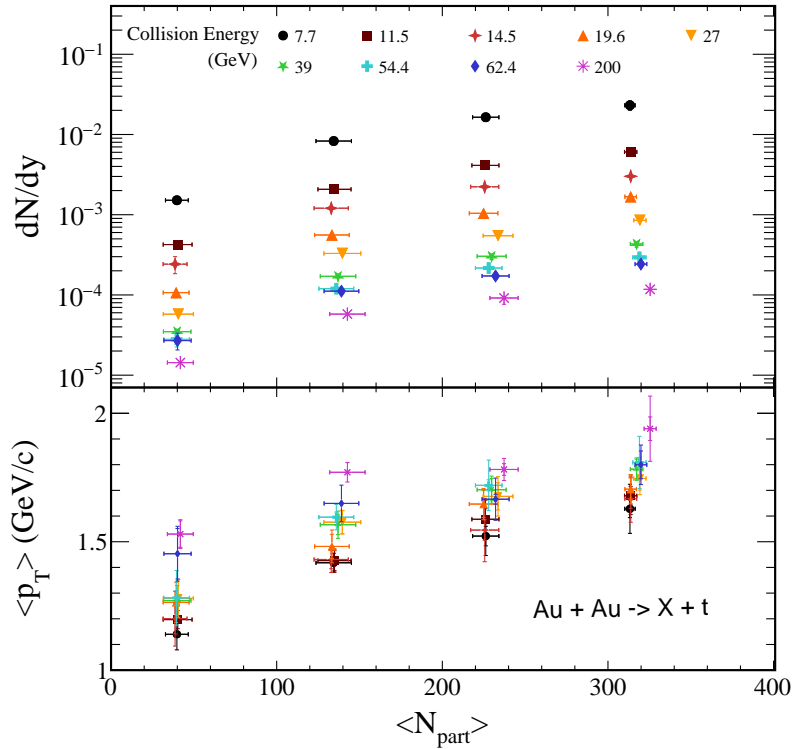


Figure 5.3.2: Centrality dependence of  $dN/dy$  (upper panel) and  $\langle p_T \rangle$  (lower panel) of triton in Au+Au collisions at  $\sqrt{s_{NN}} = 7.7 \sim 200$  GeV. Errors shown are the statistical and systematic uncertainties separately.

The lower panel in Fig. 5.3.2 shows the average transverse momentum ( $\langle p_T \rangle$ ) of triton as a function of average number of participating nucleons ( $\langle N_{part} \rangle$ ) in Au+Au collisions at  $\sqrt{s_{NN}} =$



7.7 ~ 200 GeV. It is observed that  $\langle p_T \rangle$  of tritons increase significantly as the centrality of the collisions increase. This trend is consistent across all energies. For a given collision centrality, the  $\langle p_T \rangle$  of tritons at higher energies is almost always larger than at lower energies, indicating a stronger radial flow.

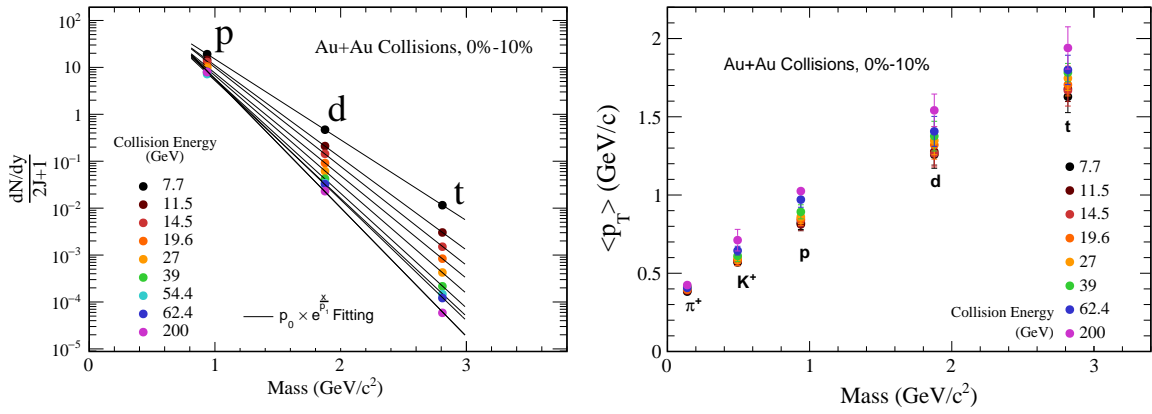


Figure 5.3.3: Mass dependence of light nuclei yields (divided by the spin degeneracy factor)  $dN/dy$  (upper panel) in Au+Au collisions at  $\sqrt{s_{NN}} = 7.7 \sim 200$  GeV. Mass dependence of average transverse momentum  $\langle p_T \rangle$  for the particles in Au+Au collisions at  $\sqrt{s_{NN}} = 7.7 \sim 200$  GeV.

The figure presented in the left side of Fig. 5.3.3 shows the integral yield distribution of the particle mass dependence, with the yield on the vertical axis divided by the spin degeneracy factor. The distribution indicates that the decrease from proton to triton is quicker with increasing collision energy since the baryon number density decreases as the energy increases. The distribution on the left side was fitted with an exponential function and showed an excellent fit result. In the thermodynamic statistical model, particle yields are filled with the Boltzmann factor, which is expressed in the form of an exponential function. The temperature of the system is characterized by the denominator on the exponential factor, identified as the  $p_1$  parameter in this fit. On the right side of Fig. 5.3.3, we observe the increase of the  $\langle p_T \rangle$  with increasing energy and particle mass, indicating the influence of radial flow.

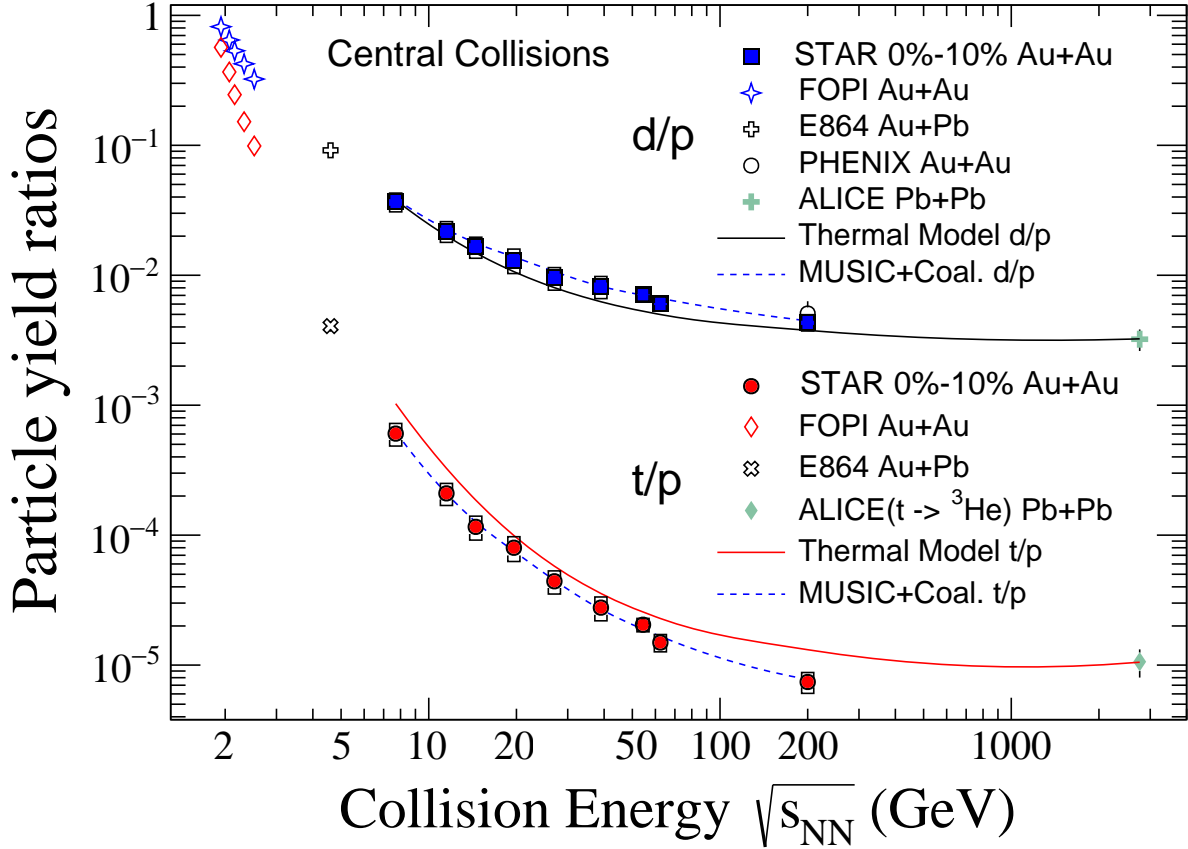


Figure 5.4.1: Collision energy dependence of the mid-rapidity ratios  $N_d/N_p$  (blue solid square) and  $N_t/N_p$  (red solid circles) from the top 0-10% central Au+Au collisions. Statistical and systematic uncertainties are shown as vertical lines and brackets, respectively. For comparison, results from FOPI [10], E864 [11], PHENIX [12, 13], and ALICE [14] are also shown. The solid and dashed lines are results from thermal model [15, 16] and MUSIC+COAL. model [9] calculations, respectively.



## 5.4 Particle Ratios

One of our goals in experiments involving relativistic heavy-ion collisions is to understand the properties and evolution of hot and dense matter. In medium energy nuclear collisions, a point of contention was the ratio of deuterons to protons,  $R_{d/p}$ , which is proportional to the neutron density in the phase space of the fireball, and characterizes the entropy of the fireball. The correlation between nuclear cluster formation and entropy can easily be understood as entropy serves as a metric for the level of organization in the system. Higher entropy indicates that the nucleons are loosely interacting with each other, while lower entropy signifies that a significant number of nucleons are grouped together in the form of cold nuclei [77, 78, 39]. In relativistic heavy ion collisions, light nuclear abundance can be used to characterize the entropy of the system, and further understand the mechanism of light nuclear formation and the equation of state of matter.

Figure 5.4.1 shows the energy dependence of  $dN/dy$  ratios,  $N_d/N_p$  [79] and  $N_t/N_p$ , in the mid-rapidity of central heavy-ion collisions from different experiments, including the FOPI [10], E864 [11], PHENIX [12, 13], and ALICE [14] experiments. Both the  $N_t/N_p$  and  $N_d/N_p$  ratios decrease monotonically with increasing collision energy and the differences between the ratios get smaller at lower collision energies. The solid lines represent the results calculated from the thermal model which does not include excited nuclei [80], in which the parametrization of chemical freeze-out temperature and  $\mu_B$  from Ref. [15, 16] are used. Quantitatively, the thermal model describes the  $N_d/N_p$  ratios well, but it systematically overestimates the  $N_t/N_p$  ratios except for the results from central Pb+Pb collisions at  $\sqrt{s_{NN}}=2.76$  TeV [14]. In addition, the coalescence model, which predicts light nuclei production at mid-rapidity based on baryon density ( $\rho_B$ ) via the relationship  $N_A/N_p \propto \rho_B^{A-1}$ , can also describe energy dependence trends [9].

The thermal model has been successful in describing the measured yields of hadrons and light (anti-)nuclei in central Pb+Pb collisions at the Large Hadron Collider (LHC) [81, 82]. However, the survival of light nuclei in the hot medium created in heavy-ion collisions remains a puzzle. One possible explanation is that the hadronic re-scatterings play a crucial role during the hadronic expansion phase. Dynamical model calculations with hadronic re-scatterings implemented using both the saha [83] and rate equations [84] show that the deuteron, triton, and helium-3 yields remain unchanged during hadronic expansion. A similar conclusion is obtained in a transport model simulation of hadronic re-scattering processes realized by the dissociation and regeneration of deuterons via the reaction  $\pi NN \leftrightarrow \pi d$  [85]. Recently, a calculation using the kinetic approach [86]



showed that the effects of hadronic re-scatterings during the hadronic expansion stage could reduce the triton and helium-3 yields by approximately a factor of 1.8 from their initial values predicted by the thermal model.

As mentioned earlier, the yield ratio  $N_t \times N_p / N_d^2$  is predicted to be sensitive to the local baryon density fluctuations and can be used to probe the QCD phase structure. Figure 5.4.2 shows the charged-particle multiplicity  $dN_{ch}/d\eta$  ( $|\eta| < 0.5$ ) dependence of the yield ratio  $N_t \times N_p / N_d^2$  in Au+Au collisions at  $\sqrt{s_{NN}} = 7.7 - 200$  GeV. The data from each collision energy presented in the figure include four centrality bins: 0-10%, 10-20%, 20-40%, and 40-80%, in addition, a single 0-20% centrality bin is also presented for 54.4 GeV. It is observed that the yield ratio  $N_t \times N_p / N_d^2$  exhibits scaling, regardless of collision energy and centrality. The shaded bands in Fig. 5.4.2 are the corresponding results from the calculations of hadronic transport AMPT and MUSIC+UrQMD hybrid models [9]. MUSIC is a (3+1)D viscous hydrodynamics model [87, 88], which conserves both energy-momentum and baryon number and is used to describe the dynamical evolution of the QGP. To provide a reliable baseline, neither critical point nor first-order phase transition is included in the AMPT and MUSIC+UrQMD hybrid model calculations. These two models are employed to generate the nucleon phase space at kinetic freeze-out, when light nuclei are formed via nucleon coalescence. It is found that the overall trend of the experimental data is well described by the model calculations. The light blue dashed line is the result calculated from the thermal model at chemical freeze-out [15, 16] for central Au+Au collisions, which overestimates the experimental data by more than a factor of two at  $dN_{ch}/d\eta \sim 600$ . As discussed in Ref. [86], this overestimation could be due to the effects of hadronic re-scatterings during hadronic expansion, which reduce the triton and helium-3 yields by about a factor of 1.8 from their initial values predicted by thermal model. However, this cannot explain the agreement between the thermal model calculations and the  $N_{3\text{He}} \times N_p / N_d^2$  ratio from central Pb+Pb collisions at  $\sqrt{s_{NN}} = 2.76$  TeV where  $dN_{ch}/d\eta \sim 1100$  [14, 89]. Obviously, further investigations are needed to understand the discrepancy.

The black dot-dashed line is a fit to the data based on the coalescence model. As discussed in Ref. [9], assuming a thermal equilibrated and static spherical Gaussian nucleon source, one can obtain the fit function as:

$$\frac{N_t \times N_p}{N_d^2} = p_0 \times \left( \frac{R^2 + \frac{2}{3}r_d^2}{R^2 + \frac{1}{2}r_t^2} \right)^3, \quad (5.4.1)$$

where  $R = p_1 \times (dN_{ch}/d\eta)^{1/3}$  denotes the radius of the spherical nucleon emission source.

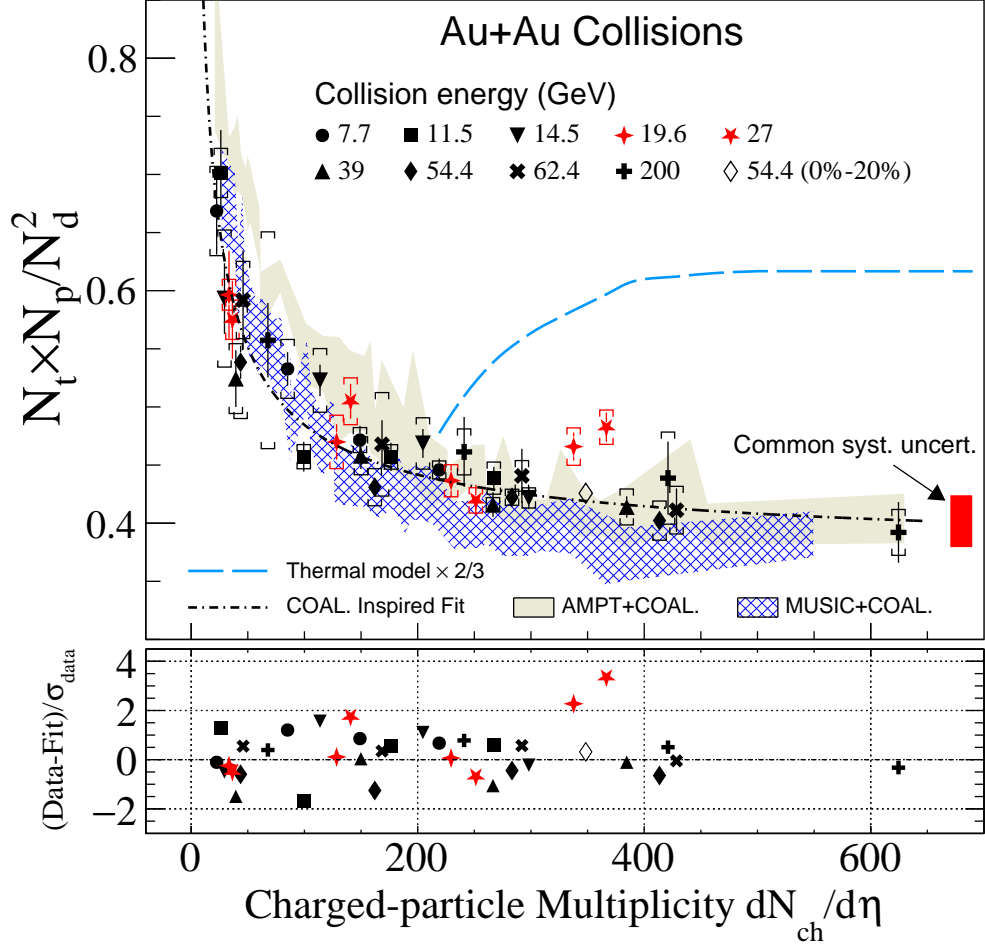


Figure 5.4.2: The yield ratio  $N_t \times N_p / N_d^2$  as a function of charged-particle multiplicity  $dN_{ch}/d\eta$  ( $|\eta| < 0.5$ ) in Au+Au collisions at  $\sqrt{s_{NN}} = 7.7 - 200$  GeV for 0-10%, 10-20%, 20-40%, and 40-80% centralities. Statistical and systematic uncertainties are shown as vertical lines and brackets, respectively. The black dot-dashed line denotes the coalescence-inspired fit. The open diamond denotes the yield ratio of 0-20% central Au+Au collisions at  $\sqrt{s_{NN}} = 54.4$  GeV. The red shaded vertical band on the right side of the figure represents the multiplicity independent systematic uncertainties on these ratios. The significance of the deviation relative to the fit is shown in the lower panel. The results calculated from thermal model are shown as the blue long-dashed line. Calculations from AMPT and MUSIC+UrQMD hybrid models [90, 9] are shown as shaded bands.

$r_d = 1.96$  fm and  $r_t = 1.59$  fm are the nucleonic point root-mean-square radius of deuteron and triton [91], respectively.  $p_0$  and  $p_1$  are the two fitting parameters where the best fit values are  $0.37 \pm 0.008$  and  $0.75 \pm 0.04$ , respectively. At small values of  $dN_{ch}/d\eta$ , when the system size is comparable to the size of light nuclei, the yield ratio shows a rapid increase with decreasing  $dN_{ch}/d\eta$ , while it saturates at large charged-particle multiplicity. The general trend of the yield ratio  $N_t \times N_p/N_d^2$  is driven by the interplay between the finite size of light nuclei and the overall size of the fireball created in heavy-ion collisions. This provides strong evidence that nucleon coalescence is the correct formation mechanism to describe the light nuclei production in such collisions. If we use the coalescence-inspired fit as the baseline, the lower panel of the Fig. 5.4.2 shows that most of the measurements are within significance of  $2\sigma$  from the coalescence baseline, except there are enhancements observed for the yield ratios in the 0-10% most central Au+Au collisions at  $\sqrt{s_{NN}} = 19.6$  and 27 GeV with significance of  $2.3\sigma$  and  $3.4\sigma$ , respectively, and for a combined significance of  $4.1\sigma$ , as shown in the lower panel of Fig. 5.4.2. The yield ratio of 0-20% central Au+Au collisions at 54.4 GeV is also shown in Fig. 5.4.2 as an open diamond. It agrees with the coalescence baseline at the same value of  $dN_{ch}/d\eta$  as those data points from central collisions at  $\sqrt{s_{NN}} = 19.6$  and 27 GeV. Therefore, the observed enhancement may be driven by the baryon density rather than the overall size of the system which is proportional to the charged-particle density  $dN_{ch}/d\eta$ . In order to understand the origin of the observed enhancement in the ratios, further dynamical modeling of heavy-ion collisions with a realistic equation of state is needed.

Figure 5.4.3 shows the energy dependence of the yield ratio  $N_t \times N_p/N_d^2$  at mid-rapidity in central (0-10%) and peripheral (40-80%) Au+Au collisions at  $\sqrt{s_{NN}} = 7.7 - 200$  GeV. For comparison, the coalescence baselines obtained by fitting the  $dN_{ch}/d\eta$  dependence of the yield ratio as shown in Fig. 5.4.2 and the calculations of AMPT, MUSIC+UrQMD hybrid models are displayed in Fig. 5.4.3. For the 0-10% most central Au+Au collisions, the yield ratios are consistent with the coalescence baseline and model calculations, except for the enhancements of the yield ratios to coalescence baseline with a significance of  $2.3\sigma$  and  $3.4\sigma$  observed at  $\sqrt{s_{NN}} = 19.6$  and 27 GeV, respectively. The colored bands in panel (a) denote the yield ratios, in which the proton, deuteron, and triton yields are obtained from the commonly measured  $p_T/A$  range without any extrapolation. The enhancements and the significance of the measurements decrease with smaller  $p_T$  acceptance in the region of interest. The combined (19.6 and 27 GeV) significance of enhancements to the corresponding coalescence baselines for  $0.5 \leq p_T/A \leq 1.0$  GeV/c,  $0.4 \leq p_T/A \leq 1.2$  GeV/c, and the full  $p_T/A$  range are  $1.6\sigma$ ,  $2.5\sigma$ , and  $4.1\sigma$ , respectively. In the model calculations, the physics

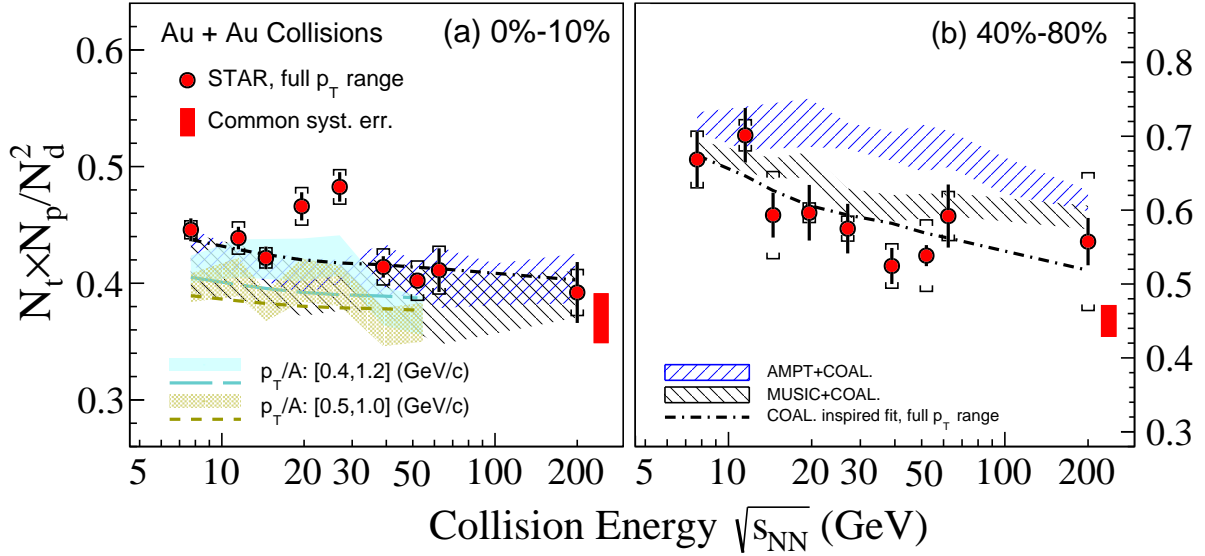


Figure 5.4.3: Collision energy, centrality, and  $p_T$  dependence of the yield ratio  $N_t \times N_p / N_d^2$  in Au+Au collisions at RHIC. Solid circles are the results from 0-10% central (left panel) and 40-80% peripheral (right panel) collisions. Colored-bands in panel (a) denote  $p_T$  acceptance dependence, for which the statistical and systematic uncertainties are added in quadrature. Red solid circles are the final results with extrapolation to the full  $p_T$  range. Statistical and systematic uncertainties are shown as bars and brackets, respectively. Red vertical bands on the right side of panels represent the common systematic uncertainties. Dashed lines are the coalescence baselines obtained from the coalescence-inspired fit. Shaded areas denote the calculations from hadronic transport AMPT and MUSIC+UrQMD hybrid models.

of the critical point or first-order phase transition are not included. Therefore, the non-monotonic behavior observed in the energy dependence of the yield ratio  $N_t \times N_p / N_d^2$  from 0-10% central Au+Au collisions may be due to the enhanced baryon density fluctuations induced by the critical point or first-order phase transition in heavy-ion collisions. The right panel of Fig. 5.4.3 shows the energy dependence of the yield ratio in peripheral (40-80%) Au+Au collisions. Within uncertainties, the experimental data can be well described by the coalescence baseline (black-dashed line) whereas the calculations from AMPT and MUSIC+UrQMD hybrid models overestimate the data.

Since the ALICE collaboration has published the proton and light nuclei yield of p+p 7.0 TeV [92, 93, 94], p+Pb 5.02 TeV [95, 96] and Pb+Pb 2.76 GeV [97, 14], we calculated the corresponding light nuclei yield ratio based on these published data. In the error processing, we have cancelled the correlated part of the systematic error of this ratio using the following formula. The definition of light nuclei yield ratio is

$$R = \frac{t \times p}{d^2} \quad (5.4.2)$$

According to the stand error propagation, the statistic error is

$$\Delta R = R \times \sqrt{\left(\frac{\Delta p}{p}\right)^2 + 4 \times \left(\frac{\Delta d}{d}\right)^2 + \left(\frac{\Delta t}{t}\right)^2} \quad (5.4.3)$$

The Systematic uncertainties without correlation is

$$\delta R = R \times \sqrt{\left(\frac{\delta p}{p}\right)_{uncorr}^2 + \left(2 \times \frac{\delta d}{d}\right)_{uncorr}^2 + \left(\frac{\delta t}{t}\right)_{uncorr}^2 + \left(\frac{\delta p}{p} + \frac{\delta t}{t} - 2 \times \frac{\delta d}{d}\right)_{corr}^2} \quad (5.4.4)$$

The calculation results of the Thermal-FIST model also added the light nuclei ratio at  $\mu_B = 0$  MeV for different temperature [98]. As we can see from the Fig. 5.4.4, it seems that ALICE measurements are closer to the thermal model, while STAR results can be better described using coalescence model.

The formation of light nuclei is correlated to the nucleon correlator, which can be directly measured. The critical point can be identified by the non-monotonous behavior of the fluctuation observable. By knowing the correlator for three-body, one can make quantitative predictions for fluctuation measures used in experiments. However, extracting the density fluctuation in heavy-ion collisions from experimental observables is challenging as only the particle momentum distribution is generally measured. Although the fireball created in heavy-ion collisions undergoes rapid expansion, density fluctuations resulting from spinodal instability or critical fluctuations

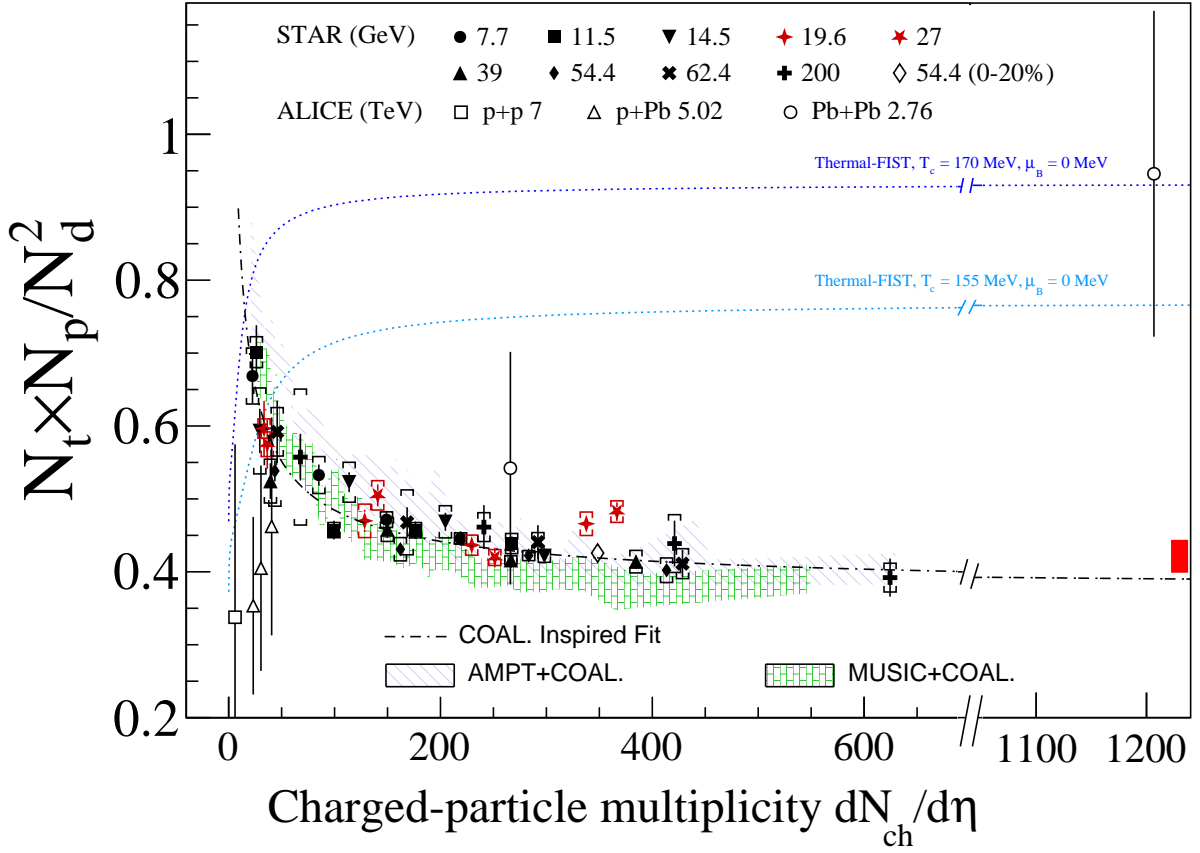


Figure 5.4.4: The yield ratio ( $N_t \times N_p / N_d^2$ ) as a function of charge particle multiplicity  $dN_{ch}/d\eta$  in Au + Au collisions at  $\sqrt{s_{NN}} = 7.7 - 200$  GeV from STAR by solid symbols. The open diamond denotes the yield ratio of 0-20% central Au+Au collisions at  $\sqrt{s_{NN}} = 54.4$  GeV. Statistical and systematic uncertainties are shown as vertical lines and brackets, respectively. The black dot-dashed line denotes the coalescence-inspired fit. The red shaded vertical band on the right side of the figure represents the multiplicity independence systematic uncertainties on these ratios from STAR measurements. From ALICE results: The open square is from p+p 7 TeV [92, 93, 94], the open triangle is from p+Pb 5.02 TeV [95, 96], and the open circle is from Pb+Pb 2.76 TeV [97, 14]. Statistical error and systematic error are combined shown as vertical lines. The results from a Thermal-FIST model with  $\mu_B = 0$  MeV at different temperature are shown as the blue dotted lines. Calculations from AMPT [90] and MUSIC+UrQMD hybrid [9] models are shown as shaded blue and green bands, respectively.

may persist despite final-state interactions. These fluctuations have the potential to influence observables that reflect nucleon density fluctuations and correlations at kinetic freeze-out, when particles cease interacting [28]. However, detecting large magnitude fluctuations alone does not confirm the existence of a critical point, as there are other factors contributing to fluctuations that are challenging to quantify. The event-by-event fluctuations of conserved quantities in relativistic heavy-ion collisions have extensively been studied both theoretically and experimentally. The energy dependence of the fourth-order fluctuation of net-proton distribution measured in the BES-I program by the STAR collaboration is found to exhibit the largest deviation from unity in Au + Au collisions at 19.6 GeV [99, 100, 101, 102]. Whether there is a correlation between the non-monotonous behavior of the fluctuation observable and the fourth-order fluctuation is still a question worth answering. With the upgrade of STAR detectors and the implementation of the BES-II program, the high statistical data and excellent detector performance will push the accurate measurement of these observables and even understanding of QCD phase diagram to a new level.

# Chapter 6

## Summary, Others, and Outlook

### 6.1 Summary

In summary, we present the measurement of triton production and the compound yield ratio  $N_t \times N_p/N_d^2$  in Au+Au collisions at  $\sqrt{s_{\text{NN}}} = 7.7 - 200$  GeV measured by the STAR experiment at RHIC. The yield ratio monotonically decreases with increasing charged-particle multiplicity ( $dN_{ch}/d\eta$ ) and exhibits a scaling behavior, which is explained by the formation of deuteron and triton via nucleon coalescence. On the other hand, the thermal model overestimates the triton over proton yield ratio  $N_t/N_p$  and the  $N_t \times N_p/N_d^2$  ratio at RHIC energies. This overestimation could indicate that the effects of hadronic re-scatterings during hadronic expansion play important role for light nuclei production in heavy-ion collisions. In the 0-10% most central Au+Au collisions at  $\sqrt{s_{\text{NN}}} = 19.6$  and 27 GeV, the yield ratio shows enhancements relative to the coalescence baseline with a significance of  $2.3\sigma$  and  $3.4\sigma$ , respectively, and a combined significance of  $4.1\sigma$ . The significance of the measurement decreases with reduced  $p_T$  range. This suggests that the possible enhancement may have a strong dependence on the  $p_T$  acceptance. In peripheral collisions, similar to data, model calculations have a smooth decreasing trend as a function of energy. Further detailed calculations from dynamical modeling of heavy-ion collisions with a realistic equation of state are required to determine whether the enhancements are due to large baryon density fluctuations induced by critical point. In the BES program, the STAR experiment has measured the energy dependence of observables that are sensitive to the CP and/or first-order phase transition, including pion HBT radii [103, 104], baryon directed flow [105, 106], net-proton fluctuations [107, 108]

and intermittency of charged hadrons [109]. Non-monotonic energy dependencies were observed in all of these observables, and the energy ranges where peak or dip structures appear are around  $\sqrt{s_{NN}} \approx 10\text{--}30$  GeV. Those intriguing observations are of great interest and more investigation and analysis are required to reach definitive conclusion. The systematic measurements of light nuclei yields and their ratios over a broad energy range provide important insights into the production dynamics of light nuclei and our understanding of the QCD phase diagram.

The exploration of the microstructure of matter is one of the fundamental questions in mankind's quest for understanding the mysteries of nature. This pursuit dates back to as early as the 4th century B.C., where people pondered the structure of matter in terms of particle theory and the "atom" idea. However, these were only hypotheses without sufficient and rigorous scientific basis. As human civilization progressed, science and technology gradually became an integral part of people's lives and began to dominate them. With the discovery of electricity, rays and the deepening understanding of nature, it inspired generations of explorers of scientific and technological civilization who continued to explore in the darkness, where unknown dangers could not stop them from seeking the truth. Today, modern physics and human civilization appear to be at the pinnacle of development but standing in the depths of the distant universe and looking back at the earth. We realize that the advancement of science and technology has brought tremendous changes and will continue to do so. The development of civilization doesn't seem to have an end, and therefore, it is essential to ponder more about the meaning of human civilization's existence.

## 6.2 Di-lepton Production

One of the main research goals behind high-energy experiments of relativistic heavy-ion collisions is the study of the properties of QCD substances. However, the use of final state hadrons as probes to examine the properties of QGP can be affected by strong interactions during the evolution of the system. Alternatively, electromagnetic probes such as di-electron are not impacted by strong interactions during system collisions and can offer a more precise and direct understanding of the collisions.

Di-electrons are produced through various mechanisms during collisions. The mass of the produced di-electrons determines their generation time in the collision. In the early stages of the collision, positive and negative quarks are mainly produced by Drell-Yan annihilation of the di-electron, which contributes primarily to the high-invariant mass region ( $M_{ee} > 3$  GeV/ $c^2$ ).



As the high-density and high-temperature medium generated by the collision heats up rapidly, leptons from heavier quarks through semi-leptonic decay accumulate mainly in the intermediate mass region ( $1 < M_{ee} < 3 \text{ GeV}/c^2$ ), following the thermodynamic statistical distribution. In the later stages of the collision, di-electrons are produced through meson annihilation and the decay of other hadrons, which contribute mainly to the low-mass region ( $M_{ee} < 1 \text{ GeV}/c^2$ ). Fig. 6.2.1 shows the invariant mass spectrum of di-electrons [110].

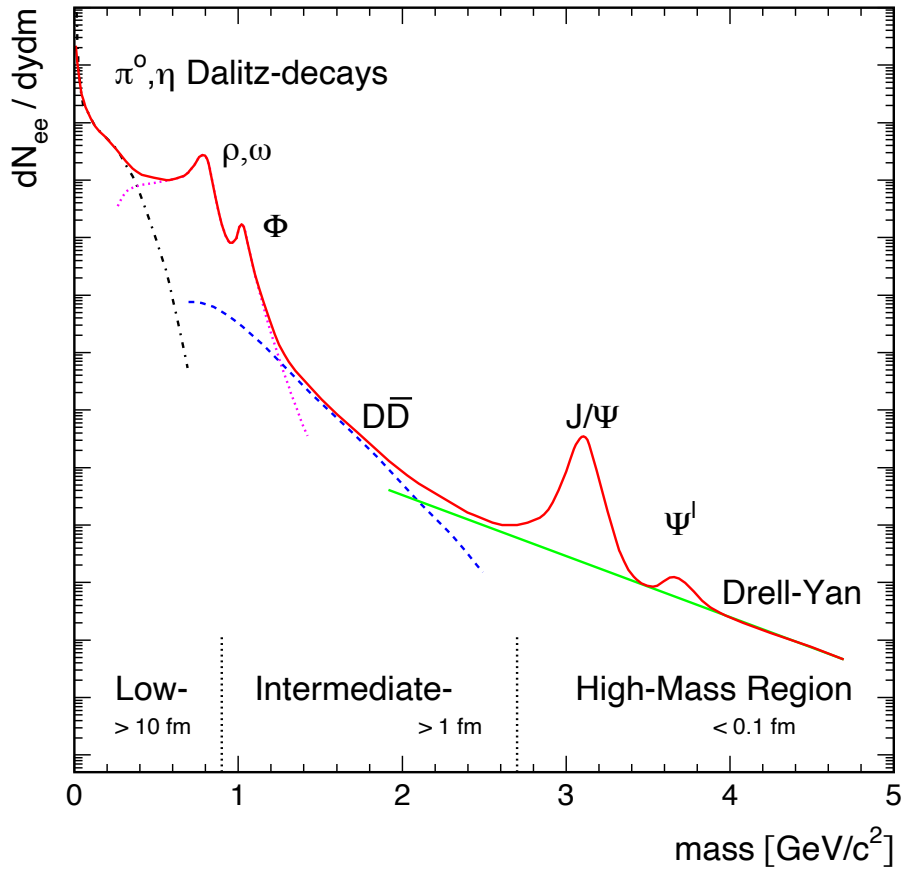


Figure 6.2.1: Expected source for di-lepton productions as a function of invariant mass in ultra-relativistic heavy-ion collisions.

The measurement of di-electrons presents a significant challenge in distinguishing between the

combinatorial background and the signal. To overcome this challenge, experiments have tried to include detailed invariant mass intervals. Recently, the GSI HADES experiments on p+p, p+A, and A+A have expanded the measured mass intervals to include lower mass ranges [111]. With the STAR Collaboration's Phase II energy collection of Au+Au collisions, which provides high statistics at 3 GeV, there is an excellent opportunity to analyze the di-electron invariant mass spectrum [112].

### 6.3 Outlook

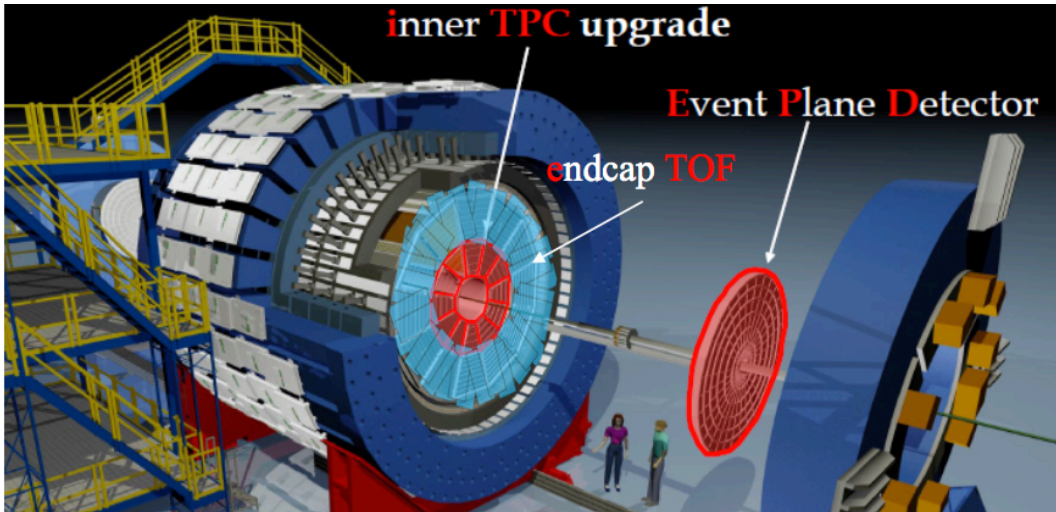


Figure 6.3.1: A view of the STAR detector with the BES-II upgrades highlighted. The EPD and iTPC are symmetric in STAR. The eTOF is only on the east side.

The STAR detector is an amazing masterpiece of advanced human technology, as a very successful exploration tool for studying strong interactions. The upgrade of the STAR detector has the central goal of maximizing the physical output of the Beam Energy Scan II (BES-II), which is achieved through detector upgrades (Fig. 6.3.1) and high precision data (Fig. 6.3.2). The upgraded detectors include, Event Plane Detector (EPD), inner TPC upgrade (iTPC), endcap TOF (eTOF), etc.. The iTPC will increase the acceptance of the TPC from  $|\eta| < 1$  to  $|\eta| < 1,5$ , improve the  $dE/dx$  resolution, and allow tracks to be reconstructed down to  $p_T \sim 60$  MeV/c. The



eTOF will extend STAR's PID capabilities at forward rapidities ( $-1.6 < \eta < -1.1$ ), complementing the existing Barrel TOF measurements in the region  $|\eta| < 0.9$ . The EPD will replace the BBC as a minimum-bias trigger detector and will provide forward measurements of the events plane and centrality.

The acquisition of data for the BES-II/FXT program has been successfully concluded, surpassing all the set targets for data acquisition. A bar chart in Fig. 6.3.2 illustrates the BES-II/FXT recorded data sets as compared to the older BES-I data sets, and the energies for which there is overlapping coverage from both the collider and fixed-target plans are also included. The bars are presented with respect to  $\mu_B$  show the range of  $\mu_B$  as well as the step size. The collision energies ( $\sqrt{s_{NN}}$ ) are annotated on the top edge of the plot to improve clarity. Overall, with its enhanced capabilities in gathering highly accurate data, the STAR detector is well-equipped to make significant strides towards understanding the mysteries of the Quark Gluon Plasma and unlocking the secrets of the universe.

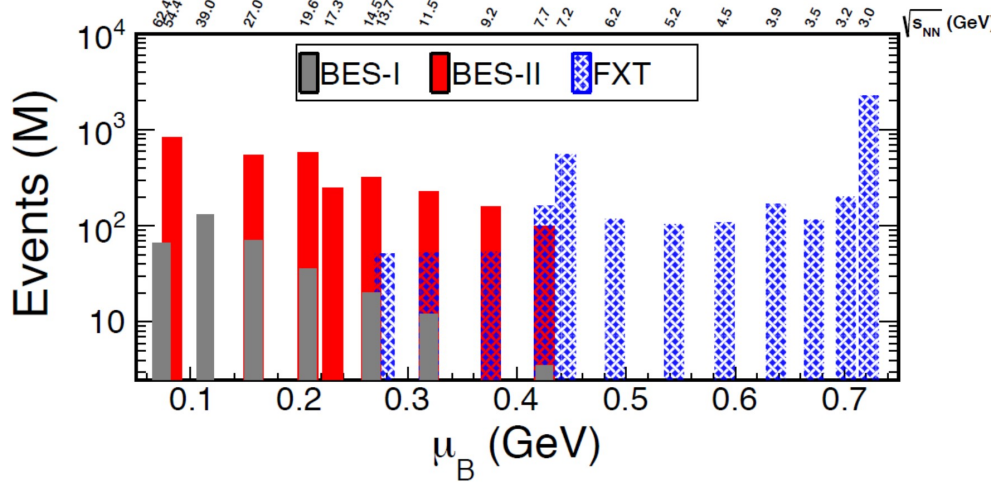


Figure 6.3.2: A summary of the good events acquired for the various collision energies (translated to  $\mu_B$ ). The BES-II collider data sets are shown in red bars. The FXT data sets are shown in hashed blue bars. For comparison the BES-I data sets are shown in grey bars.



## Bibliography

- [1] *Isospin*, chapter 2, pages 21–41. John Wiley and Sons, Ltd, 2017.
- [2] [https://commons.wikimedia.org/wiki/File:Standard\\_Model\\_of\\_Elementary\\_Particles.svg](https://commons.wikimedia.org/wiki/File:Standard_Model_of_Elementary_Particles.svg).
- [3] M. Tanabashi et al. Review of Particle Physics. *Phys. Rev. D*, 98(3):030001, 2018.
- [4] Xiaofeng Luo, Shusu Shi, Nu Xu, and Yifei Zhang. A Study of the Properties of the QCD Phase Diagram in High-Energy Nuclear Collisions. *Particles*, 3(2):278–307, 2020.
- [5] Peter Braun-Munzinger, Krzysztof Redlich, and Johanna Stachel. Particle production in heavy ion collisions. pages 491–599, 4 2003.
- [6] Feng Li and Che Ming Ko. Spinodal instabilities of baryon-rich quark-gluon plasma in the Polyakov–Nambu–Jona-Lasinio model. *Phys. Rev. C*, 93(3):035205, 2016.
- [7] Feng Li and Che Ming Ko. Spinodal instabilities of baryon-rich quark matter in heavy ion collisions. *Phys. Rev. C*, 95(5):055203, 2017.
- [8] Michael L. Miller, Klaus Reyers, Stephen J. Sanders, and Peter Steinberg. Glauber modeling in high energy nuclear collisions. *Ann. Rev. Nucl. Part. Sci.*, 57:205–243, 2007.
- [9] Wenbin Zhao, Kai-jia Sun, Che Ming Ko, and Xiaofeng Luo. Multiplicity scaling of light nuclei production in relativistic heavy-ion collisions. *Phys. Lett. B*, 820:136571, 2021.
- [10] W. Reisdorf et al. Systematics of pion emission in heavy ion collisions in the 1A- GeV regime. *Nucl. Phys. A*, 781:459–508, 2007.
- [11] T. A. Armstrong et al. Measurements of light nuclei production in 11.5-A-GeV/c Au + Pb heavy ion collisions. *Phys. Rev. C*, 61:064908, 2000.
- [12] S. S. Adler et al. Deuteron and antideuteron production in Au + Au collisions at  $\sqrt{s(\text{NN})} = 200\text{-GeV}$ . *Phys. Rev. Lett.*, 94:122302, 2005.
- [13] S. S. Adler et al. Identified charged particle spectra and yields in Au+Au collisions at  $\sqrt{s(\text{NN})} = 200\text{-GeV}$ . *Phys. Rev. C*, 69:034909, 2004.



- [14] Jaroslav Adam et al. Production of light nuclei and anti-nuclei in pp and Pb-Pb collisions at energies available at the CERN Large Hadron Collider. *Phys. Rev. C*, 93(2):024917, 2016.
- [15] V. Vovchenko, V. V. Begun, and M. I. Gorenstein. Hadron multiplicities and chemical freeze-out conditions in proton-proton and nucleus-nucleus collisions. *Phys. Rev. C*, 93(6):064906, 2016.
- [16] Volodymyr Vovchenko, Benjamin Dönigus, Behruz Kardan, Manuel Lorenz, and Horst Stoecker. Feeddown contributions from unstable nuclei in relativistic heavy-ion collisions. *Phys. Lett.*, B:135746, 2020.
- [17] Professor E. Rutherford F.R.S. Lxxix. the scattering of  $\alpha$  and  $\beta$  particles by matter and the structure of the atom. *The London, Edinburgh, and Dublin Philosophical Magazine and Journal of Science*, 21(125):669–688, 1911.
- [18] D. Iwanenko. The neutron hypothesis. *Nature*, 129:798–798, 1932.
- [19] Murray Gell-Mann. A Schematic Model of Baryons and Mesons. *Phys. Lett.*, 8:214–215, 1964.
- [20] O. W. Greenberg. Spin and Unitary Spin Independence in a Paraquark Model of Baryons and Mesons. *Phys. Rev. Lett.*, 13:598–602, 1964.
- [21] C. S. Wu, E. Ambler, R. W. Hayward, D. D. Hoppes, and R. P. Hudson. Experimental Test of Parity Conservation in  $\beta$  Decay. *Phys. Rev.*, 105:1413–1414, 1957.
- [22] Y. Aoki, G. Endrodi, Z. Fodor, S. D. Katz, and K. K. Szabo. The Order of the quantum chromodynamics transition predicted by the standard model of particle physics. *Nature*, 443:675–678, 2006.
- [23] A. Bazavov et al. Chiral crossover in QCD at zero and non-zero chemical potentials. *Phys. Lett. B*, 795:15–21, 2019.
- [24] Shinji Ejiri. Canonical partition function and finite density phase transition in lattice QCD. *Phys. Rev. D*, 78:074507, 2008.
- [25] Christian S. Fischer. QCD at finite temperature and chemical potential from Dyson–Schwinger equations. *Prog. Part. Nucl. Phys.*, 105:1–60, 2019.

- [26] Wei-jie Fu, Jan M. Pawłowski, and Fabian Rennecke. QCD phase structure at finite temperature and density. *Phys. Rev. D*, 101(5):054032, 2020.
- [27] Adam Miklos Halasz, A. D. Jackson, R. E. Shrock, Misha A. Stephanov, and J. J. M. Verbaarschot. On the phase diagram of QCD. *Phys. Rev. D*, 58:096007, 1998.
- [28] Mikhail A. Stephanov. QCD phase diagram and the critical point. *Prog. Theor. Phys. Suppl.*, 153:139–156, 2004.
- [29] Kenji Fukushima and Tetsuo Hatsuda. The phase diagram of dense QCD. *Rept. Prog. Phys.*, 74:014001, 2011.
- [30] J. D. Bjorken. Highly Relativistic Nucleus-Nucleus Collisions: The Central Rapidity Region. *Phys. Rev. D*, 27:140–151, 1983.
- [31] Gordon Baym. Kinetic theory and fluid dynamics in very high energy nucleus-nucleus collisions. In K. Kajantie, editor, *Quark Matter '84*, pages 39–52, Berlin, Heidelberg, 1985. Springer Berlin Heidelberg.
- [32] Hans Albrecht Bethe. Theory of atomic collisions. *Nature*, 167:165–165, 1951.
- [33] P. A. Piroué and A. J. S. Smith. Particle Production by 2.9-BeV Protons Incident on Beryllium and Platinum. *Phys. Rev.*, 148:1315–1326, 1966.
- [34] B. Schurmann. Effective nucleon numbers in relativistic heavy ion collisions. *Phys. Rev. C*, 20:1607–1611, 1979.
- [35] B. Schurmann and J. Randrup. QUASIELASTIC COMPONENT IN HIGH-ENERGY NUCLEAR COLLISIONS. *Phys. Rev. C*, 23:2766–2768, 1981.
- [36] H. W. Barz, L. P. Csernai, and W. Greiner. DIRECT NUCLEON EMISSION FROM HOT AND DENSE REGIONS DESCRIBED IN THE HYDRODYNAMICAL MODEL OF RELATIVISTIC HEAVY ION COLLISIONS. *Phys. Rev. C*, 26:740–743, 1982.
- [37] R. Bond, P. J. Johansen, S. E. Koonin, and S. Garpman. Breakup Densities of Nuclear Fireballs. *Phys. Lett. B*, 71:43–47, 1977.
- [38] H. Sato and K. Yazaki. On the coalescence model for high-energy nuclear reactions. *Phys. Lett. B*, 98:153–157, 1981.



- [39] L. P. Csernai and Joseph I. Kapusta. Entropy and Cluster Production in Nuclear Collisions. *Phys. Rept.*, 131:223–318, 1986.
- [40] S. Wheaton and J. Cleymans. THERMUS: A Thermal model package for ROOT. *Comput. Phys. Commun.*, 180:84–106, 2009.
- [41] T. Andrews. Bakerian lecture: On the continuity of the gaseous and liquid states of matter. *Proc. R. Soc. Lond.*, 18(114-122):42–45, 1869. Cited by: 10.
- [42] Kai-Jia Sun, Lie-Wen Chen, Che Ming Ko, and Zhangbu Xu. Probing QCD critical fluctuations from light nuclei production in relativistic heavy-ion collisions. *Phys. Lett. B*, 774:103–107, 2017.
- [43] Kai-Jia Sun, Lie-Wen Chen, Che Ming Ko, Jie Pu, and Zhangbu Xu. Light nuclei production as a probe of the QCD phase diagram. *Phys. Lett. B*, 781:499–504, 2018.
- [44] Kai-Jia Sun, Feng Li, and Che Ming Ko. Effects of QCD critical point on light nuclei production. *Phys. Lett. B*, 816:136258, 2021.
- [45] Peng Liu. The production of triton and reconstruction of  $^3\text{He}$  with the Heavy Flavor Tracker in Au+Au collisions at STAR. *Nucl. Phys. A*, 982:811–814, 2019.
- [46] Edward Shuryak and Juan M. Torres-Rincon. Baryon clustering at the critical line and near the hypothetical critical point in heavy-ion collisions. *Phys. Rev. C*, 100(2):024903, 2019.
- [47] Edward Shuryak and Juan M. Torres-Rincon. Baryon preclustering at the freeze-out of heavy-ion collisions and light-nuclei production. *Phys. Rev. C*, 101(3):034914, 2020.
- [48] Edward Shuryak and Juan M. Torres-Rincon. Light-nuclei production and search for the QCD critical point. *Eur. Phys. J. A*, 56(9):241, 2020.
- [49] Kai-Jia Sun, Wen-Hao Zhou, Lie-Wen Chen, Che Ming Ko, Feng Li, Rui Wang, and Jun Xu. Spinodal Enhancement of Light Nuclei Yield Ratio in Relativistic Heavy Ion Collisions. 5 2022.
- [50] <https://www.bnl.gov/newsroom/news.php?a=119262>.
- [51] <https://www.bnl.gov/rhic/complex.php>.



- [52] [https://www.bnl.gov/ec/files/EIC\\_CDR\\_Final.pdf](https://www.bnl.gov/ec/files/EIC_CDR_Final.pdf).
- [53] M. Anderson et al. The Star time projection chamber: A Unique tool for studying high multiplicity events at RHIC. *Nucl. Instrum. Meth. A*, 499:659–678, 2003.
- [54] W. J. Llope. The large-area time-of-flight upgrade for STAR. *Nucl. Instrum. Meth. B*, 241:306–310, 2005.
- [55] <https://drupal.star.bnl.gov/STAR/system/files/tof-5-24-2004.pdf>.
- [56] [https://www.star.bnl.gov/protected/bulkcorr/dingwei/minimc\\_index.html](https://www.star.bnl.gov/protected/bulkcorr/dingwei/minimc_index.html).
- [57] <https://indico.cern.ch/event/792436/contributions/3533912/>.
- [58] Clemens Adler, Alexei Denisov, Edmundo Garcia, Michael J. Murray, Herbert Strobele, and Sebastian N. White. The RHIC zero degree calorimeter. *Nucl. Instrum. Meth. A*, 470:488–499, 2001.
- [59] W. J. Llope et al. The TOFp / pVPD time-of-flight system for STAR. *Nucl. Instrum. Meth. A*, 522:252–273, 2004.
- [60] F. S. Bieser et al. The STAR trigger. *Nucl. Instrum. Meth. A*, 499:766–777, 2003.
- [61] C. A. Whitten. The beam-beam counter: A local polarimeter at STAR. *AIP Conf. Proc.*, 980(1):390–396, 2008.
- [62] H. Bichsel. A method to improve tracking and particle identification in TPCs and silicon detectors. *Nucl. Instrum. Meth. A*, 562:154–197, 2006.
- [63] <https://drupal.star.bnl.gov/STAR/starnotes/private/PSN0783>.
- [64] Giacomo Contin et al. The STAR MAPS-based PiXeL detector. *Nucl. Instrum. Meth. A*, 907:60–80, 2018.
- [65] D. Ashery and J. P. Schiffer. Pion Absorption in Nuclei. *Ann. Rev. Nucl. Part. Sci.*, 36:207–252, 1986.
- [66] B. I. Abelev et al. Systematic Measurements of Identified Particle Spectra in  $pp$ ,  $d^+$  Au and Au+Au Collisions from STAR. *Phys. Rev. C*, 79:034909, 2009.



- [67] Ekkard Schnedermann, Josef Sollfrank, and Ulrich W. Heinz. Thermal phenomenology of hadrons from 200-A/GeV S+S collisions. *Phys. Rev. C*, 48:2462–2475, 1993.
- [68] L. Adamczyk et al. Bulk Properties of the Medium Produced in Relativistic Heavy-Ion Collisions from the Beam Energy Scan Program. *Phys. Rev. C*, 96(4):044904, 2017.
- [69] Jaroslav Adam et al. Bulk properties of the system formed in Au + Au collisions at  $\sqrt{s_{NN}} = 14.5$  GeV at the BNL STAR detector. *Phys. Rev. C*, 101(2):024905, 2020.
- [70] B. I. Abelev et al. Energy dependence of pi<sup>±</sup>, p and anti-p transverse momentum spectra for Au+Au collisions at  $s(NN)^{1/2} = 62.4$  and 200-GeV. *Phys. Lett. B*, 655:104–113, 2007.
- [71] B. I. Abelev et al. Identified baryon and meson distributions at large transverse momenta from Au+Au collisions at  $s(NN)^{1/2} = 200$ -GeV. *Phys. Rev. Lett.*, 97:152301, 2006.
- [72] M. M. Aggarwal et al. Strange and Multi-strange Particle Production in Au+Au Collisions at  $\sqrt{s_{NN}} = 62.4$  GeV. *Phys. Rev. C*, 83:024901, 2011.
- [73] Jaroslav Adam et al. Strange hadron production in Au+Au collisions at  $\sqrt{s_{NN}} = 7.7, 11.5, 19.6, 27, \text{ and } 39$  GeV. *Phys. Rev. C*, 102(3):034909, 2020.
- [74] John Adams et al. Particle type dependence of azimuthal anisotropy and nuclear modification of particle production in Au + Au collisions at  $s(NN)^{1/2} = 200$ -GeV. *Phys. Rev. Lett.*, 92:052302, 2004.
- [75] L. Adamczyk et al. Beam Energy Dependence of Jet-Quenching Effects in Au+Au Collisions at  $\sqrt{s_{NN}} = 7.7, 11.5, 14.5, 19.6, 27, 39, \text{ and } 62.4$  GeV. *Phys. Rev. Lett.*, 121(3):032301, 2018.
- [76] Muhammad Abdulhamid et al. Beam Energy Dependence of Triton Production and Yield Ratio ( $N_t \times N_p / N_d^2$ ) in Au+Au Collisions at RHIC. *Phys. Rev. Lett.*, 130:202301, 2023.
- [77] P. J. Siemens and Joseph I. Kapusta. EVIDENCE FOR A SOFT NUCLEAR MATTER EQUATION OF STATE. *Phys. Rev. Lett.*, 43:1486–1489, 1979.
- [78] Joseph I. Kapusta. DEUTERON AND ENTROPY PRODUCTION AND THE NUCLEAR LIQUID - GAS PHASE TRANSITION. *Phys. Rev. C*, 29:1735–1743, 1984.
- [79] Jaroslav Adam et al. Beam energy dependence of (anti-)deuteron production in Au + Au collisions at the BNL Relativistic Heavy Ion Collider. *Phys. Rev. C*, 99(6):064905, 2019.



- [80] Volodymyr Vovchenko and Horst Stoecker. Thermal-FIST: A package for heavy-ion collisions and hadronic equation of state. *Comput. Phys. Commun.*, 244:295–310, 2019.
- [81] Anton Andronic, Peter Braun-Munzinger, Krzysztof Redlich, and Johanna Stachel. Decoding the phase structure of QCD via particle production at high energy. *Nature*, 561(7723):321–330, 2018.
- [82] Peter Braun-Munzinger and Benjamin Dönigus. Loosely-bound objects produced in nuclear collisions at the LHC. *Nucl. Phys. A*, 987:144–201, 2019.
- [83] Volodymyr Vovchenko, Kai Gallmeister, Jürgen Schaffner-Bielich, and Carsten Greiner. Nucleosynthesis in heavy-ion collisions at the LHC via the Saha equation. *Phys. Lett. B*, 800:135131, 2020.
- [84] Tim Neidig, Kai Gallmeister, Carsten Greiner, Marcus Bleicher, and Volodymyr Vovchenko. Towards solving the puzzle of high temperature light (anti)-nuclei production in ultra-relativistic heavy ion collisions. *Phys. Lett. B*, 827:136891, 2022.
- [85] Dmytro Oliinychenko, Long-Gang Pang, Hannah Elfner, and Volker Koch. Microscopic study of deuteron production in PbPb collisions at  $\sqrt{s} = 2.76\text{TeV}$  via hydrodynamics and a hadronic afterburner. *Phys. Rev. C*, 99(4):044907, 2019.
- [86] Kai-Jia Sun, Rui Wang, Che Ming Ko, Yu-Gang Ma, and Chun Shen. Unveiling the dynamics of nucleosynthesis in relativistic heavy-ion collisions. 7 2022.
- [87] Chun Shen and Björn Schenke. Dynamical initial state model for relativistic heavy-ion collisions. *Phys. Rev. C*, 97(2):024907, 2018.
- [88] Gabriel S. Denicol, Charles Gale, Sangyong Jeon, Akihiko Monnai, Björn Schenke, and Chun Shen. Net baryon diffusion in fluid dynamic simulations of relativistic heavy-ion collisions. *Phys. Rev. C*, 98(3):034916, 2018.
- [89] D. Oliinychenko. Overview of light nuclei production in relativistic heavy-ion collisions. *Nucl. Phys. A*, 1005:121754, 2021.
- [90] Kai-Jia Sun, Che Ming Ko, and Benjamin Dönigus. Suppression of light nuclei production in collisions of small systems at the Large Hadron Collider. *Phys. Lett. B*, 792:132–137, 2019.



- [91] G. Ropke. Light nuclei quasiparticle energy shift in hot and dense nuclear matter. *Phys. Rev. C*, 79:014002, 2009.
- [92] Jaroslav Adam et al. Measurement of pion, kaon and proton production in proton–proton collisions at  $\sqrt{s} = 7$  TeV. *Eur. Phys. J. C*, 75(5):226, 2015.
- [93] Shreyasi Acharya et al. Multiplicity dependence of (anti-)deuteron production in pp collisions at  $\sqrt{s} = 7$  TeV. *Phys. Lett. B*, 794:50–63, 2019.
- [94] Shreyasi Acharya et al. Production of deuterons, tritons,  $^3\text{He}$  nuclei and their antinuclei in pp collisions at  $\sqrt{s} = 0.9, 2.76$  and 7 TeV. *Phys. Rev. C*, 97(2):024615, 2018.
- [95] Shreyasi Acharya et al. Multiplicity dependence of light (anti-)nuclei production in p-Pb collisions at  $\sqrt{s_{\text{NN}}} = 5.02$  TeV. *Phys. Lett. B*, 800:135043, 2020.
- [96] Shreyasi Acharya et al. Production of (anti-) $^3\text{He}$  and (anti-) $^3\text{H}$  in p-Pb collisions at  $\sqrt{s_{\text{NN}}} = 5.02$  TeV. *Phys. Rev. C*, 101(4):044906, 2020.
- [97] Betty Abelev et al. Centrality dependence of  $\pi$ , K, p production in Pb-Pb collisions at  $\sqrt{s_{\text{NN}}} = 2.76$  TeV. *Phys. Rev. C*, 88:044910, 2013.
- [98] Volodymyr Vovchenko, Benjamin Dönigus, and Horst Stoecker. Multiplicity dependence of light nuclei production at LHC energies in the canonical statistical model. *Phys. Lett. B*, 785:171–174, 2018.
- [99] Xiaofeng Luo and Nu Xu. Search for the QCD Critical Point with Fluctuations of Conserved Quantities in Relativistic Heavy-Ion Collisions at RHIC : An Overview. *Nucl. Sci. Tech.*, 28(8):112, 2017.
- [100] L. Adamczyk et al. Energy Dependence of Moments of Net-proton Multiplicity Distributions at RHIC. *Phys. Rev. Lett.*, 112:032302, 2014.
- [101] M. M. Aggarwal et al. Higher Moments of Net-proton Multiplicity Distributions at RHIC. *Phys. Rev. Lett.*, 105:022302, 2010.
- [102] L. Adamczyk et al. Collision Energy Dependence of Moments of Net-Kaon Multiplicity Distributions at RHIC. *Phys. Lett. B*, 785:551–560, 2018.

- [103] L. Adamczyk et al. Beam-energy-dependent two-pion interferometry and the freeze-out eccentricity of pions measured in heavy ion collisions at the STAR detector. *Phys. Rev. C*, 92(1):014904, 2015.
- [104] J. Adam et al. Flow and interferometry results from Au+Au collisions at  $\sqrt{s_{NN}} = 4.5$  GeV. *Phys. Rev. C*, 103(3):034908, 2021.
- [105] L. Adamczyk et al. Beam-Energy Dependence of the Directed Flow of Protons, Antiprotons, and Pions in Au+Au Collisions. *Phys. Rev. Lett.*, 112(16):162301, 2014.
- [106] Leszek Adamczyk et al. Beam-Energy Dependence of Directed Flow of  $\Lambda$ ,  $\bar{\Lambda}$ ,  $K^\pm$ ,  $K_s^0$  and  $\phi$  in Au+Au Collisions. *Phys. Rev. Lett.*, 120(6):062301, 2018.
- [107] J. Adam et al. Nonmonotonic Energy Dependence of Net-Proton Number Fluctuations. *Phys. Rev. Lett.*, 126(9):092301, 2021.
- [108] Mohamed Abdallah et al. Cumulants and correlation functions of net-proton, proton, and antiproton multiplicity distributions in Au+Au collisions at energies available at the BNL Relativistic Heavy Ion Collider. *Phys. Rev. C*, 104(2):024902, 2021.
- [109] Energy Dependence of Intermittency for Charged Hadrons in Au+Au Collisions at RHIC. 1 2023.
- [110] R. Rapp and J. Wambach. Chiral symmetry restoration and dileptons in relativistic heavy ion collisions. *Adv. Nucl. Phys.*, 25:1, 2000.
- [111] Tetyana Galatyuk. Recent Results from HADES. *JPS Conf. Proc.*, 32:010079, 2020.
- [112] Zaochen Ye. Overview of STAR Results at Hard Probes 2020. *PoS*, HardProbes2020:005, 2021.

# Appendix

## A: 博士论文中文简介

相对论重离子碰撞实验中，最主要的目的是研究描述强相互作用量子色动力学 (QCD) 的相结构，而量子色动力学理论的基本成分是夸克和胶子。在自然界中，夸克和胶子被禁闭在强子内部，只有通过极端的实验环境 - 高温高密下才有可能得到自由的夸克胶子，这些解禁闭的夸克胶子物态与宇宙大爆炸后十几微秒产生的物质类似，通常被称之为夸克胶子等离子体 (QGP)。实验中人们将带电原子核加速至接近光速，然后使之发生碰撞，碰撞区域急剧升高的能量密度及温度将会产生我们想要研究的夸克胶子等离子体，因为整个过程发生的十分迅速，科学家只能通过观测其膨胀冷却后的末态粒子产物，通过分析这些末态粒子的性质来反推 QGP 的性质以及在碰撞过程中的整个演化过程。基于第一性原理出发的格点 QCD 计算得到，在重子化学势为零的区域，物质由 QGP 相到强子相的过渡是平滑穿越的。对于重子化学势更高的区域，格点 QCD 计算由于符号问题而失效，基于 QCD 有效模型计算的结果表明在较大重子化学势时则为一阶相变，一阶相变有个终点，被称之为 QCD 相变临界点。长期以来探索 QCD 相结构和寻找 QCD 临界点是重离子碰撞中的核心热点话题。经过多年理论和实验的不断发展，QCD 临界点寻找始终是一项具有挑战性的课题，实验方面，科学家通过重离子碰撞实验中的能量扫描来对相图进行探索和 QCD 临界点的寻找。

轻核作为重离子碰撞实验主要的末态产物之一，其形成机制也一直是一个悬而未解之谜，经过半个多世纪的发展，核子合并模型和热力学统计模型在描述其形成机制中取得了较为成功的结果，但是仍然有很多问题不能够解决。近年来有理论学家提出，基于轻核的核子合并模型，轻核的复合产额比值  $N_t \times N_p / N_d^2$  可以提取出系统演化中的中子数密度涨落，这为相边界和 QCD 临界点的寻找提供了新的思路和方法。当系统经过临界区域是，系统的关联长度发散，将会导致局域的重子数密度不均匀，而轻核是由多个核子组合而成的，重子数密度的涨落将会直接影响到轻核的产额，因为轻核形成的有效相互范围在核子大小范围内，这些系统演化的相关信息很有可能得以保



留。RHIC-STAR 自 2010-2017 年第一阶段能量扫描计划, 采集了金核-金核碰撞, 质心系能量为 7.7-200 GeV 的数据, 所对应的重子化学势从 750 -25 MeV, 这将覆盖了 QCD 相图中很大的区域, 这些数据为探索相图的结构提供了有效的途径。末态粒子的产额是我们实验测量中直接而有效的观测, 数据采集至今末态强子的产额都相继得以发表, 为了得到轻核复合产额比值, 我们对第一阶段能量扫描中的氩核产额进行了测量。我们知道在重离子碰撞末期, 有很多质子来自于奇异粒子的弱衰变, 需要将这一部分参与弱衰变的质子扣除, 才可以得到更加真实的轻核产额比值。2020 年 STAR 合作组发表了第一阶段能量扫描的奇异粒子产额, 这也为我们利用实验测量的奇异粒子来进行质子弱衰变的修正提供了很重要的信息。本文主要将会展示第一阶段能量扫描下, 金核-金核碰撞质心系能量  $\sqrt{s_{NN}} = 7.7, 11.5, 14.5, 19.6, 27, 39, 54.4, 62.4$  和 200 GeV 中氩核的测量细节, 以及相应能量下质子弱衰变修正的流程与结果。最终的也将讨论粒子产额比所提取到的物理信息以及相关模型计算。

论文由以下几个章节组成:

第 1 章介绍了本论文的研究背景、研究动机以及简单介绍本分析中用到的实验观测。

**研究背景、动机:** 本文首先介绍了现代物理学史的发展历程, 从基本粒子的探索到标准模型的建立, 经历了漫长的发展道路。1895 年德国物理学家伦琴首次发现 X-射线, 紧接着贝克勒尔发现了物质的放射性, 再由后来的居里夫妇在人工放射性方面的巨大贡献, 正式拉开了近代物理学探索微观世界的帷幕。1897 年汤姆逊证实了阴极射线为电子束流, 玻尔提出了最开始的氢原子模型, 人们对最小物质结构的认识是电子围绕原子核运转, 类似于行星围绕太阳的运动。早起的量子力学在计算氢原子能谱取得成功, 氦 4 的计算遇到了困难, 查德威克发现中子解决了这一难题, 也意味着人类的最基本粒子的认识上升到原子核的结构, 具体是电子围绕带正电的原子核运转, 原子核是由带正电的质子和不带电的中子组成。面对这个基本的认识, 摆在人们眼前的问题接踵而至, 束缚质子与中子形成原子核的又是什么? 毕竟带正电的质子紧挨在一起会有很强的库仑力相互排斥。随着爱因斯坦光电效应的发现, 人们认识到物质具有波粒二象性, 基于电子作为电磁相互作用的传递介质, Yukawa 提出质子与中子的束缚也是由一种很强的场使核子之间克服库伦排斥结合在一起, 在研究这个场的性质时过程中, 他计算得到在这个场中传递相互作用的媒介粒子质量为电子的 300 多倍, 质子质量的 1/6。后来科学家在宇宙射线中成功观测到这种粒子, 也被称之为介子。在此段期间, 量子力学已经迅速发展起来, 而相对论量子力学发展遇到了很大的困难, 在这些困难的解决过程当中, 狄拉克惊人的成就是以他的名字命名的狄拉克方程的发现。他在计算电子能量时得到了负能解, 也就意味着存在与电子质量一样, 带正电的粒子。这一度被认为是错误的, 后来正电子在宇宙射线中的发现, 揭开了反物质的崭新认识阶段。在这段时间里, 人们在研究贝塔弱衰变时, 发现电子能量在很宽的一个范围内以谱的形式连续呈现, 而这违背了能量守恒定律, 正当人们对能量守恒定律发起质疑时, 泡利大胆的提出了中微子的存在, 这将困扰大家的问题得以解决。



随着实验的证明，中微子得到了证实，并且也产生了轻子的概念，轻子数守恒也很快被提出。正当人们认为基本粒子的寻找已经完成时，科学家又从宇宙射线中发现了更多以前从未被发现的粒子，例如  $K^0 \rightarrow \pi^+ + \pi^-$ ,  $K^+ \rightarrow \pi^+ + \pi^+ + \pi^-$ ,  $\eta$ ,  $\phi$ ,  $\omega$  等介子， $\Lambda$ ,  $\Xi$ ,  $\Sigma$  等重子。在寻找基本粒子的整个过程中，人们由最开始的一两个粒子，到现阶段的上百种粒子，科学家也意识到这些粒子并非最基本的粒子，联想到门捷列夫的化学元素周期表，如何能将这些粒子进行分类成为了当时亟待解决的问题。

基本粒子的门捷列夫时莫里-盖尔曼，他在 1961 年的时候提出了重子八重态，具体的就是将最轻的八个重子放到了一个正六边形上，中间放两个，对角的粒子都具有相同的电荷数和奇异数，同样适用于最轻的介子。他利用这种分类方法精确的预言了  $\Omega$  粒子的存在，1964 年这个粒子被实验上发现，使得他提出的重子八重态或者十重态的分类不再被人们质疑。那么这么分类的原理又是什么呢？盖尔曼和乔治·茨威格几乎同时提出了所有强子是由更基本的粒子组成，后来盖尔曼称之为夸克。并且他们将夸克分为了三类，夸克带有分数电荷，且对应具有反夸克。夸克形成强子的基本规则为：重子由三个夸克组成；介子由夸克和反夸克组成。但是新的疑问是为什么不能观察到单独的夸克？并且有很多粒子是有相同的夸克组成，似乎与泡利不相容原理相违背。很长一段时间，人们不断的尝试寻找违背夸克模型的一些“反常”粒子，幸运的是始终没有发现这类粒子。1964 年色的概念引入，也就是夸克除了味的自由度，还具有色自由度，我们所看到的所有物种都具有色中性，这就聪明的解决了上面所遇到问题。1964 到 1974 年是粒子物理发展的贫瘠时期，夸克模型短暂的成功和热度也逐渐退去，1974 年夏天丁肇中领导的小组在布鲁克海文国家实验室发现了一种新的介子，当时为了确保他们的测量没有问题，这个秘密一被保守到同年的 11 月，位于 SLAC 的小组也独立的有着相同的发现，后来它们同时宣布了  $J/\psi$  的发现。紧接着关于  $J/\psi$  的性质进入了激烈的讨论，最终以夸克模型的解释获得了成功，这是由新的夸克  $c$  和  $\bar{c}$  组成。而早在几年前，因为发现的轻子已经有四种了，就有人提出夸克模型中存在第四种夸克，后来随着实验上发现存在单个  $c$  夸克的粒子，正式确认第四代夸克的存在。事情并没有就此结束，1975 年  $\tau$  轻子的发现，轻子数目上升为 6 个，两年后含有第五代夸克  $b$  的  $\Upsilon$  也被实验上发现，随着加速器的不断发展，最后一代夸克  $t$  在 1995 年在实验室发现。

从 Yukawa 提出介子作为强相互作用的媒介子，人们开始思考媒介子的相互交换传递了力。对于弱相互作用中的媒介子的寻找又是一个艰巨的挑战，因为我们没有办法去衡量弱力的力程，因为弱力顾名思义就是相互作用太弱，无法将粒子结合在一起。直到肖格拉、温伯格和萨拉姆的电弱相互理论的出现，这些所谓的中间矢量玻色子才被预言，CERN 专门建造了质子-反质子对撞机去验证它们的存在，实验上的最终确认也证实了电弱理论的正确性，同时人们也惊人的发现这些传递相互作用的粒子质量达到了质子质量的 100 倍。2013 年欧洲核子中心宣布希格斯粒子的发现，这个被预言半个多世纪的粒子，算是标准模型的最后一块拼图，他也将是整个模型的重要基石。至此



标准模型的建立算是取得了阶段性的胜利，这些发现无不证实着人类尖端科技的发展迅猛发展。

**量子色动力学 (QCD) 及临界点信号:** 从 1935 年 Yukawa 提出原子核内质子和中子是通过交换媒介子而形成原子核内很强的束缚力, 后来被证实这种媒介子是  $\pi$  介子, 这便开创了强相互作用的探究史。汤川的强相互作用与电磁相互作用相类比, 所不同的是交换的  $\pi$  介子是有质量的。在电磁相互作用中, 相互作用强度以电荷  $e$  标记, 强相互作用中用  $g$  标记。然而当人们将汤川理论和核力实验做对比, 发现有效相互作用强度远远大于 1,  $g^2/4\pi \approx 14$ , 这比电磁相互作用  $e^2/4\pi = 1/137$  大很多, 因此微扰理论已不再适用, 高阶项的贡献不仅不能忽略, 而且使整个微扰理论计算变得无意。随后发展的  $S$  矩阵理论和群论都在强相互作用的理解过程中起到了十分重要的作用。关于强相互所用的再次的重大突破是美国斯坦福直线加速器上电子轰击质子的深度非弹性散射实验, 标度无关性规律的发现。首先是 J. Bjorken 认识到标度无关性规律意味着大动量迁移下电子是与质子内许多无相互作用的自由点粒子发生相互作用, 也就是动量迁移很大时, 质子内的部分子具有渐近自由的现象。实验上不能击出自由的夸克, 只能通过间接的强子实验来观测它们的存在, 因此 QCD 的检验要比电磁相互作用中的理论检验困难的多。经过与电弱相互作用的类比, 人们发现强相互作用的有效耦合常数为变化的值, 当动量转移区域无穷大时, 强相互作用耦合常数区域 0, 但当动量转移很小时, 耦合常数则变为无穷大。经过后期的多年的实验验证, 渐近自由的性质也得以验证。因为当两个夸克之间的距离增大, 夸克之间交换胶子的能量就会变小, 跑动耦合常数就会变大, 以至于耦合强度变的无穷大, 这意味着夸克之间的相互作用随着分开距离的增加而增加, 使得夸克和胶子永远束缚在强子内部, 后来人们也形象的称之为“夸克禁闭”。

格点理论提出, 在温度极高, 重子化学势很低的时候, 由夸克胶子等离子体到强子相的过渡是平滑穿越的 QCD 的相关理论也研究提出, 当重子化学势增大, QGP 相到强子相则为一阶相变, 而一阶相变到平滑过渡区有个终点, 并称之为 QCD 临界点。在实验上, 人们也不断的尝试去形成夸克胶子等离子体来研究其性质, 位于美国纽约的布鲁克海文国家实验室以及欧洲核子研究中心专门建造了能够产生 QGP 的对撞实验。当介质的温度足够高或者密度足够大时, 禁闭在强子内的夸克胶子便会解禁闭形成自由的夸克胶子等离子体。RHIC-STAR 实验制定的能量扫描计划通过改变金核-金核对撞的质心能量, 来得到不同重子化学势下的介质性质, 是寻找 QCD 相边界以及临界点具有重要意义重离子碰撞实验。

**相对论重离子碰撞实验中轻核的产生:** 轻核是相对论重离子碰撞中主要的产物之一, 但是其形成机制在半个多世纪的发展当中始终是一个悬而未解的问题。核子合并机制模型和热力学统计模型在描述轻核产生当中都有着比较成功的地方, 但当更多精确实验数据的得到, 许多地方还是需要人们的进一步理解与修正。早期轻核形成机制的研究是在质子-原子核对撞实验中展开的, 氘核作为最简单的轻核, 也是人们最容易研究的对象。基于核子的相空间分布, 人们认识到氘核形成的概率是一个中子附近, 在有效的相互作用范围内, 出现一个质子的概率, 整个氘核的产额则为整个以



每个中子为中心的球形体积在全空间的积分，这便是最初核子合并模型的雏形。该简单模型的提出结合后期的实验观测，发展为轻核团簇的产额与所包含核子产额在相空间的关系，其相关系数的不断测量与修正，发展为现阶段相空间中轻核的波函数与核子在相空间中魏格纳函数的重叠所形成。随着热力学统计模型的发展，当末态的粒子间达到化学平衡，随着系统的膨胀粒子间的相互作用消失，自由的粒子都将在探测器中可以观测到。这个系统便可以由系统的热力学量来表征，温度、体积等都将决定解离后的最终状态。在热力学模型中，只要满足电荷重子数守恒，所有粒子都将根据统计力学配分函数中的玻尔兹曼因子来填充，即便所考虑的核子不在基态，只要守恒率成立便可。在此基础上更过研究小组提出了很多出发点，例如轻核形成时有效的冻结体积或相互作用体积，轻核结合能，核子共振态等。近年来，基于前面所讲的核子合并模型，有理论提出轻核的形成会受到系统局域重子数密度涨落的影响，系统局域重子数密度又于系统本身演化紧密相连，当系统中物质发生相变或达到临界点附近，系统的关联长度发散，从而引起系统重子数密度不均匀。而轻核在通过核子合并时，其相互作用长度可以这种局域密度的涨落得以体现。

第 2 章介绍了 STAR 实验的实验装置，以及我们的分析中所用到的探测器。

**相对论重离子对撞机：**RHIC-STAR 实验探测器坐落于美国纽约的布鲁克海文国家实验室，主题是由加速粒子的 RHIC 环和粒子发生对撞的交叉点处的探测器组成。RHIC 环总长有 2.8 公里，是目前世界上亮度较高，可以加速重离子和极化质子的加速器，环上总共有 4 个探测器，有三个现阶段都已关闭，目前只有 STAR 实验在运行。STAR 探测器是一个具有极大接受度，全方位角的探测装置，其设计的最初目的就是研究高能重离子碰撞末态的产物以及 QCD 相结构的研究，所以对末态粒子可以做到中心快度的全方位接受。STAR 探测器中最主要的径迹探测器是时间投影室，是一个圆柱形的场笼结构，圆柱形的直径为 4 米，高是 4.2 米，放置在一个螺线管磁铁当中，磁铁最大能产生 0.5 特斯拉强度的均匀磁场。束流管垂直穿过圆柱两端的圆面，整个场笼被一个圆形的高压膜沿着垂直于束流管的方向分为相等的两半，这个中心的高压膜最高可工作在 28 kV 下，圆柱的两端为低压面，直接接地，在众多电阻和等势环的调节下，场笼内会形成一个指向高压膜的均匀电场。TPC 的端盖装有基于多丝正比室技术的探测器，每个端盖被均匀的分为 12 等份，每一等份又分为外侧部分和内侧部分，外侧部分装有 3940 个小模块，分 32 行，内侧部分有 1750 个，分 13 行，详图参照 2.2.3。场笼内充有最高为两个大气压的 P10 气体，具体为 10% 的甲烷和 90% 的氩气，一般环境中，电子在工作气体中的漂移速度为  $5.45 \text{ cm}/\mu\text{m}$ 。当带电粒子穿过场笼时，工作气体被电离，产生的电子在电场的作用下飞向阳极丝并发生雪崩。信号的振幅被设计为飞行时间的函数，这样便可以得到该粒子在沿束流方向的坐标位置，而在端盖接受信号的这个模块又可以提供在垂直于束流管方向的坐标位置，这样便可以得到粒子穿过场笼的径迹。带电粒子穿过介质时都会损失能量，基于 TPC 的工作原理我们便可以同时记录带电粒子穿过工作气体时所损失的能量，这将作为粒子鉴别的重要测量量。根据带电粒子穿过物质所损失能量的性质，当入射粒子动



量偏高或低都会有不同的能损性质。TPC 探测器也是适用在某一给定的动量区间，当末态粒子的横动量继续增大，将会使得 TPC 探测器的分辨率降低。STAR 于 2010 年安装了飞行时间探测器，来将高横动量的粒子鉴别能力得以扩展，飞行时间探测器是基于多气隙电阻板室的技术，TOF 探测器安装在 TPC 圆柱形场笼的外部。每 34 个模块组合为一个托盘，场笼外侧东西两侧各有 60 个进行了  $2\pi$  方位角的覆盖。TOF 探测器主要测量粒子的飞行时间，而飞行时间的起始由位于束流管的顶点探测器提供，结合 TPC 所测量到的飞行距离和动量，粒子的质量便可以计算，这也就是 TOF 探测器的主要工作原理。

最后简单介绍了关于 STAR 探测器的仿真部分，因为探测器接受粒子都具有一定的效率，并且随着粒子数目的增大，接受效率也会随之降低，这就需要我们利用仿真技术来进行效率估计，在我们的分析中，质子弱衰变的修正也需要模拟奇异粒子通过探测器的衰变过程，所以进行简单的篇幅阐述。整套探测器的仿真都是由 GEANT 来完成的，在 STAR 中是以 *GSTAR/Starsim* 软件包的形式运行，其中包含了很多模块，包含了各个不同的子探测器，还有一些用户需要操作的接口，例如蒙特卡洛产生粒子的事件产生器，新粒子的性质以及衰变特性等都可以外部用户编辑及编译，最终作为库函数来调用。以奇异粒子的衰变为例，事件产生的径迹，包括径迹的全局动量，拟合所用到的点的数目等基本信息以一个标记的径迹来存储，这些事件的数据将会与实验采集到数据放到一起，然后通过仿真的探测器。*GSTAR/Starsim* 会将穿过探测器的这些模拟产生的径迹的信息存储起来，在计算效率以及粒子衰变信息都可以根据自身需要来读取。

第 3 章介绍了氙核测量的数据分析过程。

**数据集的筛选及中心度的定义：**所测量的氙核来自于 STAR 第一阶段能量扫描的金核-金核碰撞数据，质心系能量  $\sqrt{s_{NN}}$  为 7.7, 11.5, 14.5, 19.6, 27, 39, 54.4, 62.4, 和 200 GeV。其中 7.7, 11.5, 39 和 62.4 GeV 的数据采集于 2010 年，19.6, 27 和 200 GeV 采集于 2011 年，14.5 GeV 采集于 2014 年。54.4 GeV 采集于 2018 年且由同门同事完成，因最终能量依赖的物理结果需要该能量点，故将相关信息在此列出。所有的这些数据所处理的流程如下：首先是所有事件的挑选，根据探测器的位置，以及束流管的截面大小，通过重建的事件顶点进行第一次的事件挑选，第二步的事件挑选所采用的是对每一个事件中的重要观测量进行求平均，然后将偏差较大的事件进行事件日志查询，判定为不可用的事件，便将其从所有分析数据中剔除。利用挑选后的好事件，首先进行径迹质量的一些截断条件判选，因为事件中的所有径迹都是通过拟合粒子穿过 TPC 所留下的信号点所重建出来的，以及重建出来的径迹是否穿过碰撞顶点，径迹到碰撞顶点的最小距离等这些信息都会有所记录。这些截断条件的选择没有严格的标准，基本流程为填充这些参量随动量的分布，选出对径迹质量最好的截断条件，所以会带来一部分系统误差，在最终的分析中都会将其考虑。在这些事件挑选和径迹截断之后。下一步为事件碰撞中心度的划分，主要根据每个事件末态产生粒子的数目来作为划分标准。在核子-核子碰撞中，越是核子-核子对心碰撞，末态产生的粒子就越多，相对



于偏心的碰撞次之，边缘碰撞产生的粒子数目最少。末态带电粒子多重数将与碰撞的初始几何位置呈正比，因此可以将带电粒子多重数分布图按照百分比来划分，来指代不同的碰撞中心度。

**粒子鉴别：**氙核是有三个核子组成，其整体的平均横动量在 STAR 探测器中主要分布在相对较高的横动量区间。低横动量区间根据 DCA 判断，有很大一部分氙核来自于束流管或者探测器材料敲出，因为没有足够的反氙核来提供信号 DCA 的形状，所以背景扣除无法进行，为保证在低动量区间不引入过大的背景，我们的测量区间从横动量大于 1.2 GeV 开始，且在这个横动量区间内，TPC 探测器已经开始不能很好的鉴别氙核，我们采用 TPC 联合 TOF 进行了信号提取。氙核相对于质子算是产额比较低的粒子，即在金核-金核反应中截面较小，所以对数据的统计量有一定的要求。在分析当中，为了保证每个动量区间内有足够的统计量，可以通过拓宽测量区间或者中心度来实现。从 7.7-200 GeV 下，不同的能量，中心度和横动量下，信号有不同的分布特点，我们分析中具体分为了三类：1. 以 7.7 GeV 的中心碰撞中为实例，当测量区间内统计不是很大，且没有明显背景的区间，我们可以直接用高斯函数或者符合信号分布的函数去拟合，并且统计出该区间内总的统计点数，将拟合函数积分，可以直接对比看出该测量区间内信号个数与背景粒子的个数。这种方法只适用于能量较低（末态产生粒子较少），较低横动量区间内（氙核背景较少）。2. 这个提取方法应用于大多数粒子的原始信号提取，具体为该测量区间有足够的统计，并且有均匀的背景分布，需要通过函数去将整个测量区间的分布拟合好，然后将信号函数通过积分整个区间来得到，剩余的则都将是背景，氙核分析中用高斯函数和指数函数分别描述了信号和背景。尤其在高能量区域，背景分布为均匀变化时，利用数据分布中不同组分分别拟合来提取信号是唯一有效方法。3. 是直接在信号区间内进行统计求和，这种具体实例可以参考 7.7 GeV 边缘碰撞的分布，可以简单看出信号的数目，将偏离过大的视为背景剔除，这种情况只有信号特别干净或污染少，统计少时可用，视具体情况而定。200 GeV 因为背景粒子很多，所以测量的横动量区间由 1.5 GeV 开始，总体来讲氙核信号提取还是统计量不是很够，所以在很多测量区间只能通过调节数据分布直方图的横轴分割宽度来使信号拟合更加真实可信，这也将额外引入一部分系统误差，也在最终结果中加以了考虑。

第 4 章介绍了质子弱衰变的修正过程，及相关结果。

**动机及修正的数据：**在相对论重离子碰撞中，我们知道有一部分质子是来自于奇异粒子的弱衰变，具体的衰变通道以及分支比在粒子物理当中是比较基础的信息，可以在 PDG 书中找到。STAR 之前所发表的质子产额是没有经过奇异粒子弱衰变修正的，如果想利用质子产额来研究系统中强相互作用刚结束过程中的信息，这一步修正务必要完成，因为从基本信息可以看到对于  $\Lambda$  衰变到质子的分支比高达 64%，这也意味着在有些反应中，弱衰变会提供很大一部分末态直接测量到的质子，这将会直接影响到物理结论的讨论。STAR 探测器及很多探测器现阶段还不能直接在数据采集时将弱衰变的质子利用触发进行区分，因为奇异粒子寿命很短，探测器分辨率目前还不能达到。我们所修正的数据包括，STAR 第一阶段能量扫描中质心系能量为  $\sqrt{s_{NN}} = 7.7, 11.5, 14.5,$



19.6, 27, 39, 54.4, 和 62.4 GeV。需要注意这里 62.4 GeV 末态总质子数据采集于 2004 年, 且快度范围是  $|y| < 0.5$ , STAR 仿真数据来自于 2010 年的实验数据植入, 原则上只会引起系统误差内的变化。200 GeV 发表了实验数据为基础的弱衰变修正。关于奇异粒子的产额, STAR 实验中目前无法探测到电中性的粒子, 所以对于  $\Xi^0$ ,  $\Sigma^+$  产额将无法测量, 因为  $\Xi^0$  和  $\Xi^-$  质量寿命都很接近, 我们就用  $\Xi^0$  代替了  $\Xi^-$  产额。有热力学统计模型, 得到了  $\Sigma^+/\Lambda = 0.27$ , 我们假设该产额比值无动量中心度的依赖, 并将一个 20% 的相对误差添加到了  $\Sigma^+$  的产额中。

**质子弱衰变修正的流程:** STAR 合作组于 2020 年发表了奇异粒子的产额, 这将为质子弱衰变的修正提供了基本数据, 结合了 STAR 仿真的数据, 具体修正结果如下: 我们首先参数化了奇异粒子的横动量谱, 这样就保证了所有横动量区间都可以知道奇异粒子产额。然后用这个参数化的谱去将 MC 产生的奇异粒子谱在每一个横动量处加一个权重因子, 使它们的谱完全重合, 并对应记录好每个动量处的权重因子。然后将这些 MC 的奇异粒子经过 STAR 的仿真探测器, 得到衰变后的质子的横动量分布, 最后将对应动量处的权重因子去除, 在这个步骤中需要考虑每个奇异粒子的衰变通道及分支比。这样就得到了真实 STAR 实验中, 由奇异粒子衰变后的质子的横动量分布, 然后利用已经发表的总的横动量分布减去由奇异粒子衰变来的横动量依赖的质子分布, 就可以得到原初质子的产额。这问题的讨论中, 曾有人提到如果不利用 STAR 仿真数据, 只利用测量的奇异粒子产额, 乘以衰变分支比是否可以得到衰变的质子产额。这里需要考虑粒子测量事件的选取区间, 会影响到谱的归一化, 再就是奇异粒子的快度区间, 以及衰变后质子的快度区间, 测量总的质子的快度区间, 在对撞模式下的中心快度测量可能影响不会很大, 但是对于快度划分下的分析可能需要额外注意快度的对应问题。

**质子弱衰变修正的结果:** 我们对所有能量的测量质子弱衰变完成后, 估算了衰变质子占总质子的百分比。首先对于横动量依赖的占比, 其分布规律为从低动量到高动量呈递减分布, 因为衰变来的粒子大都会集中在低动量区间。对于每一个能量下质子衰变占比的分布具有较弱的中心度依赖, 这也就比较自然的结果。质子弱衰变的具有较强的能量, 随着质心系能量从 7.7 - 200 GeV, 百分比将会从 20% 上升至 45% 左右, 这将再次说明奇异粒子衰变的质子在能量较大的区间将是很大的占比。

第 6 章是整个分析中结果讨论的部分。

**粒子产额、核子聚合参数:** 首先最基础的便是我们的直接观测量, 氘核的横动量依赖的谱和修正后原初质子的谱。基于核子合并模型, 我们可以利用氘核和原初质子产额估算核子聚合参数  $B_3^t$ , 核子聚合参数与轻核形成的有效体积呈反比, 我们的测量展示了从低横动量到高横动量区间  $B_3^t$  递增, 也就意味着有效的核子聚合体积随着动量的增加而减小。对于固定能量下中心度依赖, 从中心到边缘碰撞  $B_3^t$  递增, 也就是核子有效的聚合体积在中心碰撞中最大。利用测量到的粒子横动量谱, 也就是微分产额, 对全空间积分后便可以得到粒子的积分产额, 因为测量的横动量区间有限,



我们只能在非测量区间采用函数外推的方式来估计外推区间的产额，最终产额将是这两部分的合并，因此积分产额的系统误差也将主要来源于非测量区间的理论不确定性。以每个动量区间内的产额占总产额的百分比为权重，再对整个动量空间进行积分，也可以的粒子的平均横动量，平均横动量将反应粒子在横向的运动速度的大小。

**粒子积分产额比值：**粒子产额比值一直是物理信息提取的很有效操作过程。氘核除以原初质子和氦核除以原初质子在 0-10% 中心度下的能量依赖在我们的分析中进行了估算，可以看到低能到高能两个比值都呈单调递减的行为，也就是说氘核、氦核产额随着碰撞能量的升高而降低，这在一定程度上反映了它们的产生机制及系统的熵变。重离子对撞中末态重子主要产方式有两种：对产生和重子阻止产生。我们知道在相对低的碰撞能量下，重子数密度高，较高的碰撞能量下重子数密度低，从图中我们可以看出低能轻核的产生更多的来源于重子阻止效应。

正如前面所提到的，轻核的复合产额比值  $N_t \times N_p / N_d^2$  在理论上预言是与系统局域中子数密度涨落直接关联，可以很好的作为探索 QCD 相结构的有效探针。经与 STAR 已经发表的数据相结合，我们计算的得到了该比值。结果中我们展示了带电粒子多重数依赖和能量依赖的轻核复合产额比值，下面将逐一讨论：带电粒子多重数依赖的分布，主要反映了该比值随着碰撞中心度，也就是碰撞系统大小的变化趋势。从 STAR 测量结果来看，随着碰撞碰撞中心度的增大，该比值呈单调递减的变化趋势，并且不同的能量的不同中心度下，只要系统带电粒子多重数一致，则该比值也相同，该比值不随能量的变化而变化，仅仅依赖于末态系统大小的标度行为。强子输运模型以及流体动力学模型，结合核子合并模型都能很好的描述我们测量的结果。而热力学统计模型在  $dN_{ch}/d\eta$  为 600 左右时，高估了这个比值约两倍以上，该模型的高估可能与一下两方面相关，其一强子共振态的衰变会直接影响到质子等的产额，强衰变的粒子会直接影响模型的计算结果。其二轻核在膨胀过程中受到强子的多重散射的影响，它会使得氘核或氦-3 的最终产额与热力学冻结后产额存在差异，这仍然需要更多的研究与计算。在我们的测量结果中，最为重要的是在质心系能量  $\sqrt{s_{NN}} = 19.6$  和 27 GeV，0-10% 的轻核复合产额比值出现了异常的增强，我们用基于核子合并模型的理论公式将  $dN_{ch}/d\eta$  依赖的比值进行了拟合，得到了很好的拟合结果。以拟合曲线作为该比值的基线，可以发现在 19.6 和 27 GeV 中心碰撞中的比值偏离基线的偏差达到了 4 被的标准偏差，而其它测量点都在 2 倍标准偏差以内，54.4 GeV 0-20% 中心度与 19.6, 27 GeV 中心碰撞的  $dN_{ch}/d\eta$  相接近，测量的比值基本落在了基准线上。这也就说明 19.6 和 27 GeV 中心碰撞中，轻核复合产额比值的增强是由系统的重子化学势不一样引起的，与系统末态体积无关。我们也将碰撞能量依赖的轻核复合产额比值得到，从测量结果发现，中心对撞中 19.6 和 27 GeV 的该比值出现了增强，而在边缘对撞和不包含临界点的模型计算中都没有出现这种异常的增强。如正如理论的预言，该比值是否反映了系统中子数密度的涨落，而系统重子数密度涨落，是否又是由于核物质相变而引起的，为了理解这个观测量及测量的实验结果，人们仍然需要更加真实的核物质状态方程来对系统演化进行



---

更多模拟与研究。

# Publications and Presentations

## Publications:

1. Energy Dependence of Light Nuclei ( $d$ ,  $t$ ) Production at STAR Dingwei Zhang (for the STAR Collaboration) [JPS Conf. Proc. 32, 010069 \(2020\)](#)
2. Beam Energy Dependence of (Anti-)Deuteron Production in Au+Au Collisions at the BNL Relativistic Heavy Ion Collider (STAR) [Phys. Rev. C 99, 064905 \(2019\)](#)
3. Search for QCD critical point by transverse velocity dependence of anti-deuteron to deuteron ratio  
Ning Yu, Dingwei Zhang, Xiaofeng Luo [Chinese Physics C Vol. 44, No. 1 \(2020\) 014002](#)
4. Light Nuclei ( $d$ ,  $t$ ) Production in Au+Au Collisions at  $\sqrt{s_{\text{NN}}} = 7.7 - 200$  GeV  
Dingwei Zhang (for the STAR Collaboration) [Nuclear Physics A 1005 \(2021\) 121825](#)
5. Light Nuclei Production in Au+Au Collisions at  $\sqrt{s_{\text{NN}}} = 5 - 200$  GeV from JAM Model  
Hui Liu, Dingwei Zhang, Shu He, Kai-jia Sun, Ning Yu, Xiaofeng Luo [Physics Letters B 805 \(2020\) 135452](#)
6. Beam Energy Dependence of Triton Production and Yield Ratio ( $N_t \times N_p / N_d^2$ ) in Au+Au Collisions at RHIC (STAR) [PHYSICAL REVIEW LETTERS 130, 202301 \(2023\)](#), [arXiv:2209.08058 \[nucl-ex\]](#)
7. 相对论重离子碰撞中 QCD 相图的实验研究 / Experimental study of the QCD phase diagram in relativistic heavy-ion collisions  
Yu Zhang, Dingwei Zhang, Xiaofeng Luo [NUCLEAR TECHNIQUES,2023,46\(04\):040001-040001](#)

## Presentations:

1. Beam Energy Dependence of Triton Production and Yield Ratio ( $N_t \times N_p / N_d^2$ ) in Au+Au Collisions at RHIC  
[CPOD 2022, November 28 - December 2, 2022](#)
2. Light Nuclei ( $d, t$ ) Production in Au+Au Collisions at  $\sqrt{s_{NN}} = 7.7 - 200$  GeV  
[Quark Matter 2019, November 4-9, 2019](#)
3. Collision Energy Dependence of Light Nuclei (Triton) Production at STAR  
[QPT 2019, August 16-20, 2019](#)
4. Energy Dependence of Triton Production and Neutron Density Fluctuations at RHIC  
[The 4th CBM-China Workshop, April 12-14, 2019](#)
5. Collision Energy and Centrality Dependence of Light Nuclei (triton) Production at STAR  
[NN2018, December 4-8, 2018](#)
6. Collision Energy and Centrality Dependence of Light Nuclei (Triton) Production at RHIC with the STAR Experiment  
[Quark Matter 2018, May 14-19, 2018 \(Poster\)](#)

# Achnowledgments

I would like to express my sincere gratitude to all those who supported me during my PhD studies. Your help was invaluable in enabling me to successfully complete my thesis. The contributions and efforts described in this thesis are a testament to the essential role that each of you played in this achievement.

First and foremost, I express my heartfelt gratitude to Prof. Xiaofeng Luo for his invaluable guidance and support in my academic and research journey from my master's degree to present. I am thankful to him for allowing me to be a part of the data analysis project for the STAR collaboration and providing me with numerous opportunities to enhance my knowledge and skills. I am proud to share that an article closely related to my thesis has been accepted Physical Review Letters in March 2023. Additionally, I extend my sincere thanks to Associate Prof. Ning Yu, presently associated with Hubei University of Education, for his meticulous mentoring and guidance in various crucial aspects of this work since the inception of my master's degree. I am also grateful to Dr. Nu Xu from LBNL, Dr. Zhangbu Xu from BNL, and Dr. Xin Dong from LBNL for their valuable assistance and direction in managing the critical details of this study. Lastly, I am indebted to Dr. Daniel Cebra from the University of California - Davis, Prof. Fuqiang Wang from Purdue University and Huzhou Normal University, and my many colleagues in the STAR collaboration for their invaluable inputs and suggestions.

I would like to express my gratitude to Prof. Feng Liu, Prof. Shusu Shi, Prof. Yaping Wang, Prof. Hua Pei, and Associate Prof. Zhiming Li from the STAR collabo-



ration at CCNU for the valuable time we spent together in discussing during our group meetings. I am also thankful to Shu He for his influence during my graduate studies, and I wish him a successful graduation with his excellent knowledge. A special thanks to all my colleagues from room 9427 Building 9 at CCNU, including Dr. Shaowei Lan, Dr. Yu Zhang, Jin Wu, Dr. Yingjie Zhou, Chuan Fu, Shuai Zhou, Yun Huang, Qianda Sheng, Yongcong Xu, Youquan Qi, Yige Huang, Yuantao Gu, Li-ke Liu, Zuowen Liu, Yanhuan Bai, Bijun Fang, Yixuan Jin, Hanwen Feng, Liubing Chen, Guoping Wang, Xin Wu, and Xin Zeng. I hope that everyone achieves great research results.

I would like to extend special thanks to Dr. Tetyana Galatyuk, Professor at the GSI Helmholtz Centre for Heavy Ion Research and Technical University of Darmstadt in Germany, for accepting me as a joint doctoral student and for her remarkable expertise and exceptional qualities in the field of dilepton physics. I apologize for not being able to complete the di-electron analysis work that you guided me on due to personal reasons. I also regret any inconvenience this may have caused. Additionally, I would like to thank Prof. Dr. Joachim Stroth, Dr. Jochen Markert, Dr. Szymon Harabasz, Niklas Schild, Wilhelm Krüger, Maximilian Wiest, Dr. Malgorzata Gumberidze, Dr. Maria Stefaniak, Dr. Adrian Rost, Dr. Frédéric Linz, Dr. Christian Wendisch, Vadym kedych, Nicolas Schwarz and someone I cannot recall the name, who provided me with a lot of help and enjoyable times during my study at GSI in Germany. Thanks also to my many Chinese friends such as Hui Liu, Ke Mi, Tiantian Chen, Tan Lu, Pengzhong Lu, Peng Ma, Dr. Bowen Zhou, Dr. Jiajun Yu, Yi Jin, and Kaiwen Jin, who were with me through both the joys and challenges of my time in Germany.

I am grateful to Dr. Lijuan Ruan from BNL for kindly accepting me as a joint PhD student after I received study abroad funding from the China Scholarship Council. Unfortunately, due to various obstacles such as COVID-19, we were unable to have further cooperation.

In December 2019, I began my doctoral research during the global outbreak of the COVID-19 pandemic. During this difficult time, countless heroes were defending our



beautiful homeland. Fast forward to December 2023, China's comprehensive epidemic prevention work marks the end of human struggle against the novel coronavirus. A famous scholar once compared scientific research to groping forward in a dangerous swamp, where countless brave warriors have paved the way to truth with one stone after another. Although many silent contributors have dedicated their lives to scientific exploration, some cannot leave their mark on the rugged road. The road of scientific exploration is an extremely difficult path for humanity, and my sincerest hope is that our world can provide better soil for scientific exploration, and the continuous progress and development of human technology will give every resident on this beautiful planet the opportunity to gaze upon the deep starry sky.

Lastly, I would like to express my sincere gratitude towards my family for their immense sacrifices and contributions during my doctoral studies. I am especially thankful to my wife, who gave birth to our beloved daughter in March 2021. I would also like to thank my father, who is bravely fighting against illness, and my mother, who tirelessly manages our household chores. Their unwavering support and encouragement have been crucial in my academic journey, and I am truly blessed to have them in my life.

“Three passions, simple but overwhelmingly strong, have governed my life: the longing for love, the search for knowledge, and unbearable pity for the suffering of mankind. These passions, like great winds, have blown me hither and thither, in a wayward course, over a great ocean of anguish, reaching to the very verge of despair.”

**What I Have Lived For ——— Bertrand Russell**